Universidade do Minho
Escola de Engenharia
Departamento de Engenharia Civil

POLITECNICO DI MILANO
Polo Regionale di Lecco

Assessing the possibilities of fibre reinforced concrete for underground prefabricated structures

Joaquim A. O. Barros & Marco di Prisco

Report 09-DEC/E-12

The present report resumes the research carried out within the ambit of the sabbatical licence of the 2008-09
The research was done at Polytechnic of Milan, under the supervision of Prof. Marco di Prisco

Date: October 2009
Nº of pages: 70

Key-words: Fibre reinforced concrete, box-culvert, finite element method, material nonlinear analysis

INDEX

AKNOWLEDGEMENTS

The first Author wish to acknowledge the support provided by FCT by means of the SFRH/BSAB/818/2008 and SFRH/BSAB/913/2009 sabbatical grants, as well as the excellent work conditions provided by Prof. Marco di Prisco. Thanks for the friendship environment of the colleagues of the Lecco Regional Polo of Politecnico di Milano.

Abstract. *The favourable effect that fibres provide at concrete crack initiation and propagation is especially notable in structures of high redundant supports, such is the case of concrete infrastructures surrounded by soil. If the design of these concrete structures is governed by crack width restrictions, fibre reinforced concrete is even a more competitive solution, since the stress redistribution provided by fibres bridging the micro-cracks allows the formation of diffuse crack patterns of reduced crack width. If these structures are precast with high strength concrete, and composed by thin walled components, fibres can effectively replace the total conventional transversal reinforcement, as well as a significant percentage of flexural reinforcement, resulting high competitive structures in economic and functional terms. However, to assess the fibre reinforcement benefits in this type of engineering problems, the concrete post-cracking behaviour and the soil-structure interaction behaviour need to be modelled as accurately as possible. The simulation of the phase construction is also a key aspect. In this work, the material nonlinear constitutive models implemented into FEMIX FEM-based computer program, as well as the computational tools for the simulation of the aforementioned phenomena are described. Using this computer program, the possibilities of discrete steel fibres as a shear and flexural reinforcement for box-culvert structures of distinct stiffness are explored. The results are presented and discussed.*

1 INTRODUCTION

The crack opening arrestment provided by the reinforcement mechanisms of fibres bridging the crack surfaces of cement based materials leads to significant increase in terms of load carrying capacity and energy dissipation capability of concrete structures, mainly those of high redundant support conditions, such is the case of structures surrounded by soil. In fact, as higher is the degree of static indeterminacy, as competitive can be the replacement of conventional steel bars by discrete steel fibres, since stress redistribution provided by fibre reinforcement allows an ultimate load much higher than the cracking load. In several underground reinforced concrete (RC) structures, crack width limit is the governing design condition, since a crack width higher than a certain value can compromise the durability and the functionality of theses structures, with economic and technical harmful consequences.
Box-culvert is one of these types of underground concrete structures, formed by a bottom and top U shape RC laminar elements connected by a concrete-concrete hinge connection (Fig. 1). Box-culverts are used for several purposes, like underground passages for persons, vehicles or animals (Fig. 1). These RC structures are subject to the soil dead weight, which in certain cases can attain a top cover layer 20m thick. Other constructions can also transfer loads to the box-culverts. On the soil surface, a live load (LL) can also actuate due to the action of vehicles or other non-permanent loads.

Fig. 1 – Examples of application of box-culvert.

Since the construction of this infra-structure is made by phases, the numerical simulation of this construction process is mandatory for a realistic prediction of the behaviour of the intervening materials and structures. Fig. 2 represents the current construction phase process used in this type of infra-structure. In general, the construction process is composed of 6 phases. In this figure [P_i-P_j] means a material or structural component pertaining to phases P_i up to P_j.
Fig. 3b and Fig. 4b represent the reinforcement detailing of the box-culverts analysed in the present work, whose geometries of the top part is shown in Fig. 3a and Fig. 4a, respectively. The first box-culver, with the tradename of m-50-5, is stiffer than the second box-culver, with the tradename of iv-200-8, in order to assess the potentialities of the fibre reinforcement for these two types of boxes. According to the information provided by a precast company, the reinforcement applied in m-50-5 (118.5 kg/m^3, see Fig. 3) was designed for an embankment soil layer thickness (H_{ST}) of 5 m (Fig. 2). In this box-culvert only flexural reinforcement was applied, since shear is not the governing failure mode. According to the same source, the reinforcement applied in iv-200-8 (214.8 kg/m^3, see Fig. 4) was designed for an embankment soil layer thickness of 8 m. In the m-50-5 box-culvert H_{sB}=3.64 m, H_{sT}=5.0 m

and the width of the trench is 9.1 m, while in the iv-200-8 box-culvert H_{sB}=9.08 m, H_{sT}=8.0 m and the width of the trench is 11.35 m.
In the present work the use of a self compacting concrete reinforced with 45 kg/m^3 of hooked ends steel fibres (SFRSCC), whose main characteristics are presented in Section 2, is explored with the purpose of verifying the possibility of replacing the reinforcement applied in the box-culverts of Fig. 3 and Fig. 4. Since iv-200-8 box-culver has both flexural and shear reinforcement arrangements, the capabilities of the fibres to replace totally the steel stirrups are also explored. To assess the shear reinforcement performance of steel fibres, in Section 3 of the present work is described an experimental program carried out with shallow beams shear reinforced with distinct fibre contents and with a sufficient high percentage of longitudinal reinforcement in order to force the occurrence of shear failure mode.

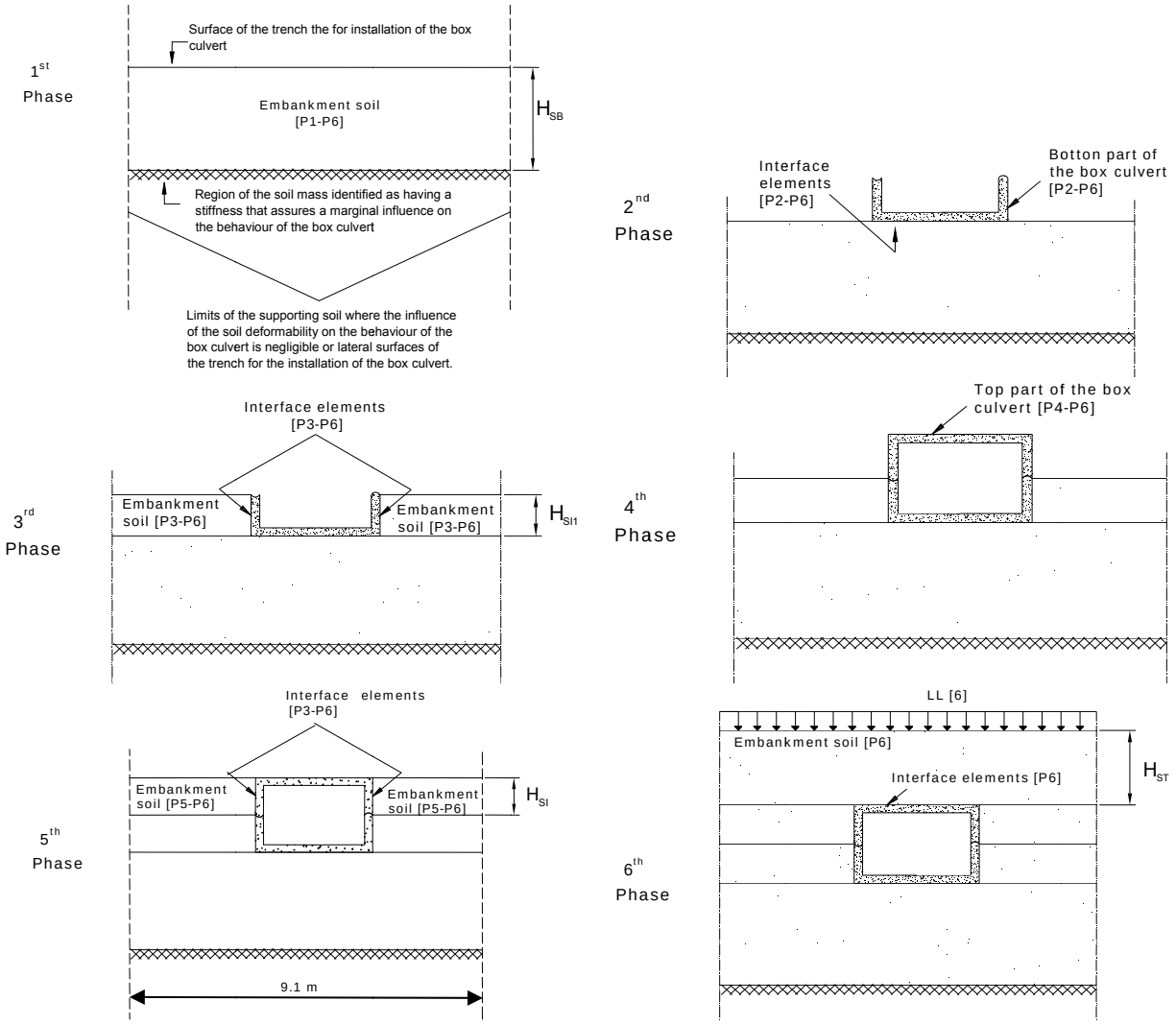

Figure 2 – Phase construction process.

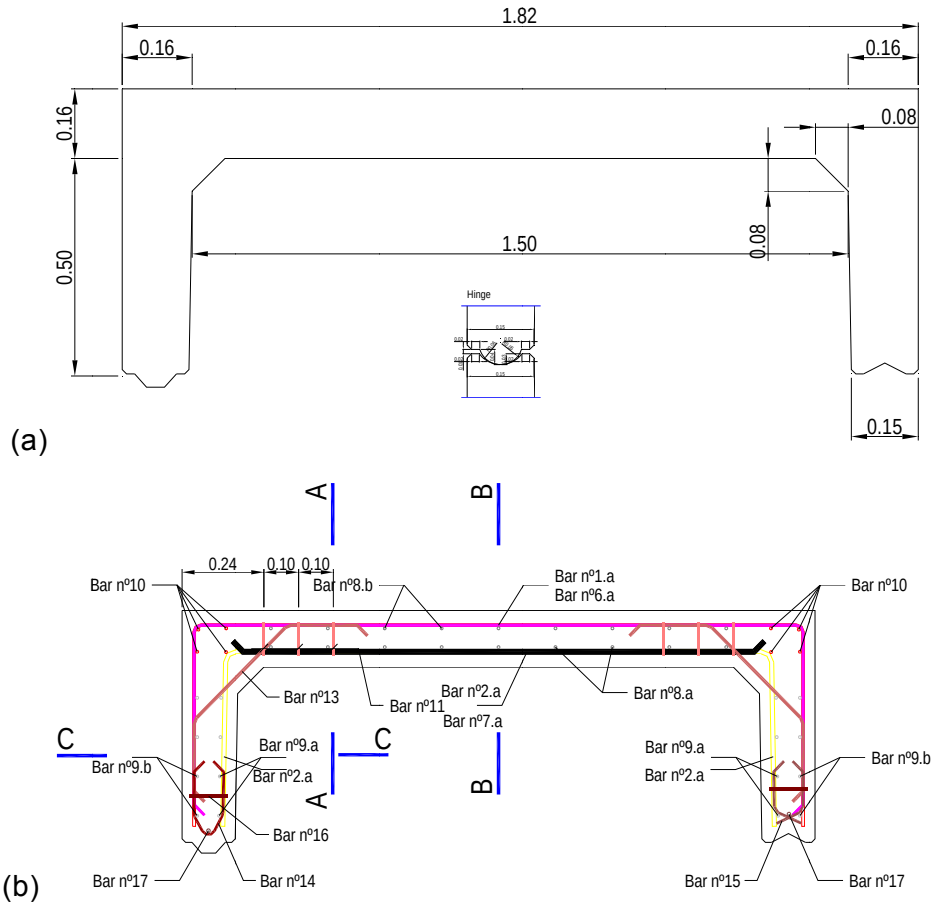

Fig. 3 – (a) Geometry and (b) reinforcement of the m-50-5 Box-culvert (dimensions in m).

Furthermore, the live load (LL of Fig. 2) that can be applied up to introduce a maximum crack width of 0.3 mm in the box-culvert will be evaluated, since below to this crack width the durability performance of SFRSCC is not affected by the action of the aggressiveness of environmental agents (Barros *et al.* 2008).

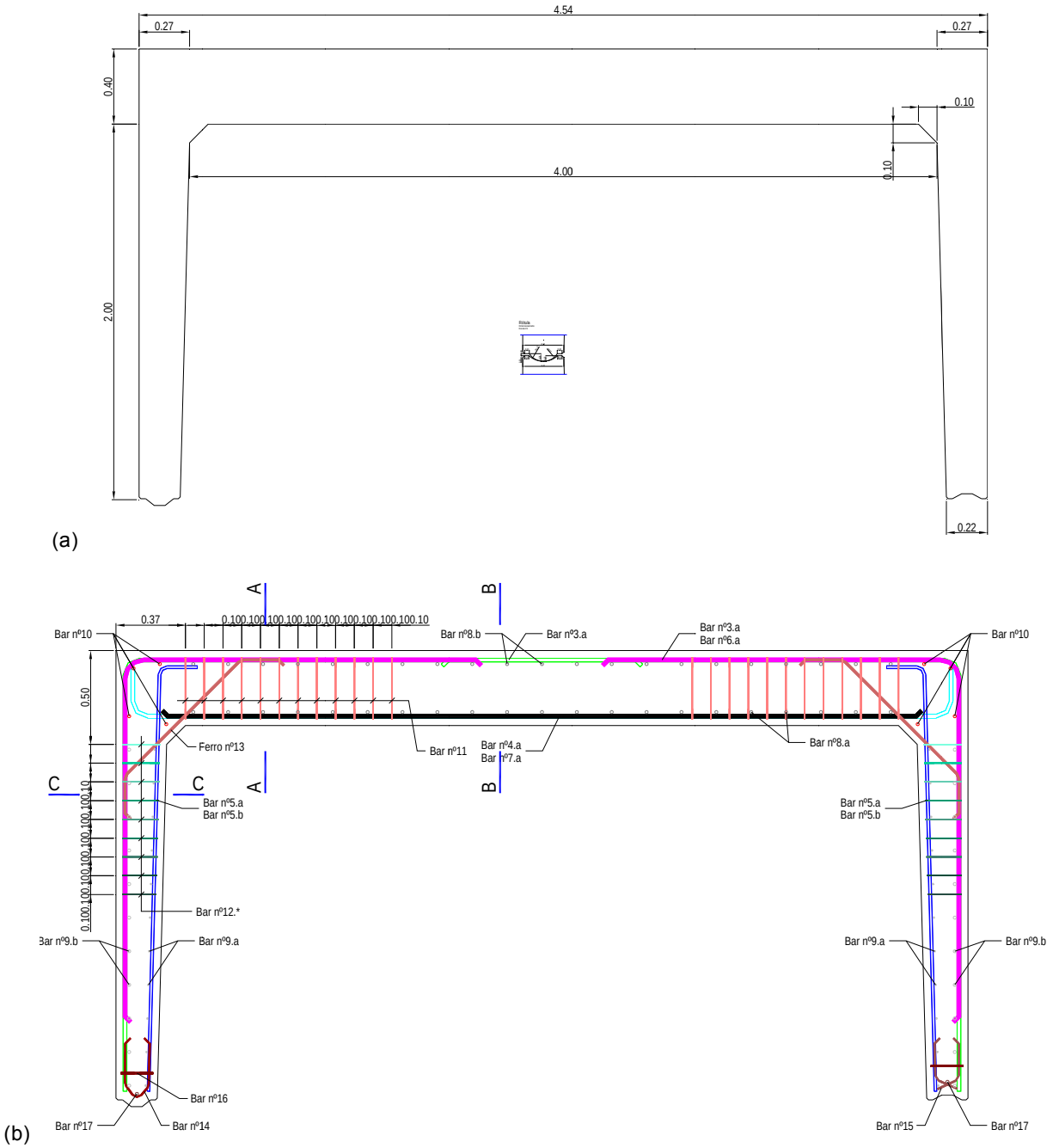

Fig. 4 – (a) Geometry and (b) reinforcement of the iv-200-8 Box-culvert (dimensions in m).

2 APPRAISING THE POTENTIALITIES OF SFRSCC FOR THE PARTIAL REPLACEMENT OF CONVENTIONAL REINFORCEMENT IN ELEMENTS FAILING IN BENDING

2.1 Introduction

Due to the reinforcement mechanisms provided by fibres bridging the crack surfaces, steel fibres have been used to enhance both the flexural and shear strength of concrete elements. In flexure, the presence of fibres decreases the crack width and the average crack spacing (Vandewalle 2000, Chiaia *et al.* 2009), and increase the load carrying capacity at serviceability and at ultimate limit states of structural members (Swamy and Al-Ta'an 1981).
The simulation of the contribution of steel fibres for the behaviour of laminar structures (slabs, shallow beams, shells and structures made by thin walled components like the case of box-culvert) of SFRC failing in bending is still a challenge, since several parameters influence this contribution, such as: geometrical characteristics and material properties of the fibres; concrete properties; method of SFRC application; geometry of the structure; loading conditions. Due to this fact, there are several approaches for modelling the contribution of fibre reinforcement, but none of them has received a full acceptance of the scientific community, which does not contribute for a more extended use of this high performance material, even in applications where its use would result in technical and economic advantages.
For the assessment of the potentialities of SFRC for structures with redundant number of supports, such is the case of underground concrete structures (surrounded by soil), an experimental program was carried out. In this type of structures, concrete crack width limit is a mandatory requisite in its design and, due to the congestion of conventional reinforcement in certain zones, its replacement for a certain content of steel fibres can be a favourable option in terms of assuring good concrete cast.
The advantages associated to the addition of steel fibres to concrete mixes may be joined with the ones resulting from the self-compacting ability concept in concrete (Okamura 1997), with the formulation of steel fibre reinforced concrete mixes exhibiting self-compacting ability (Steel Fibre Reinforced Self-Compacting Concrete, SFRSCC). Therefore, for the assessment of steel fibre reinforcement effectiveness for shallow structures failing in bending, SFRSCC was used.

2.2 Experimental program

2.2.1 Test series

The experimental program is composed of three series of shallow beams. Each one has a shear span (a = 450 mm) almost equal to 3.5 times the effective depth of the beam cross section (a/d $\approx$ 3.5), a total length of 1600 mm, a distance between supports of 1350 mm and a cross section area of 350×150 mm^2 (see Fig. 5). A distinct percentage of longitudinal reinforcement was adopted for each series of beams: 3ϕ6 (ρ_{sl} =0.2), 3ϕ8 (ρ_{sl} =0.36) and 3ϕ10 (ρ_{sl} =0.56), having been attributed the designations of A, B and C for these series, respectively. In all tested beams, three steel bars of 6 mm diameter were applied in the top part of the cross section. Twelve beams were tested: six reinforced with steel fibres and the other six without steel fibres, used for comparison purposes.

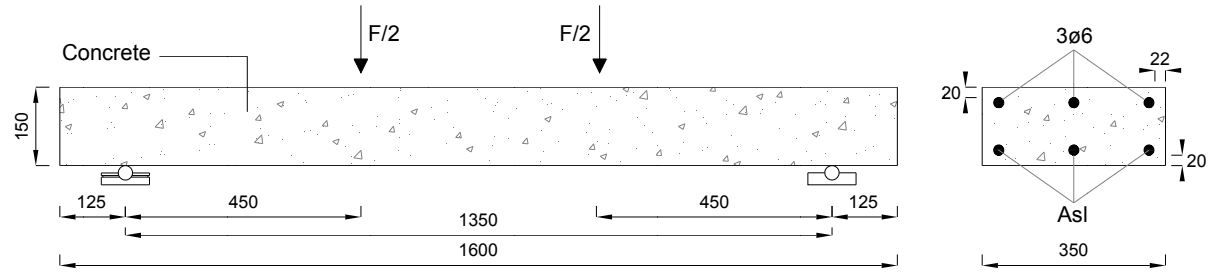

Fig. 5 - Geometry, support and load conditions of the tested shallow beams [mm].

2.2.2 Mix compositions

The mix composition adopted for the manufacture of the SFRSCC was optimized for a solid skeleton that includes 45 kg of the selected steel fibres per m^3 of concrete. This mix composition was obtained applying a design method that takes into account the strong perturbation effect produced by steel fibres on the flowability of fresh concrete. In fact, steel fibres are stiff and, consequently, do not easily accommodate to the dynamically changing shape of the bulk paste located between particles constituting the granular skeleton structure. Consequently, the design procedure and the optimization process followed to achieve self-compacting requirements are sensible to the fibre content, as well as to the geometrical and material properties of the fibres (Pereira 2006; Barros *et al.* 2007). The characteristics of the SFRSCC mix composition are included in Table 1. The materials used were cement (C) CEM I 52.5R (rapid hardening and high strength cement, according to EN197-1:2000), limestone filler MICRO 100 AB (LF), a superplasticizer (SP) with the trade name SIKA 3002 HE, water (W), four types of aggregates (fine river sand, FS; coarse river sand, CS; crushed calcareous 6-14 mm, CG_1; and crushed calcareous 14-20 mm, CG_2) and DRAMIX® RC-80/60-BN hooked ends steel fibres (SF). This fibre has a length (l_f) of 60 mm, a diameter (d_f) of 0.75 mm, an aspect ratio (l_f / d_f) of 80 and a yield stress of about 1100 MPa.

In the beams only reinforced with conventional steel bars, the self compacting concrete (SCC) mix was similar to the mix composition applied in the SFRC beams (see Table 1) apart the fact of the former one does not include fibres. This is not the most appropriate procedure, since the composition depends on the interferences introduced by the fibres. However, for the relatively small content of fibres used in this experimental program (45 kg/m^3), it was assumed that the changes necessary to introduce in the mix composition, due to the presence of fibres, are not so significant that compromise the principal conclusions of the present work. For both compositions no visual signal of segregation was detected and the mixtures showed good homogeneity and cohesion. The total spread, s, and the time to reach a spread diameter of 500 mm, T_f, measured with the slump cone in conjunction with J Ring, were measured, as well as the H_2/H_1 (blocking ratio) parameter of the L Box test (EFNARC 2002). The obtained results are indicated in Table 1, showing that the self-compacting requirements were assured.

Table 1 - Adopted composition (per m^3 of concrete).

Designation	C (kg)	W (kg)	SP (dm^3)	LF (kg)	FS (kg)	CS (kg)	CG_1 (kg)	CG_2 (kg)	SF (kg)	*s* (mm)	T_f (s)	H_2/H_1
SCC	380.5	102.7	12.5	360.0	391.4	429.1	336.9	298.2	0	700	12	0.80
SFRSCC	380.5	102.7	12.5	360.0	391.4	429.1	336.9	298.2	45.0	710	16	0.77

2.2.3 Test set up and monitoring system

The beams were subject to four line loads distributed in the width of the beam cross section (see Fig. 6). The force was registered by a load cell of 300 kN maximum capacity, while the deflections were measured from five LVDT's (Linear Voltage Differential Transducer), two of them of 25 mm measuring length (l_{meas}) placed at the middle of the shear span, and the others three of l_{meas} = 50 mm located at the central part of the beam. To avoid the recordings of extraneous deflections, like support settlements and deformability of the reaction frame, the LVDT's were supported on an aluminium bar fixed in the alignments of the supports of the beam, as represented in Fig. 6. The tests were carried out with servo-controlled equipment, imposing a deflection rate of 30 μm/s in the central LVDT for the test control purposes.

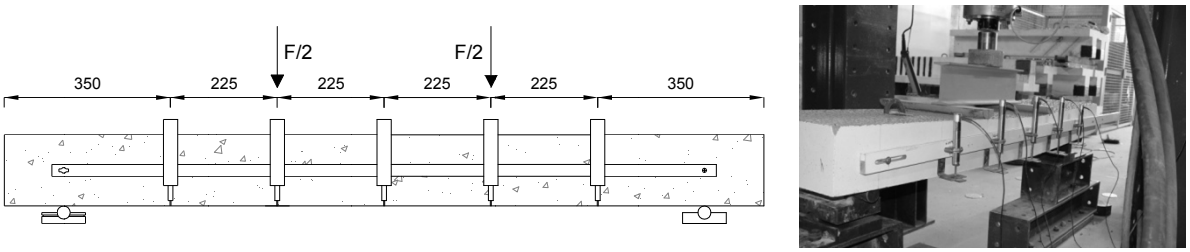

a) b)

Fig. 6 - Four point loading tests with shallow beams, including the monitoring system: a) schematic representation; b) real test execution.

2.2.4 Results and analysis

A label Li_j_k was used to differentiate the tested beams, where: "L" can be replaced by A, B or C to designate the series that the beam pertains; "i" identifies the number of the beam test in each series (two beams were tested per each series); "j" represents the diameter of the steel bars used as tensile longitudinal reinforcement; "k" represents the quantity of applied fibres (value in kg per m^3 of concrete). For instance, A2_6_45 beam represents the second beam of "A" series that is reinforced with 6 mm diameter longitudinal steel bars and includes 45 kg of steel fibres per m^3 of concrete. If "i" is omitted, the result represents the average value of the results of the beams of the corresponding series. The principal characteristics of each beam are indicated in Table 2.

Table 2 - Main characteristics of the tested shallow beams.

Designation	Longitudinal reinforcement (A_{sl}^{+})	Percentage of longitudinal reinforcement (ρ_{sl}) *	Fibre content FC (kg/m^3)	Series
A1_6_0 A2_6_0	3Ø 6	0.20	0	A
A1_6_45 A2_6_45	3Ø 6	0.20	45	
B1_8_0 B2_8_0	3Ø 8	0.36	0	B
B1_8_45 B2_8_45	3Ø 8	0.36	45	
C1_10_0 C2_10_0	3Ø 10	0.56	0	C
C1_10_45 C2_10_45	3Ø 10	0.56	45	

* $\rho_{sl} = \frac{A_{sl}^{+}}{b\,d} \times 100$

The relationship between the measured deflection in the midspan and the applied force of the tested beams is represented in Figs. 7, 8 and 9. Each curve corresponds to the average load values observed at each deflection level, obtained from the two beams of the corresponding series. From the analysis of these curves it is observed that, after crack initiation, the load carrying capacity of the SFRSCC beams is higher than the corresponding SCC ones. The difference of the load carrying capacity between these two types of beams increases from the crack initiation up to the maximum load of the SFRSCC beam. However, this difference decreases with the increase of the percentage of the conventional reinforcement.

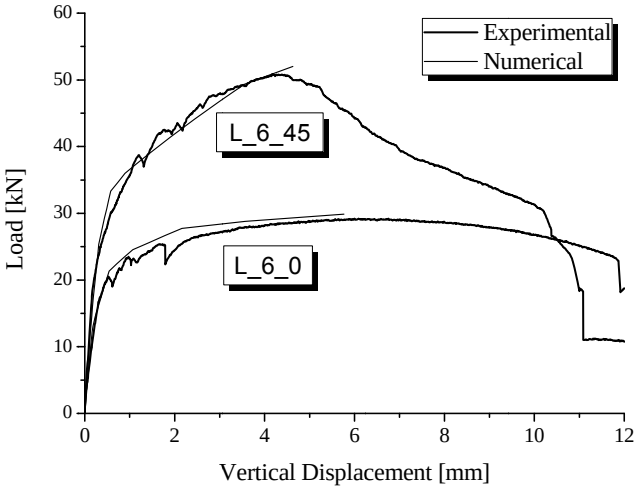

Fig. 7 - Load-central deflection curves of series L_6.

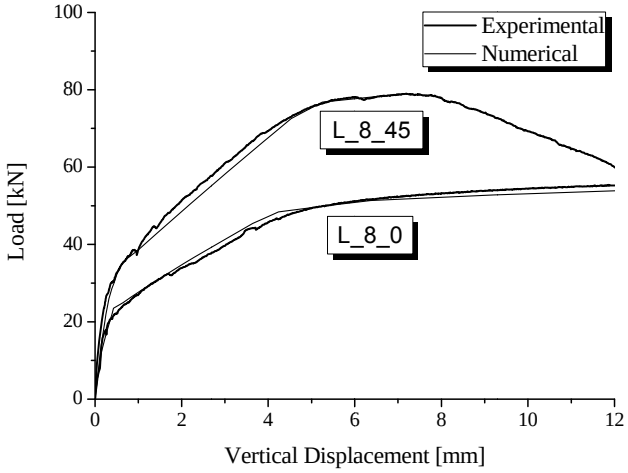

Fig. 8 - Load-central deflection curves of series L_8.

In terms of serviceability limit states (SLS) for deflection control, Eurocode 2 (2004) recommends that the maximum deflection of a structural member should not exceed a limit value in the range [L/250-L/500], depending on the type of structure, where L is the span length of the member, in mm. Assuming a limit value of u = L/400 = 3.4 mm (u_{SLS}) for the deflection, the corresponding force, F_{SLS}, was obtained (see Table 3, where F^{FRC} is the force of the beam

made by a fibrous composition and F^{ref} is the beam manufactured with the corresponding plain concrete).

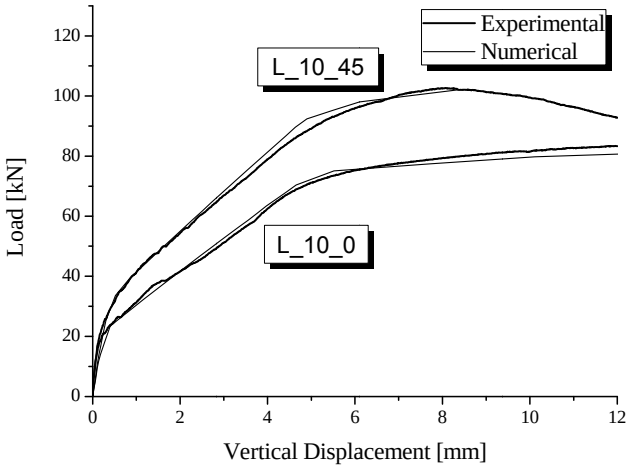

Fig. 9 - Load-central deflection curves of series L_10.

Table 1 - Force values of the tested beams.

Series	ρ_{sl}	F_{SLS} (kN)			F_{ULS} (kN)				
		F^{ref} [FC=0]	F^{FRC} [FC=45]	$\frac{F^{FRC}}{F^{ref}}$	F^{ref} [FC=0]	F^{FRC} [FC=45]	$\frac{F^{FRC}}{F^{ref}}$	$\frac{F^{ref}_{SLS}}{F^{ref}_{ULS}}$	$\frac{F^{FRC}_{SLS}}{F^{FRC}_{ULS}}$
A	0.20	27.68	49.03	1.77	29.19	50.76	1.74	0.95	0.97
B	0.36	42.46	64.45	1.52	55.42	78.96	1.42	0.77	0.82
C	0.56	55.53	71.60	1.29	83.53	102.59	1.23	0.66	0.70

FC: fibre content in kg/m^3

From the analysis of these values it can be verified that fibres increased F_{SLS} from 1.29 up to 1.77, when the F_{SLS} values of the SCC beams are taken for comparison purposes. This increase was as higher as lower was the reinforcement ratio of the longitudinal steel bars, ρ_{sl}. This table also includes the values of the maximum forces supported by the tested beams (F^{ref}_{ULS} and F^{FRC}_{ULS} is the maximum force of the SCC and SFRSCC beam, respectively). From the analysis of the F_{SLS} and F_{ULS} values it can be concluded that F_{SLS}/F_{ULS} ratio ranged from 0.66 to 0.95 in the beams without fibres, while in the beams reinforced with fibres the F_{SLS}/F_{ULS} ratio varied from 0.70 to 0.97. For both types of reinforcement F_{SLS}/F_{ULS} ratio increased with the decrease of ρ_{sl}. This shows that fibre reinforcement is very effective for the verifications of the design requirements imposed by the serviceability limit states, being this effectiveness as more pronounced as lower is ρ_{sl}.

To evaluate the increase in terms of beam's load carrying capacity provided by fibre reinforcement during the deflection process of the beams, the difference between the load carrying capacity of the SFRSCC and SCC beams, ΔF, for each deflection value, was evaluated. The relationship between the beam midspan deflection and ΔF/F ratio is represented in Fig. 10, in which F is the load carrying capacity of the SCC beam at the same deflection where ΔF is evaluated.

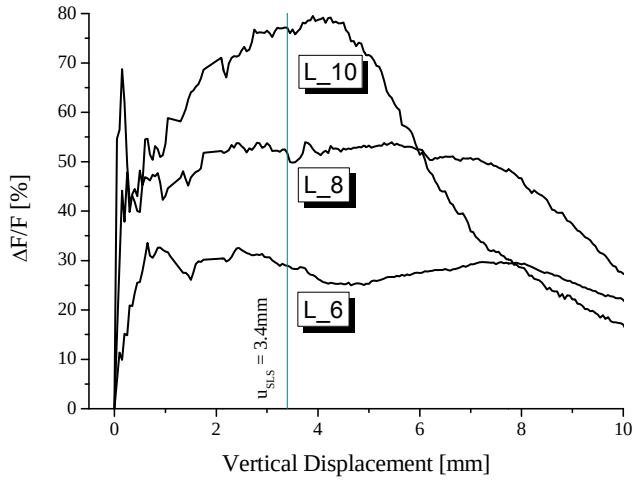

Fig. 10 - Relationship between the midspan deflection and the relative increment of the beam load carrying capacity for all series.

From the resulting curves it is apparent that the contribution of the fibres for the beam load carrying capacity starts from very early stages of the beam deformation, just after the formation of incipient cracks. It is visible that Δ*F/F* increases up to the deflection corresponding to the peak load of the SFRSCC beams, having this increase attained a maximum value of 80%. The decrease of Δ*F/F* ratio with the increase of ρ_{sl} is also apparent from Fig. 10. For the beams reinforced with the minimum percentage of longitudinal reinforcement (L_6) the maximum value of the Δ*F/F* ratio occurred at a deflection of about the deflection corresponding to the serviceability limit states (u_{SLS} = 3.4 mm). In the series of beams reinforced with the other two percentages of longitudinal reinforcement, the Δ*F/F* ratio maintained almost constant in the deflection range between 20% and 200% of the u_{SLS}. This means that the benefits provided by fibre reinforcement for the serviceability limit states are as more pronounced as lower is ρ_{sl}. In case of being necessary to increase Δ*F/F* of beams of considerable ρ_{sl}, a higher content of fibres needs to be applied. However, economic and technical aspects should be considered since, besides the higher costs of the fibres (in comparison to the one of conventional steel bars), the costs derived from the necessity of using higher percentage of fine materials in the concrete composition when the content of fibres increases should be also taken into account.
The indices $I_{F(SLS)}$ and $I_{F(ULS)}$, representing the relative increase of the beam load carrying capacity provided by fibre reinforcement for the deflection corresponding to the serviceability limit states and for the deflection corresponding to the maximum load carrying capacity of SFRSCC beam, respectively, were determined from the following equation:

$$I_F = \frac{F^{FRC} - F^{ref}}{F^{ref}} \times 100 \quad (1)$$

When F^{FRC} and F^{ref} correspond to F_{SLS}, it is evaluated the I_F for the serviceability limit state analysis, $I_{F(SLS)}$, whereas the I_F for the ultimate limit state analysis, $I_{F(ULS)}$, is obtained when the maximum forces (F_{ULS}) are used in the evaluation of (1). The values of $I_{F(SLS)}$ and $I_{F(USL)}$ are included in Table 4. These values indicate that the reinforcement of 45 kg/m^3 of fibres provided a gain in the load carrying capacity at the u_{SLS} deflection that ranged from 29% to 77%. This gain decreased with the increase of ρ_{sl}. In terms of the maximum load of the beams, this tendency was almost the same, since this gain varied from 23% to 74%, with an increase of the gain with the decrease of ρ_{sl}.

Table 2 - Increase provided by fibre reinforcement in terms of load carrying capacity at serviceability ($I_{F(SLS)}$) and at ultimate ($I_{F(ULS)}$) limit state analysis.

Designation	$I_{F(SLS)}$ (%)	$I_{F(ULS)}$ (%)
L_6	77.13	73.90
L_8	51.79	42.48
L_10	28.94	22.82

FC: fibre content in kg/m^3

3 APPRAISING THE POTENTIALITIES OF FRC FOR THE TOTAL REPLACEMENT OF CONVENTIONAL REINFORCEMENT IN ELEMENTS FAILING IN SHEAR

3.1 Introduction

The application of stirrups in concrete elements, especially in those of hollow section or composed of thin walled components, mobilize significant labour time, resulting in important financial charges. In structural concrete elements of buildings in seismic risk zones, the density of steel stirrups and hoops may difficult to obtain the desired concrete quality. Due to this type of reasons, the substitution of stirrups per steel fibres has been studied by several researchers (Casanova 1995, Casanova *et al.* 2000, Barragan 2002, Gettu *et al.* 2004).

Casanova (1995) concluded that steel fibres may substitute significant percentages of steel stirrups, especially when high strength concrete is used, since the fibre reinforcement mechanisms increase with the increase of the concrete strength, as long as fibre rupture is avoided. This Author also verified that the depth of the cross section of the beams has a significant influence in the fibre reinforcement performance, since as deeper was the cross section as less efficient was the steel fibre reinforcement.

Experimental results evidenced that beams reinforced only with steel fibres showed a similar, or even better, post cracking behaviour than reference beams with the minimum amount of steel stirrups (Meda *et al.* 2005). When used in beams reinforced with steel stirrups, steel fibres significantly improved their shear resistance. Steel fibres also reduce the width of shear cracks, thus improving the concrete durability and structural integrity (Meda *et al.* 2005).

3.2 Experimental program

3.2.1 Test series, specimens, mix compositions, test setup and monitoring system

The six series of high strength concrete (HSC) indicated in Table 5 were developed, varying the dosage of steel fibres (0, 60 and 75 kg/m^3). Table 6 includes the six designed mix compositions. The steel fibres already presented in the previous section were also used in this experimental program. For each mix composition three cylinders (150 mm diameter and 300 mm height), three cubes of 150 mm edge, and four prismatic specimens (600×150×150 mm^3) were cast and tested to assess the compression and bending behaviour of the developed concrete compositions. To evaluate the influence of the percentage of fibres in shear resistance of HSC elements, three point bending tests with shallow beams of 800×170×150 mm^3 dimensions were carried out (distance between supports equal to 720 mm).

Table 5 - Series of HSC designed for the experimental program.

Series	f_{cm} (MPa)	Content of steel fibres (kg/m^3)
f_{cm50}_*NoFibres*	50	0
f_{cm50}_*FC60*	50	60
f_{cm50}_*FC75*	50	75
f_{cm70}_*NoFibres*	70	0
f_{cm70}_*FC60*	70	60
f_{cm70}_*FC75*	70	75

The experimental program was composed of twenty four shallow beams, four beams for each series: two of plain concrete and two with two steel bars of 20 mm diameter as the tensile longitudinal reinforcement, a relatively high reinforcement ratio in order to force the occurrence

of shear failure in these two beams. The geometry of the beams and the arrangement of the reinforcement are represented in Fig. 11.
The tests were executed with a servo-controlled equipment of maximum load capacity of 300 kN. The tests were controlled by the displacement transducer of the actuator, at a displacement rate of 3 μm/s.

Table 6 – HSC mix compositions designed for the experimental program (per m^3 of concrete).

Series	Cement (kg)	Water (dm^3)	SP (kg)	LF (kg)	Coarse agg.2 (kg)	Coarse agg.1 (kg)	Fine agg. (kg)	Fine sand (kg)	Steel fibres (kg)
f_{cm50}_NoFibres	300.00	120.46	5.36	114.00	308.98	309.19	503.35	586.99	0.00
f_{cm50}_FC60	300.00	120.46	7.01	228.00	294.27	294.46	457.59	533.63	60.00
f_{cm50}_FC75	300.00	120.46	7.01	228.00	286.14	286.51	448.93	560.56	75.00
f_{cm70}_NoFibres	400.00	114.00	7.84	200.00	303.10	303.30	471.32	549.63	0.00
f_{cm70}_FC60	400.00	114.00	10.65	342.00	282.50	282.69	439.29	512.28	60.00
f_{cm70}_FC75	400.00	114.00	10.65	342.00	266.11	266.45	417.50	521.32	75.00

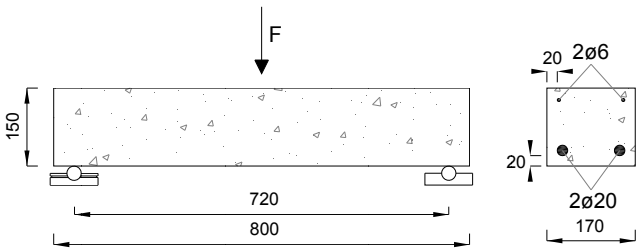

Fig. 11 – Shallow beams and ordinary reinforcement.

3.2.2 Results and analysis

Compression behaviour

The compression stress-strain relationship, $\sigma_c - \varepsilon_c$, for each testing series of HSSFRC is represented in Fig. 12. These results were obtained at the 14th day after the concrete cast operations. Each curve is the average of three specimens. As expected, in the pre-peak phase all HSC have similar behaviour, with a small increase on the compressive strength with the increase of the fibre content. In the post-peak phase, the residual strength is higher as larger is the content of fibres and is significantly higher than in the corresponding plain concrete. The main obtained results are included in Table 7. Each result is the average of three tests. The average compressive strength was a little bit lower than the target values.

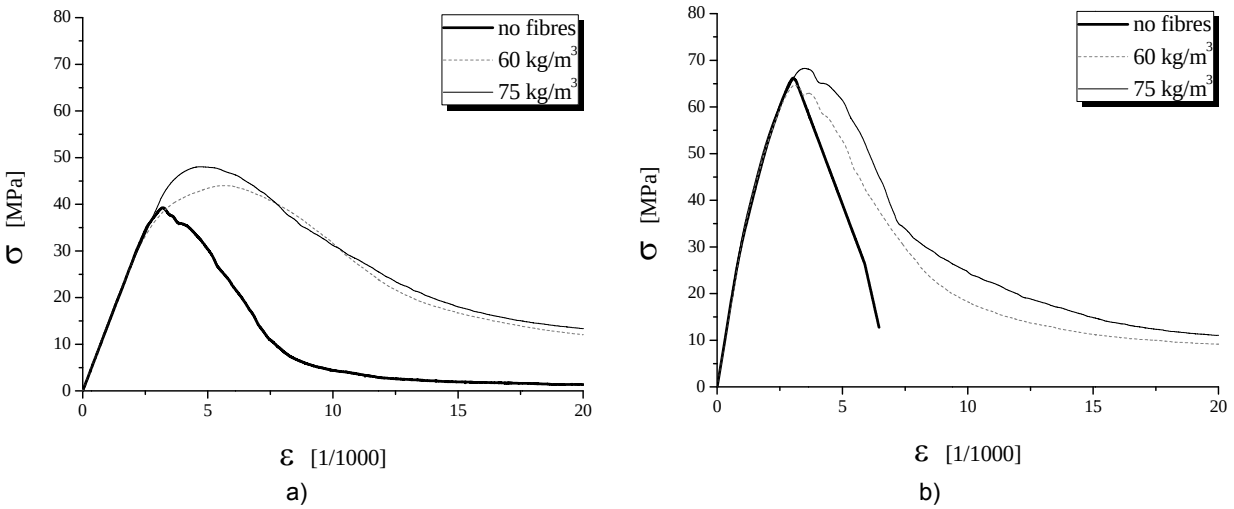

Fig. 12 - Stress-strain curves of a) f_{cm50} and b) f_{cm70} series.

Table 7 - Mechanical characterization of the tested series: compression tests (average of 3 specimens)

Series	E_c (GPa)	f_{cm} (MPa)	Strain at compressive strength (%)
f_{cm50}_NoFibres	36.31 (8.51)	41.74 (2.76)	0.350 (0.25)
f_{cm50}_FC60	37.05 (2.90)	46.58 (0.78)	0.415 (0.11)
f_{cm50}_FC75	39.01 (0.81)	48.10 (0.28)	0.377 (0.13)
f_{cm70}_NoFibres	48.41 (1.44)	66.38 (0.45)	0.310 (0.10)
f_{cm70}_FC60	45.68 (0.36)	65.73 (3.33)	0.337 (0.36)
f_{cm70}_FC75	43.75 (0.97)	66.08 (2.06)	0.343 (0.24)

() Coefficient of variation

Flexural behaviour

Apart the geometry of the notch in the prismatic specimens, the remaining RILEM TC 162-TDF recommendations (2003) for the characterization of the flexural behaviour of SFRC were adopted. Effectively, the preliminary beams started to be tested with a notch of 2-3 mm thick and 25±1 mm depth, as recommended by RILEM TC, but several cracks were formed outside the notched section. According to RILEM TC 162-TDF these tests are not valid because the energy dissipated in the fracture process can not be accurately evaluated, since the real area of the cracks formed is almost impossible of being determined. The depth of the notch that assured the formation of a single crack in the notched plan was determined from experimental trials, having been obtained a notch depth of 74 mm, which is almost half the depth of the specimen cross section. The force-deflection curves, F-δ, obtained in the tested series are depicted in Fig. 13. Each curve is the average of the F-δ relationship recorded in three specimens. The influence of steel fibres is very evident. The series without fibres show a deflection softening behaviour, with abrupt load decay after peak load. The series with fibres show a very ductile behaviour. After the crack initiation a deflection hardening phase happened in all series reinforced with fibres. The softening phase starts for the identical values of deflection (around 2.0 mm) in all series. The influence of the fibre dosage on the post-cracking flexural strength is higher in the f_{cm50} series. In fact, the difference between the series with 60 kg and 75 kg of fibres per cubic meter of concrete was more pronounced in f_{cm50} than in the f_{cm70} series. The softening branch in the f_{cm70} series with 60 kg/m^3 of steel fibres has more pronounced load decay than in all the other series. This shows that the same dosage of steel fibres may cause different levels of reinforcement effectiveness in concretes of different strength

class. Due to the better fibre-matrix bond properties provided by f_{cm70}, 60 kg/m^3 assured a peak load higher than the one registered in the f_{cm50} with the same content of fibres. However, since the number of fibres crossing the fracture surface is almost the same in both series, and the energy accumulated up to peak load of the f_{cm70} is higher than in f_{cm50}, the load decay in the softening phase of f_{cm70} was more pronounced than in f_{cm50} series.

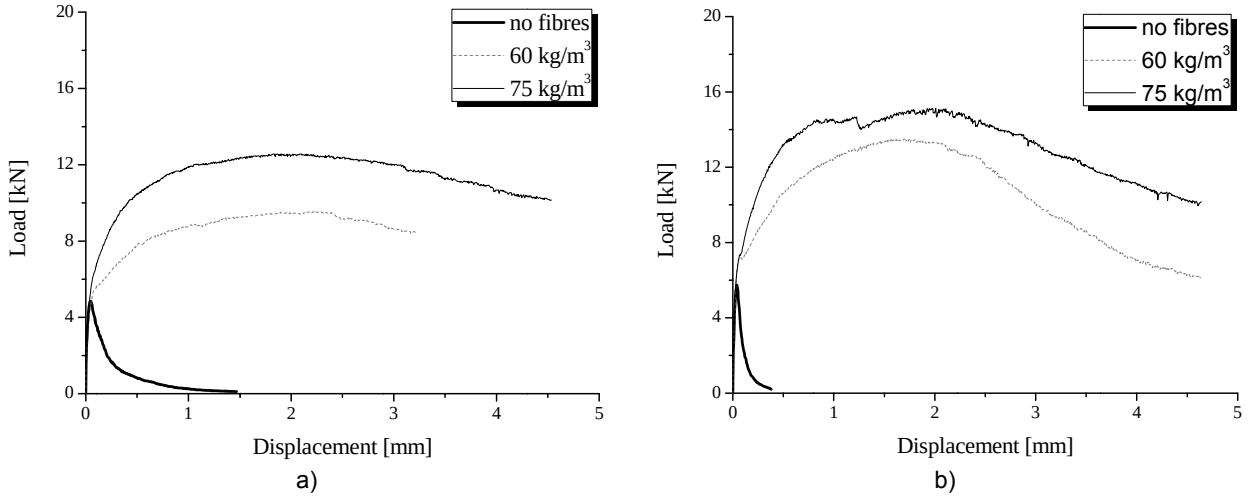

Fig. 13 - Load-displacement curves of the bending tests with prismatic specimens of a) f_{cm50} and b) f_{cm70} series.

Behaviour in shear

The load *vs* midspan deflection curves obtained from the three point loading tests carried out with the shallow beams are presented in Fig. 14. Table 8 includes the force at a deflection corresponding to the serviceability limit state (L/400 with L being the beam span length in mm), F_{SLS}, and to the ultimate limit state (maximum force), F_{ULS}, registered in the tests. To estimate the contribution of fibre reinforcement at serviceability and at ultimate limit states, the values of the $I_{F(SLS)}$ and $I_{F(ULS)}$, established in equation (1), were determined. These values are indicated in Table 9, from which it can be concluded that fibre reinforcement provided a contribution for the load carrying capacity of the shallow beams, at deflection SLS analysis, ranging from 43% to 72%, while for the ULS analysis, the fibre reinforcement effectiveness varied from 80% to 118%.

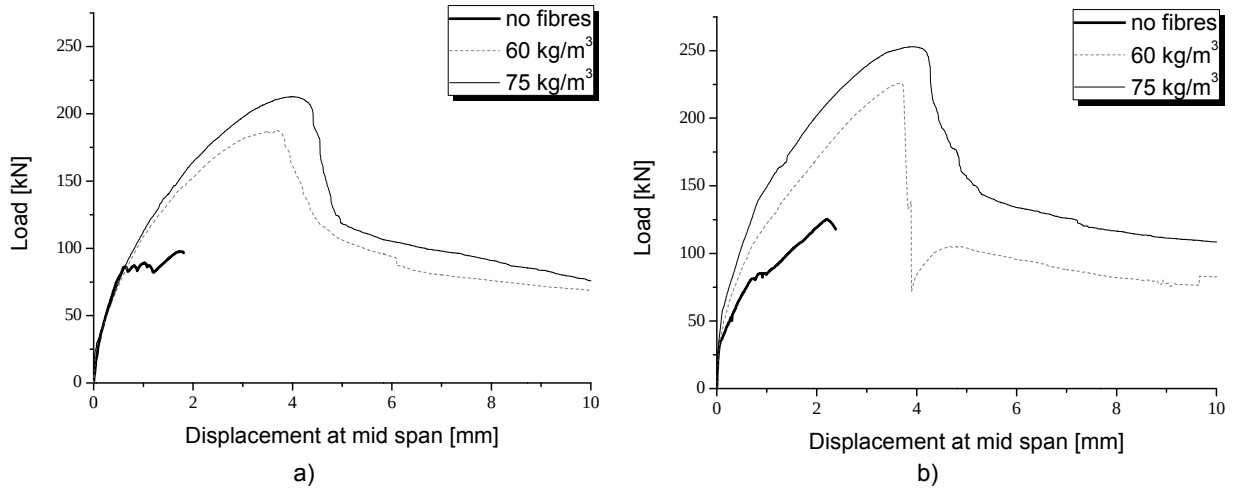

Fig. 14 - Load-displacement curves for the a) f_{cm50} and b) f_{cm70} series.

Table 8 - Values (in kN) for the F_{SLS} and F_{ULS}.

Series	F_{SLS}			F_{ULS}		
	F^{ref}	F^{FRC}	F^{FRC}	F^{ref}	F^{FRC}	F^{FRC}
	[FC=0]	[FC=60]	[FC=75]	[FC=0]	[FC=60]	[FC=75]
f_{cm50}	97.35	146.06	154.83	97.66	187.50	212.73
f_{cm70}	112.10	160.29	192.36	125.23	225.82	252.90

FC: fibre content in kg/m^3

Table 9 - Fibre reinforcement effectiveness indexes for serviceability ($I_{F(SLS)}$) and ultimate ($I_{F(ULS)}$) limit state analysis.

Series	$I_{F(SLS)}$ (%)		$I_{F(ULS)}$ (%)	
	[FC=60]	[FC=75]	[FC=60]	[FC=75]
f_{cm50}	50.04	59.05	91.99	117.84
f_{cm70}	42.98	71.59	80.33	101.96

FC: fibre content in kg/m^3

Failure modes

As Fig. 15 shows, all tested RC beams failed in shear. However, the number of flexural cracks formed up to the occurrence of the shear failure crack increased with the increase of the content of steel fibres. Furthermore, it is visible that the inclination of the shear failure crack (angle of the shear crack plan with the beam longitudinal axis) decreased with the increase of the content of fibres, which justifies the resulting benefits of fibre reinforcement, since larger area of crack bridged by fibres is available, and more favourable inclination of the fibre resisting tensile force is mobilized for the shear resistance. Moreover, due to the crack opening arrestment offered by fibres bridging the shear crack plans, a diffuse crack pattern occurred in the vicinity of the shear failure crack, which contributed for the increase of energy dissipation and for the more ductile failure mode observed in HSSFRC beams, in comparison to HSC beams (see also Fig. 14).

a) b) c)

Fig. 15 - Crack pattern in f_{cm50} series: a) without fibres, b) with 60 kg/m^3 and c) with 75 kg/m^3 of fibres.

3.2.3 Predictive performance of the RILEM TC 162-TDF

As a result of the "Brite-Euram Project 97-4163, BRPR-CT98-0813" (2002), where numerical and experimental research was developed, RILEM TC 162-TDF (2003) proposed a formulation in a close format of CEB-FIP Model Code (1993). According to this formulation, the shear resistance of a concrete element reinforced with steel stirrups, steel fibres and ordinary longitudinal reinforcement is given by:

$$V_{Rd3} = V_{cd} + V_{fd} + V_{wd} \quad (2)$$

where V_{cd} and V_{wd} represent the contribution of concrete and steel stirrups, respectively, for the shear resistance, determined according to the CEB-FIP Model Code (1993), and V_{fd} is the contribution of fibre reinforcement:

$$V_{fd} = 0.7\, k_f\, k_l\, \tau_{fd}\, b_w\, d \qquad \text{[N]} \tag{3}$$

where k_f and k_l are factors that for the cross sections of the shallow beams assume a unitary value, b_w and *d* are the width and the depth of the cross section, and,

$$\tau_{fd} = 0.12\, f_{eqk,3} \qquad \text{[N/mm}^2\text{]} \tag{4a}$$

or

$$\tau_{fd} = 0.12\, f_{Rk,4} \qquad \text{[N/mm}^2\text{]} \tag{4b}$$

where $f_{eqk,3}$ and $f_{Rk,4}$ are the characteristic value of the equivalent and residual flexural tensile strength parameters determined under the recommendations of RILEM TC 162-TDF (2003).
Applying this formulation to the experimental program carried out in the present work, the contribution of steel fibres for the concrete shear resistance was evaluated. The obtained values, included in Table 10, show that the smaller safety factor in series reinforced with fibres was 1.88. It should be mentioned that in the calculations of Table 10 average values were used for the equivalent and residual flexural strengthening parameters, since the use of characteristics values lead to too high safety factors due to the relatively high coefficient of variation (COV) that was obtained for these parameters. A possible alternative to decrease the COV of these parameters is the use of experimental programs composed of 10 to 12 bending specimens (in the present experimental program the series of notched beam tests were composed of three specimens).

Table 10 - Contribution of steel fibres to the concrete shear resistance according to the RILEM TC 162-TDF.

Series	f_{cm} (kN)	f_{ck} (kN)	*Vcd* (kN)	$\tau_{fd,1}$ [(1)] (MPa)	$\tau_{fd,2}$ [(2)] (MPa)	V_{fd} [(1)] (kN)	V_{fd} [(2)] (kN)	V_{Rd} [(1)] (kN)	V_{Rd} [(2)] (kN)	SF,1 [(3)]	SF,2 [(3)]
f_{cm50}_*NoFibres*	41.74	33.74	30.36	-	-	-	-	30.36	-	1.61	-
f_{cm50}_*FC60*	46.58	38.58	31.65	0.97	0.91	18.23	17.15	49.88	48.80	1.88	1.92
f_{cm50}_*FC75*	48.10	40.10	32.16	0.87	0.82	16.29	15.34	48.45	47.50	2.20	2.24
fcm70_ NoFibres	66.39	58.39	36.45	-	-	-	-	36.45	-	1.72	-
f_{cm70}_*FC60*	65.73	57.73	36.31	1.13	0.82	21.15	15.45	57.46	51.76	1.95	2.17
f_{cm70}_*FC75*	66.08	58.08	36.38	0.90	0.49	16.95	9.19	53.33	45.57	2.36	2.72

[(1)]Considering $\tau_{fd} = 0.12\, f_{eqk,3}$ [N/mm^2]; [(2)] Considering $\tau_{fd} = 0.12\, f_{Rk,4}$ [N/mm^2]; [(3)] Ratio between V_{exp} and $V_{Rd(1)}$ (or $V_{Rd(2)}$).

4 NUMERICAL MODEL

4.1 Introduction

This chapter describes the numerical model developed for the analysis of the box-culvert. The main features introduced in the FEMIX 4.0 FEM-based computer program (Sena-Cruz *et al.* 2007) are indicated in the following section, and the concrete, soil, and soil-concrete interface constitutive models are described in Sections 4.3 to 4.5.

4.2 Software for nonlinear material analysis

The new numerical facilities were introduced into FEMIX 4.0, which is a computer code whose purpose is the analysis of structures by the Finite Element Method (FEM). The Author of the present work is a co-founder of FEMIX. This code is based on the displacement method, being a large library of types of finite elements available. All these types of elements can be simultaneously included in the same analysis, with the exception of some incompatible combinations. The analysis may be static or dynamic and the material behavior may be linear or nonlinear. Data input is facilitated by the possibility of importing CAD models. Post processing is performed with a general purpose scientific visualization program named *drawmesh*. In the same nonlinear analysis several nonlinear models may be simultaneously considered. Interface elements with appropriate friction laws and nonlinear springs may also be simultaneously considered. The global response history is recorded in all the sampling points for selected post-processing. Advanced numerical techniques are available, such as the Newton-Raphson method combined with arc-length techniques and path dependent or independent algorithms. When the size of the systems of linear equations is very large, a preconditioned conjugate gradient method can be advantageously used.
For the analysis of FRC infrastructures taking into account the soil-structure interaction, the following new facilities were implemented into FEMIX: i) the simulation of phasing construction; ii) elasto-plasticity constitutive models for soil (Mohr-Coulomb, Drucker-Prager criterion, and Ottosen criteria were implemented); the smeared crack model to simulate the crack initiation and propagation in box-culvert, already existing for plane stress state problems, was adapted for modelling the behaviour of structures considered in plane strain state conditions, such is the case of the structural problems analyzed in the present study; iii) opening-sliding constitutive model for interface finite elements to simulate the soil-concrete interaction. The main characteristics of these constitutive models are described in next sections.

4.3 Constitutive model for the FRC

The concrete cracking is simulated under the framework of the multi-directional fixed smeared crack concepts (Rots, 1988). According to the present model, the total strain increment of the cracked concrete, $\Delta\underline{\varepsilon}$, is the addition of the strain increment in the fracture zone, $\Delta\underline{\varepsilon}^{cr}$, with the strain increment of the concrete between cracks, $\Delta\underline{\varepsilon}_e^{co}$:

$$\Delta\underline{\varepsilon} = \Delta\underline{\varepsilon}_e^{co} + \Delta\underline{\varepsilon}^{cr} \tag{5}$$

For the present study, concrete between cracks is assumed in elastic (*e*) behaviour, but elasto-plastic behaviour can also be simulated (Barros *et al.* 2004). The concrete is governed by the following constitutive equation:

$$\Delta\underline{\sigma}=\underline{D}^{co}\Delta\underline{\varepsilon}^{co} \tag{6}$$

where, in the case of uncracked linear-elastic material, $\underline{D}^{co}$ becomes with the designation of $\underline{D}_e^{co}$, with the following format:

$$\underline{D}^{co} \rightarrow \underline{D}_e^{co} = \frac{E_c}{(1+\upsilon_c)(1-2\upsilon_c)} \begin{bmatrix} (1-\upsilon_c) & \upsilon_c & 0 \\ \upsilon_c & (1-\upsilon_c) & 0 \\ 0 & 0 & \frac{1-2\upsilon_c}{2} \end{bmatrix} \tag{7}$$

where υ_c and E_c are the Poisson coefficient and the Young's modulus of the uncracked concrete, respectively. In the present study, the structure is considered in the *yz* plane and the stress component orthogonal to the structure, σ_x, is not considered in the present crack constitutive model, i.e., it is assumed that cracks do not form in parallel to the plane of the structure. When cracked, $\underline{D}^{co}$ has the following configuration (Sena-Cruz 2004):

$$\underline{D}^{co} \rightarrow \underline{D}_{ecr}^{co} = \left\{ \underline{D}_e^{co} - \underline{D}_e^{co}\, \underline{T}^{crT} \left[\underline{D}^{cr} + \underline{T}^{cr}\, \underline{D}_e^{co}\, \underline{T}^{crT} \right]^{-1} \underline{T}^{cr}\, \underline{D}_e^{co} \right\} \tag{8}$$

where $\underline{T}^{cr}$ is a matrix defining the orientation of the cracks formed at a sampling point. If *m* cracks occurs at a sampling point:

$$\underline{T}^{cr} = \left[\underline{T}_1^{cr} \quad , \quad \underline{T}_i^{cr} \quad , \quad \underline{T}_m^{cr} \right]^T \tag{9}$$

where the crack orientation of a generic *i*th crack is defined by the matrix $\underline{T}_i^{cr}$:

$$\underline{T}_i^{cr} = \begin{bmatrix} \cos^2\theta_i & \sin^2\theta_i & 2\sin\theta_i\cos\theta_i \\ -\sin\theta_i\cos\theta_i & \sin\theta_i\cos\theta_i & \cos^2\theta_i - \sin^2\theta_i \end{bmatrix} \tag{10}$$

with θ_i being the angle between *y* and the normal to the *i*th crack plane (see Fig. 16). In (8) $\underline{D}^{cr}$ is a matrix including the constitutive law of the cracks:

$$\underline{D}^{cr} = \begin{bmatrix} \underline{D}_1^{cr} & \dots & \underline{0} & \dots & \underline{0} \\ \dots & \dots & \dots & \dots & \dots \\ \underline{0} & \dots & \underline{D}_i^{cr} & \dots & \underline{0} \\ \dots & \dots & \dots & \dots & \dots \\ \underline{0} & \dots & \underline{0} & \dots & \underline{D}_m^{cr} \end{bmatrix} \tag{11}$$

where $\underline{D}_i^{cr}$ is the *i*th crack constitutive law:

$$\underline{D}_i^{cr} = \begin{bmatrix} D_{I,i}^{cr} & 0 \\ 0 & D_{II,i}^{cr} \end{bmatrix} \tag{12}$$

with D_I^{cr} and D_{II}^{cr} being the crack fracture mode I and mode II stiffness modulus, respectively. The crack system of a sampling point is governed by the following relationship:

$$\Delta\underline{\sigma}^{cr} = \underline{D}^{cr}\,\Delta\underline{\varepsilon}^{cr} \tag{13}$$

where $\Delta\underline{\sigma}^{cr}$ is the vector of the incremental crack stress components (Fig. 16):

$$\Delta\underline{\sigma}^{cr} = \left[\Delta\sigma_{n,1}^{cr} \quad \Delta\tau_{nt,1}^{cr} \quad \ldots \quad \Delta\sigma_{n,i}^{cr} \quad \Delta\tau_{nt,i}^{cr} \quad \ldots \quad \Delta\sigma_{n,m}^{cr} \quad \Delta\tau_{nt,m}^{cr}\right]^T \tag{14}$$

and $\Delta\underline{\varepsilon}^{cr}$ is the vector of the incremental crack strain components:

$$\Delta\underline{\varepsilon}^{cr} = \left[\Delta\varepsilon_{n,1}^{cr} \quad \Delta\gamma_{nt,1}^{cr} \quad \ldots \quad \Delta\varepsilon_{n,i}^{cr} \quad \Delta\gamma_{nt,i}^{cr} \quad \ldots \quad \Delta\varepsilon_{n,m}^{cr} \quad \Delta\gamma_{nt,m}^{cr}\right]^T \tag{15}$$

The D_I^{cr} of (12) is characterised by the fracture parameters (Fig. 17), namely, the tensile strength, $\sigma_{n,1}^{cr} = f_{ct}$, the fracture energy, G_f, the shape of the softening law and the crack bandwidth, l_b. Fibre reinforcement mechanisms are reflected, mainly, on the energy dissipated in the mode I fracturing process and on the shape of the softening branch. For fibre contents used in current concrete applications, the remaining concrete properties are only marginally affected by fibre addition (Barros 1995). The crack mode I stiffness is simulated by the trilinear diagram represented in Fig. 17.
The fracture mode II modulus, D_{II}^{cr}, is obtained from the equation (Rots 1988, Barros 1995):

$$D_{II}^{cr} = \frac{\beta}{1-\beta} G_c \tag{16}$$

where G_c is the concrete shear modulus and,

$$\beta = \left[1 - \frac{\varepsilon_n^{cr}}{\varepsilon_{n,u}^{cr}}\right]^p \quad \text{(p=1, 2 or 3)} \tag{17}$$

is the shear retention factor.

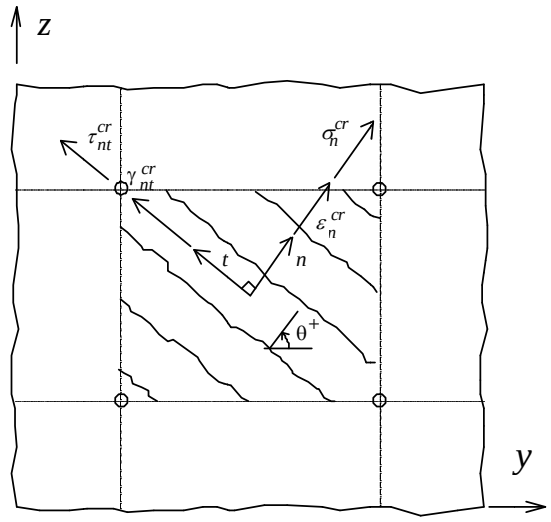

Fig. 16 - Crack stress and crack strain components.

Fig. 17 - Stress-strain diagram for modelling the crack opening process.

Based on previous research on the development of SFRSCC for laminar structures (Barros 2008), the values for the properties indicated in Table 11 were taken for the simulation of the box-culvert, assuming this structure will be precast with this material, in order to verify the possibility of replacing the conventional reinforcement used in the types of box-culverts in analysis in the present study. The values of the fracture parameters were obtained from inverse analysis (Pereira *et al.* 2008). In the numerical simulation, l_b was considered equal to the square root of the area of the finite element, a maximum of two cracks per sampling point can be formed, the threshold angle for the control of opening a new crack in a sampling point was considered equal to 30 degrees, and p=3 was taken for the evaluation of the shear retention factor, in eq. (17).

Table 11 – Values of the properties for the SFRSCC crack constitutive model.

γ_c (kN/m^3)	E_c (GPa)	υ_c (-)	f_c (MPa)	$f_{ct}=\sigma_{n,1}^{cr}$ (MPa)	G_f (N/mm)	$\varepsilon_{n,2}^{cr}/\varepsilon_{n,u}^{cr}$	$\sigma_{n,2}^{cr}/\sigma_{n,1}^{cr}$	$\varepsilon_{n,3}^{cr}/\varepsilon_{n,u}^{cr}$	$\sigma_{n,3}^{cr}/\sigma_{n,1}^{cr}$
24.0	39.0	0.2	45.0	2.90	4.0	0.05	0.60	0.20	0.20

4.4 Constitutive model for the soil

4.4.1 Mohr Coulomb

For the simulation of the behaviour of the embankment soil, the Mohr-Coulomb (M-C) yield criterion was implemented into FEMIX V4.0. This function has the following format:

$$f\left(\underline{\sigma},c,\phi\right)=\frac{1}{3}I_1\sin\phi+J_2^{1/2}\left(\cos\theta-\frac{1}{\sqrt{3}}\sin\theta\sin\phi\right)-c\cos\phi \tag{18}$$

where c and ϕ are the soil cohesion and the friction angle, I_1 and J_2 are the first invariant and the second deviatoric stress invariant, respectively, (Chen and Han 1988), and

$$\theta=\frac{1}{3}\arcsin\left(-\frac{3\sqrt{3}}{2}\frac{J_3}{J_2^{3/2}}\right) \tag{19}$$

with J_3 being the third deviatoric stress invariant (Chen and Han 1988).
For a plane strain problem, the stress vector has four components:

$$\underline{\sigma}=\left\{\sigma_x \quad \sigma_y \quad \sigma_z \quad \tau_{yz}\right\}^T \tag{20}$$

According to the plasticity theory principles, the flux vector $\underline{a}$ is composed by the four derivatives of the yield function with respect to each of the four stress components:

$$\underline{a}=\left\{\frac{\partial f\left(\underline{\sigma}\right)}{\partial\sigma_x} \quad \frac{\partial f\left(\underline{\sigma}\right)}{\partial\sigma_y} \quad \frac{\partial f\left(\underline{\sigma}\right)}{\partial\sigma_z} \quad \frac{\partial f\left(\underline{\sigma}\right)}{\partial\tau_{yz}}\right\}^T \tag{21}$$

The equation that defines each of the four flux vector $\underline{a}$ components is, in indicial notation, the following:

$$a_i = \frac{\partial f\left(\underline{\sigma}\right)}{\partial \sigma_i}$$
$$= \frac{1}{3}\sin\phi\,\frac{\partial I_1}{\partial \sigma_i} + \frac{1}{2}\frac{\partial J_2}{\partial \sigma_i} J_2^{-1/2}\left(\cos\theta - \frac{1}{\sqrt{3}}\sin\theta\sin\phi\right) + \tag{22}$$
$$\frac{\sqrt{3}}{2}\frac{\frac{\partial J_3}{\partial \sigma_i} J_2 - \frac{3}{2}\frac{\partial J_2}{\partial \sigma_i} J_3}{J_2^2\sqrt{1-\left(\sin 3\theta\right)^2}}\left(\sin\theta + \frac{1}{\sqrt{3}}\cos\theta\sin\phi\right)$$

To avoid the singularities at $\theta = \pm 30^\circ$ the a_i takes the following form:

$$a_i = \frac{1}{3}\sin\phi\,\frac{\partial I_1}{\partial \sigma_i} + \frac{1}{2}\frac{\partial J_2}{\partial \sigma_i} J_2^{-1/2}\left(\frac{\sqrt{3}}{2} \pm \frac{1}{2\sqrt{3}}\sin\phi\right) \quad (\text{- for } \theta = 30^\circ \text{ and + for } \theta = -30^\circ) \tag{23}$$

The derivatives of the stress invariants are in Section A.3 of the Annex, while the first and second derivatives of the Mohr-Coulomb yield function are in Section A.4 of the Annex. To accomplish the Mohr-Coulomb yield surface, the return-mapping algorithm was implemented (Hofstetter and Mang 1995), having been obtained the following two equations system (for the generic *l* iteration of a load step *n*+1):

$$\begin{bmatrix} \underline{D}_s^{-1} + \Delta\lambda_{n+1}^l \dfrac{\partial^2 f_{n+1}^l}{\partial\left(\underline{\sigma}_{n+1}^l\right)^2} & \dfrac{\partial f_{n+1}^l}{\partial \underline{\sigma}_{n+1}^l} \\ \dfrac{\partial f_{n+1}^l}{\partial \underline{\sigma}_{n+1}^l} & 0 \end{bmatrix} \begin{bmatrix} d\underline{\sigma}_{n+1}^l \\ d\lambda_{n+1}^l \end{bmatrix} = -\begin{bmatrix} \underline{r}_{\varepsilon_{n+1}}^l \\ r_{f_{n+1}}^l \end{bmatrix} \tag{24}$$

that is solved by the Newton-Raphson numerical technique, where

$$\left(\Delta\underline{\varepsilon}_{n+1}^p\right)^l = \Delta\lambda_{n+1}^l \frac{\partial f_{n+1}^l}{\partial \underline{\sigma}_{n+1}^l} \tag{25}$$

is the strain vector of the plastic strain increments, and

$$r_{\underline{\varepsilon}_{n+1}}^l = -\left(\underline{\varepsilon}_{n+1}^p\right)^l + \underline{\varepsilon}_n^p + \Delta\lambda_{n+1}^l \frac{\partial f_{n+1}^l}{\partial \underline{\sigma}_{n+1}^k}$$
$$r_{f,n+1}^l = f_{n+1}^l\left(\underline{\sigma}_{n+1}^l\right) \tag{26}$$

are the residues that should be minimized. The final converged values of the unknowns ($\underline{\sigma}_{n+1}^l, \Delta\lambda_{n+1}^l$) for the step *n*+1 are obtained through the successive summation of the increments determined at each iteration from the linear system of eqs. (24):

$$\underline{\sigma}_{n+1}^l = \underline{\sigma}_n + \sum_{i=1}^{l} d\underline{\sigma}_{n+1}^i$$
$$\Delta\lambda_{n+1}^l = \sum_{i=1}^{l} d\lambda_{n+1}^i \tag{27}$$

In Section A1 of the Annex the generalization of the returning-mapping algorithm is described, in order to be capable of treating the case where the yield function shrinks or expands according to a hardening or softening law. The consistent tangent elasto-plastic

constitutive matrix can be easily obtained following the procedures described in Section A.2 of the Annex, resulting (for the case where hardening/softening is not considered for the parameters of the material):

$$d\underline{\sigma}_{n+1} = \left(\underline{H} - \frac{\underline{H}\dfrac{\partial f_{n+1}}{\partial \underline{\sigma}_{n+1}}\dfrac{\partial f_{n+1}}{\partial \underline{\sigma}_{n+1}}\underline{H}}{\dfrac{\partial f_{n+1}}{\partial \underline{\sigma}_{n+1}}\underline{H}\dfrac{\partial f_{n+1}}{\partial \underline{\sigma}_{n+1}}} \right) d\underline{\varepsilon}_{n+1} \tag{28}$$

where

$$\underline{H} = \left(\underline{D}_s^{-1} - \Delta\lambda_{n+1}\frac{\partial^2 f_{n+1}}{\partial\left(\underline{\sigma}_{n+1}\right)^2} \right)^{-1} \tag{29}$$

To appraise the implementation of the Mohr-Coulomb criterion, the RC footing of 3 m width supported on soil, represented in Fig. 18a is analyzed. Both the RC footing and soil support are considered in plane strain state. The adopted finite element mesh, composed of eight nodded finite elements for both the soil and RC footing is represented in Fig. 18b.

The footing is considered in linear elastic behaviour with an elasticity modulus of 30 GPa and null Poisson coefficient. For the soil the values indicated in Table 12 were considered.

Table 12 – Values of the properties for the Mohr-Coulomb soil constitutive model.

E_s (MPa)	ν_s (-)	γ_s (kN/m^3)	c (kPa)	ϕ ($^\circ$)
150.0	0.3	16.5	20.0	35.0

Fig. 19 represents the relationship between the vertical strain and the M-C yield function at the 4th integration point (IP) of the element 146, of coordinates x_2=1.394 m, x_3=11.162 m (Fig. 18). This figure shows that, after a linear elastic-behaviour, the soil represented by this IP enters in its plastic phase with a yield stress of 16.38 kPa ($f\left(\underline{\sigma}, c, \phi\right) = c\cos\phi = 20\cos 35 = 16.38\,kPa$), when the load applied to the RC footing, p, is about 107 kPa.

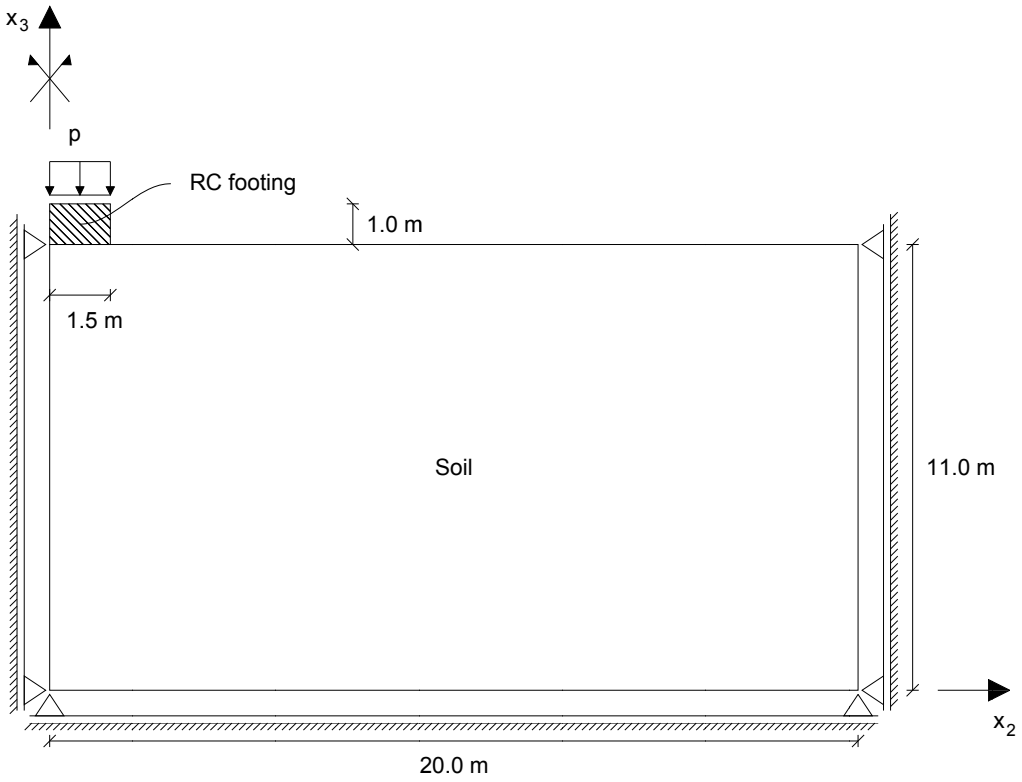

(a)

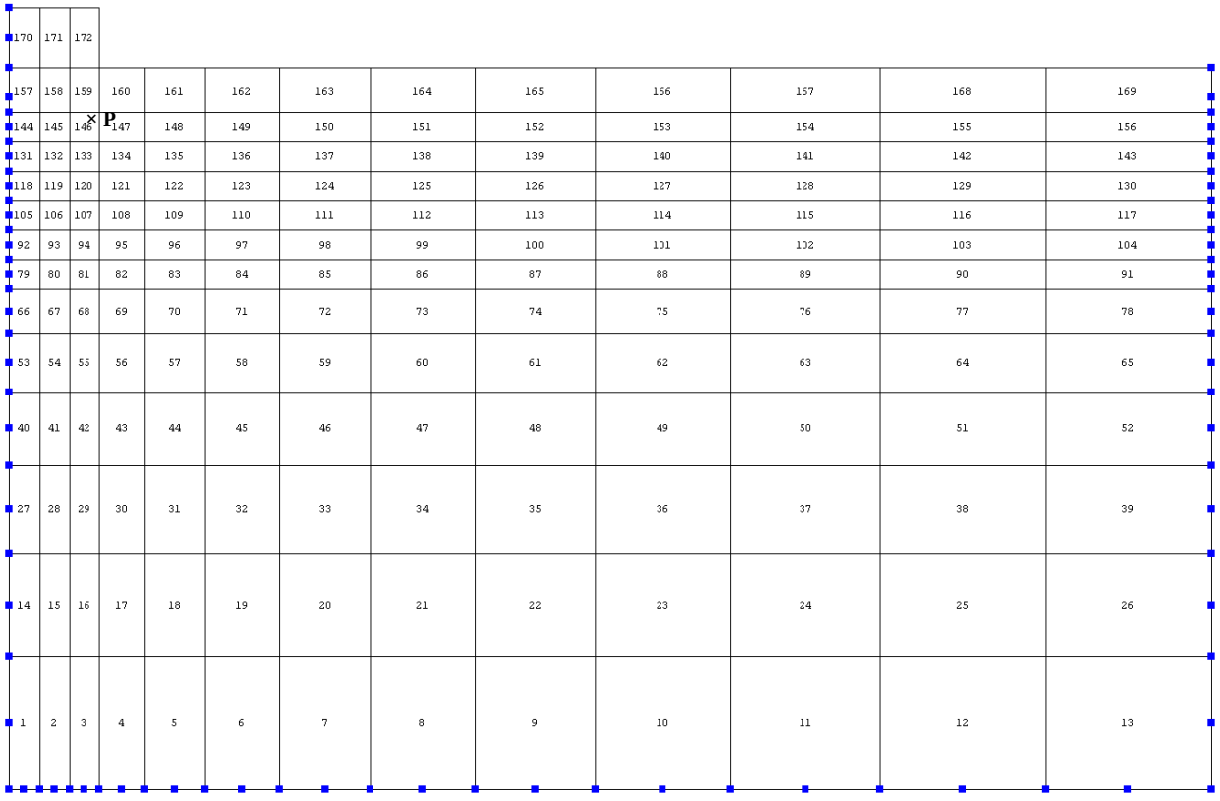

(b)

Fig. 18 – Stiff footing supported on soil: (a) geometry and (b) mesh.

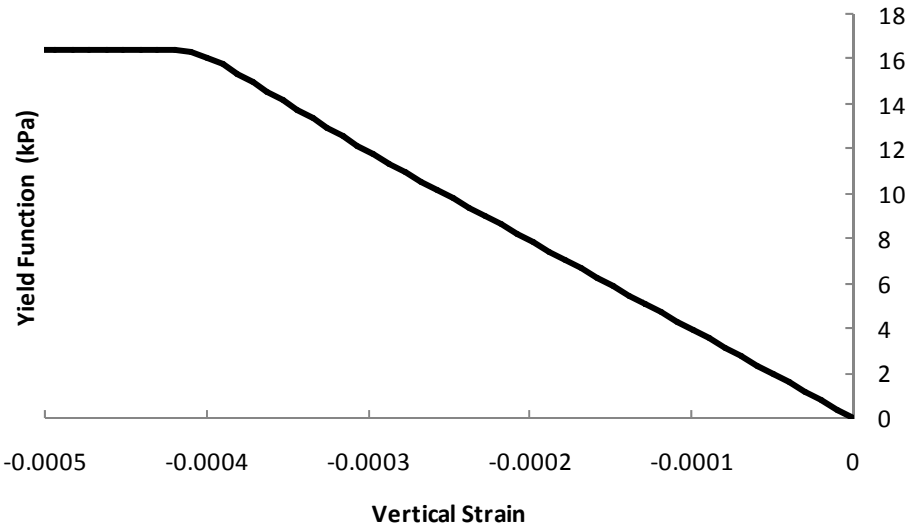

Fig. 19 – Evolution of the Mohr-coulomb yield function in the integration point P (4th IP of element 146), of coordinates 1.394 m, 11.162 m (see Fig. 18)

Fig. 20 represents the IPs that yielded for a p=175kPa, while the x_2 and the x_3 displacement fields at this load level are represented in Fig. 21.

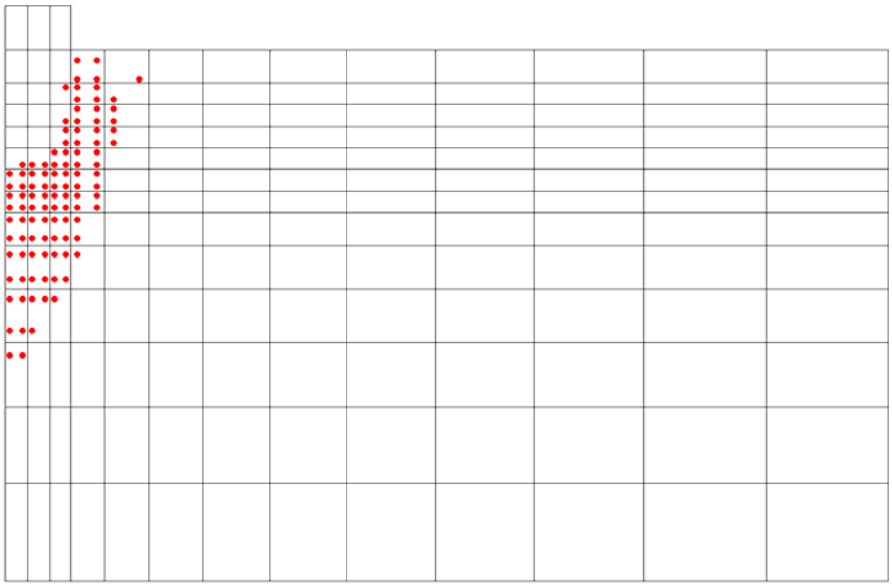

Fig. 20 – Soil yielded IPs at p=175 kPa.

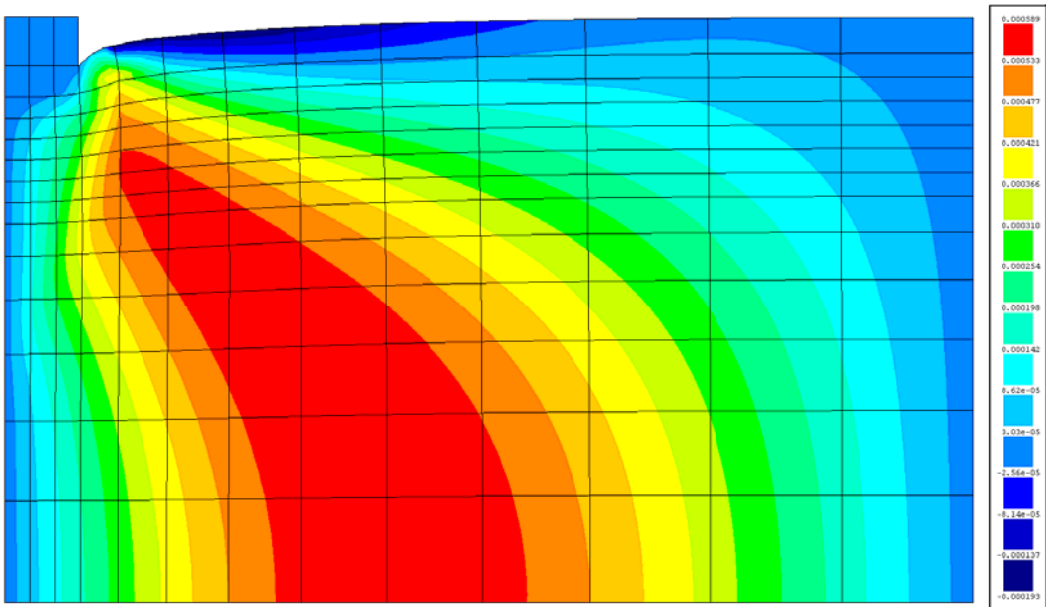

(a)

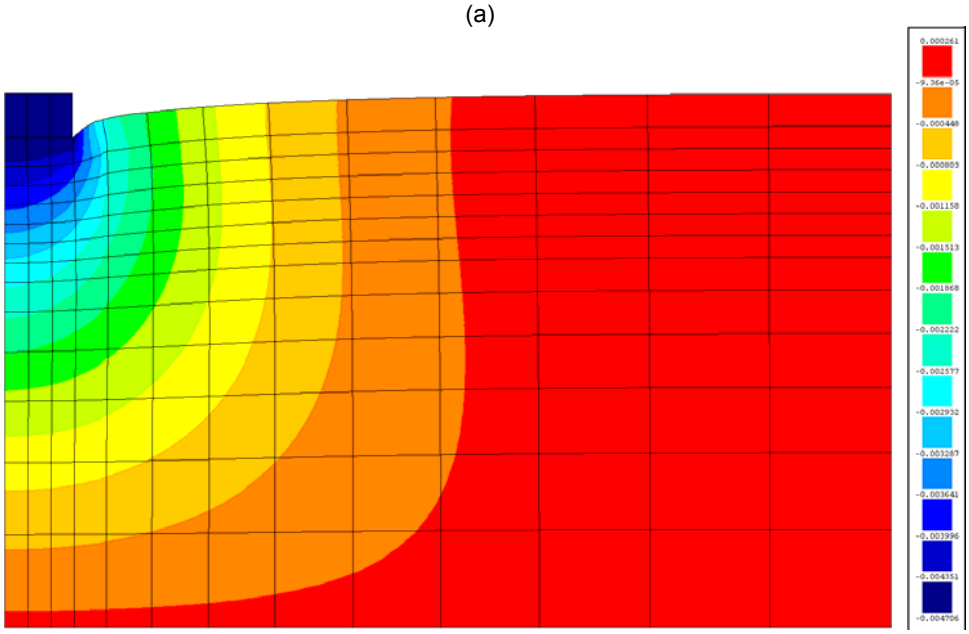

(b)

Fig. 21 – Displacement field of (a) x_2 and in (b) x_3 direction, at p=175 kPa.

4.4.2 Drucker-Prager

The Drucker-Prager (D-P) yield criterion was also implemented into FEMIX V4.0 for the simulation of the behaviour of the soil. This function has the following format:

$$f\left(\underline{\sigma},k\right)=\frac{2\sin\phi\left(k\right)}{\sqrt{3}\left(3\pm\sin\phi\left(k\right)\right)}I_1+J_2^{1/2}-\frac{6c\left(k\right)\cos\phi\left(k\right)}{\sqrt{3}\left(3\pm\sin\phi\left(k\right)\right)} \tag{30}$$

being the cohesion and the friction angle dependent of a hardening/softening parameter, *k*, thereafter designated as internal variable, in order to simulate the variation of the cohesion and the friction angle with the plastic strain evolution. In Eq. (30), when plus sign is adopted

the Drucker-Prager function passes in the inner corners of the Mohr-Coulomb surface, while the adoption of the minus sign leads to the function to pass in the outer corners of the Mohr-Coulomb surface.
If it is assumed:

$$\alpha(k) = \frac{2\sin\phi(k)}{\sqrt{3}\left(3 \pm \sin\phi(k)\right)} \tag{31}$$

$$\beta(k) = \frac{6c(k)\cos\phi(k)}{\sqrt{3}\left(3 \pm \sin\phi(k)\right)} \tag{32}$$

than Eq. (30) becomes,

$$f\left(\underline{\sigma}, k\right) = \alpha(k) I_1 + J_2^{1/2} - \beta(k) \tag{33}$$

The parameters α and β can be established in terms of the uniaxial compressive and uniaxial tensile strength (f_c, f_t) of the material (Chen and Han 1988):

$$\alpha = \frac{m-1}{\sqrt{3}(1+m)} \tag{34}$$

$$\beta = \frac{2 f_c}{\sqrt{3}(1+m)} \tag{35}$$

being

$$m = \frac{f_c}{f_t} \tag{36}$$

The return mapping algorithm described in Section A.1 of the Annex and the formulation to obtain the consistent tangent elasto-plastic constitutive matrix, exposed in Section A.2 of this Annex, are both applicable for the Drucker-Prager criterion, since they were established in order to be reused for any yield criterion. The first and the second derivatives of the Drucker-Prager yield function are presented in Section A.5 of the Annex.

To appraise the implementation of the Drucker-Prager criterion, the problem represented in Fig. 18 was analyzed, considering the soil properties indicated in that Section and performing two analyses, one assuming the Drucker-Prager function passes in the inner corners of the Mohr-Coulomb surface, and in the other it passes in the outer corners. Fig. 22 represents the relationship between the vertical strain and the D-P yield function at the 4th integration point (IP) of the element 146, of coordinates x_2=1.394 m, x_3=11.162 m (Fig. 18). This figure shows that, after a linear elastic-behaviour (some perturbations occurs just before entering in the yield phase due to the nonlinear behaviour of surrounding soil), the soil represented by this IP enters in its plastic phase. For the case of D-P passing in the inner corners of the M-C, the yield stress is 15.88 kPa ($f\left(\underline{\sigma}, c, \phi\right) = 6c\cos\phi \Big/ \left(\sqrt{3}\left(3+\sin\phi\right)\right) = 6\times 20\cos 35 \Big/ \left(\sqrt{3}\left(3+\sin 35\right)\right) = 15.88$ kPa) when the load applied to the RC footing, p, is about 77 kPa, while for the case of D-P passing in the outer corners of the M-C the yield stress is 23.39 kPa ($f\left(\underline{\sigma}, c, \phi\right) = 6c\cos\phi \Big/ \left(\sqrt{3}\left(3-\sin\phi\right)\right) = 6\times 20\cos 35 \Big/ \left(\sqrt{3}\left(3-\sin 35\right)\right) = 23.39$ kPa) when the load applied to the RC footing, p, is about 210 kPa.

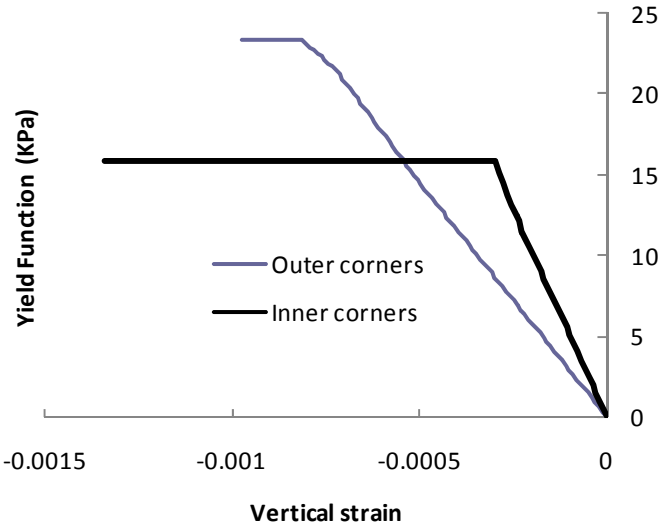

Fig. 22 – Evolution of the Drucker-Prager yield function in the integration point P (4th IP of element 146), of coordinates 1.394 m, 11.162 m (see Fig. 18)

4.5 Softening/hardening laws

In cohesive materials like soil and concrete the cohesion, in general, decreases with the increase of the plastic strain installed in the material. To simulate this phenomenon, the law:

$$c(k) = c_o e^{-\left(\frac{k}{k_c}\right)^p} \tag{37}$$

was adopted, which is represented in Fig. 23, being c_o the initial cohesion (undamaged material), k_c and p are parameters that defines the rate of degradation of the cohesion with the evolution of the internal variable k.

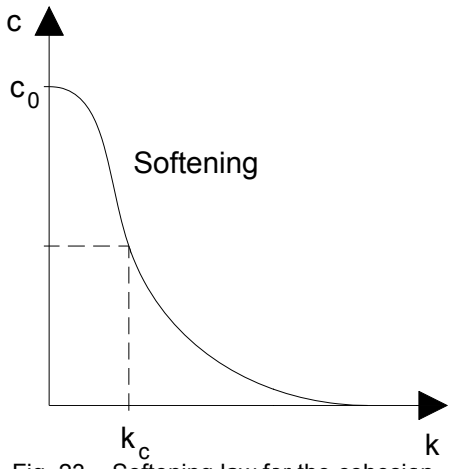

Fig. 23 – Softening law for the cohesion.

In frictional materials like some soils and cement based materials, the friction angle can decrease with the increase of the plastic strain (typical of soils) or can increase with the

increase of the plastic strain up to a certain limit (typical of cement based materials). To simulate this phenomenon the law:

$$\phi(k) = \phi_f - (\phi_f - \phi_o) e^{-\left(\frac{k}{k_f}\right)^q} \tag{38}$$

was adopted, which is represented in Fig. 24, being ϕ_o and ϕ_f the initial (undamaged material) and the final friction angle (full damaged), k_f and q are parameters that defines the rate of degradation of the friction angle with the evolution of the internal variable k.

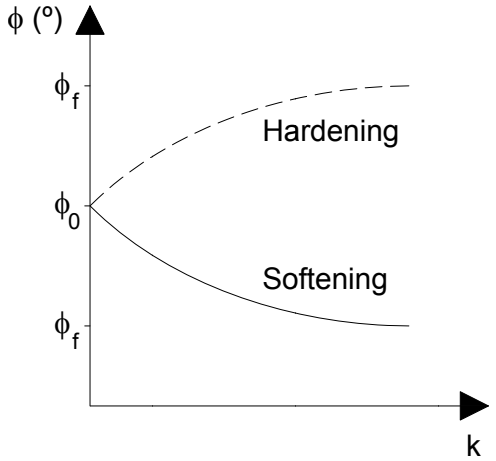

Fig. 24 – Softening/hardening law for the friction angle.

For the p and q parameters the values of 1 or 2 were assumed. The first and the second derivates of the $c(k)$ and $\phi(k)$ are in Section A.6 of the Annex.

In the present study the internal variable k was obtained according to the recommendation of the Borst and Sluys and (2007):

$$dk = \sqrt{\frac{2}{3} \Delta \underline{\varepsilon}_p^T \underline{Q} \Delta \underline{\varepsilon}_p} \tag{39a}$$

$$k = \sum dk \tag{39b}$$

$$\Delta k = k - k_o \tag{39c}$$

being $\Delta \underline{\varepsilon}_p$ evaluated from Eq. (25), k_o is the value of the internal variable of the previous converged load step and $\underline{Q}$ the diagonal matrix:

$$\underline{Q} = diag\begin{bmatrix} 1 & 1 & 1 & 0.5 \end{bmatrix} \tag{40}$$

Another alternative to calculate the k parameter is described in Section A.1 of the Annex.

To assess the influence of the values of the parameters of the cohesion evolution law and friction angle evolution law on the behaviour of a soil, a parametric study was carried out with soil element represented in Fig. 25, considered in plane strain and having the following

properties: E=20 MPa, ν=0.3. The Drucker-Prager yield function passing in the outer corners of the Mohr-Coulomb surface was adopted in the parametric study. To simulate a full uniaxial compression test, in the two top nodes of the four nodes quadrilateral finite element discretizing the specimen, descendent imposed displacements, *u*, were applied.

In Fig. 26 is depicted the relationship between the vertical strain and the vertical stress, and shows the influence of changing the value of c_o, when a constant friction angle (30° was assumed) and k_c=0.02, p=1 are adopted. The variation of the cohesion with the axial strain is represented in Fig. 27 for the three values of the c_o parameter.

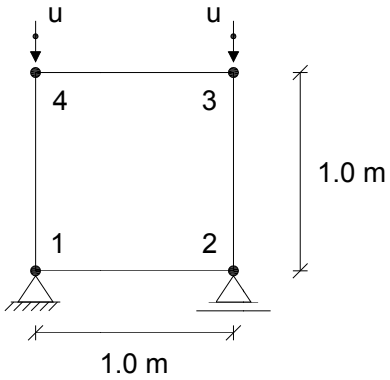

Fig. 25 – Unconfined uniaxial compression test is soil element considered in plane strain conditions.

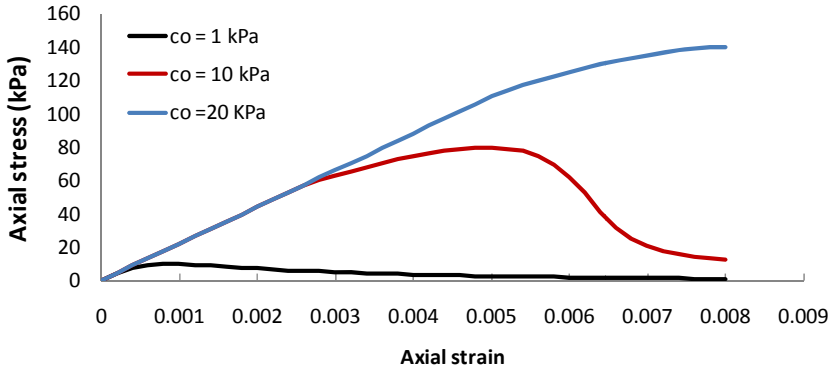

Fig. 26 – Influence of the c_o parameter on the stress-strain response.

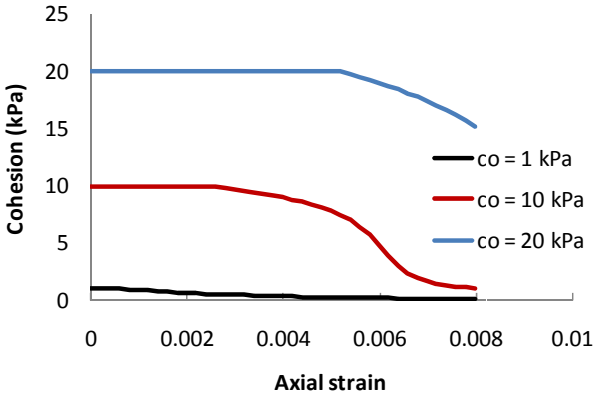

Fig. 27 – Variation of the cohesion with the axial strain for the three values of c_o parameter.

From Figs. 26 and 27 it is visible that with the increase of c_o the compressive strength increases significantly, as well the strain corresponding to axial strength. Furthermore, while cohesion is maintained constant, the stress-strain relationship is linear. When cohesion starts decrease the stress-strain response becomes nonlinear up to peak stress. The stress-strain relationship enters in a softening phase when the decrease of cohesion becomes more pronounced (the highest slope of the concave shape of the c-ε curve). After the inflection point of the curvature of the c-ε curve the stress-strain curve also changes its curvature, assuming a convex shape due to a smaller degradation of the cohesion.

In Fig. 28 is depicted the relationship between the vertical strain and the vertical stress, and shows the influence of changing the value of k_c when a constant friction angle (30° was assumed) and c_o=10 kPa and p=1 are adopted. The relationship between the axial strain and the cohesion is represented in Fig. 29 for the three values of k_c (0.001, 0.01 e 0.1).

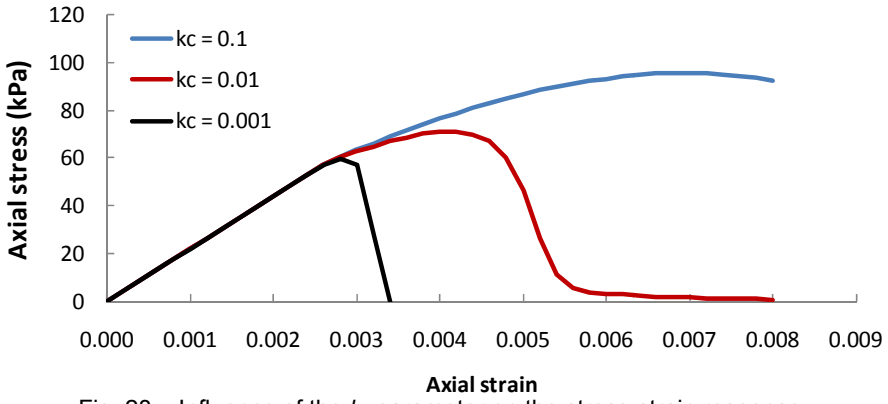

Fig. 28 – Influence of the k_c parameter on the stress-strain response.

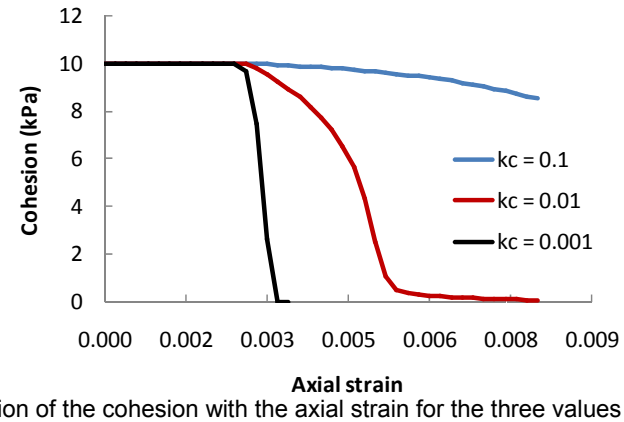

Fig. 29 – Variation of the cohesion with the axial strain for the three values of k_c parameter.

From the analysis of Figs. 28 and 29 conclusions similar to those already pointed out can be advanced. However, for the interval of values considered, the impact on the compressive strength was smaller than the registered for the interval of variation of c_o. On the other hand, the impact of k_c parameter on the post-peak phase of the stress-strain response was higher than the impact of the values of c_o. This means that the adopted softening law for the cohesion is able of reproducing the full behaviour of cohesive and friction materials of distinct strength and pseudo-ductility.

In Fig. 30 is depicted the relationship between the vertical strain and the vertical stress for distint values of $\left(\phi_f - \phi_o\right)$, when a constant cohesion (10 kPa was assumed), k_f=0.02, $\phi_o = 25^\circ$ and q=1 are adopted. The variation of the friction angle with the axial strain is represented in Fig. 31 for the four values of the $\left(\phi_f - \phi_o\right)$ parameter.

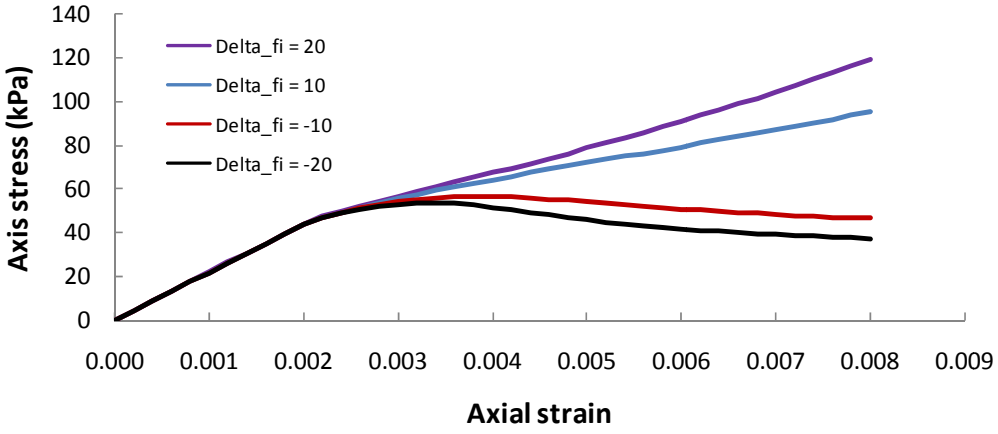

Fig. 30 – Influence of the $\left(\phi_f - \phi_o\right)$ parameter on the stress-strain response.

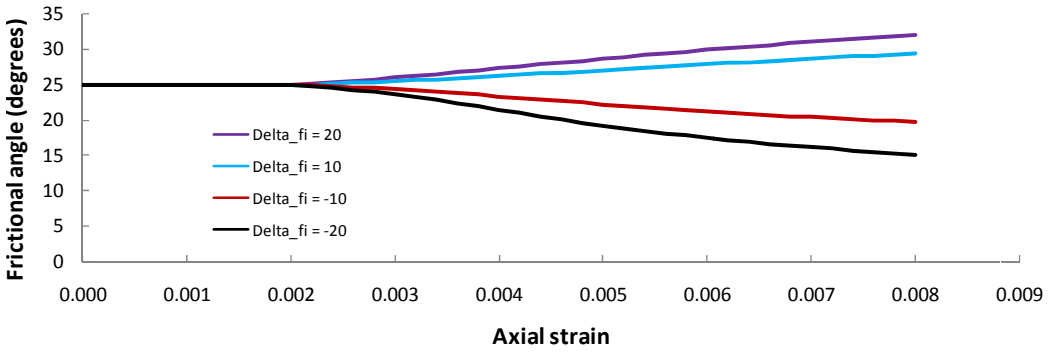

Fig. 31 – Variation of the friction angle with the axial strain for the four values of $\left(\phi_f - \phi_o\right)$ parameter.

From Figs. 30 and 31 it is visible that when the friction angle starts to decrease the stress-strain curve enters in a softening phase, while when it increases the stress-strain shows a hardening phase. A linear stress-strain relationship is obtained while friction angle has a constant value.

In Fig. 32 is depicted the relationship between the vertical strain and the vertical stress for distinct values of k_f when a constant cohesion (10 kPa was assumed), ϕ_o=25 degrees, ϕ_f =5 degrees and q=1 are adopted. The variation of the friction angle with the axial strain is represented in Fig. 33 for the three values of k_f parameter (0.001, 0.01 e 0.1).

In Fig. 34 is depicted the relationship between the vertical strain and the vertical stress for distinct values of k_f when a constant cohesion (10 kPa was assumed), ϕ_o = 25 degrees, ϕ_f =45 degrees and q=1 are adopted. The variation of the friction angle with the axial strain is represented in Fig. 35 for the three values of k_f parameter (0.001, 0.01 e 0.1).

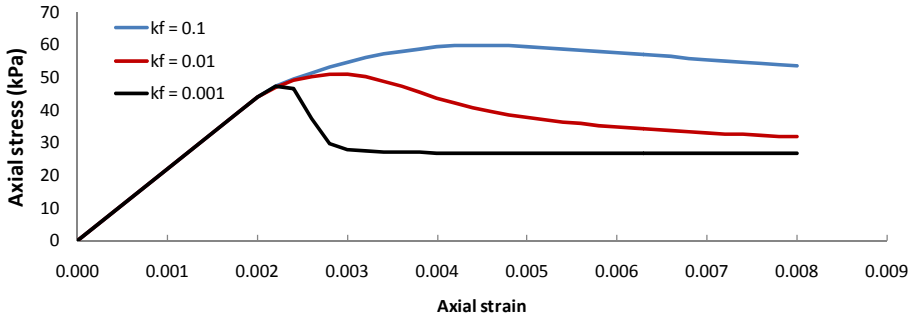

Fig. 32 – Influence of the k_f parameter on the stress-strain response.

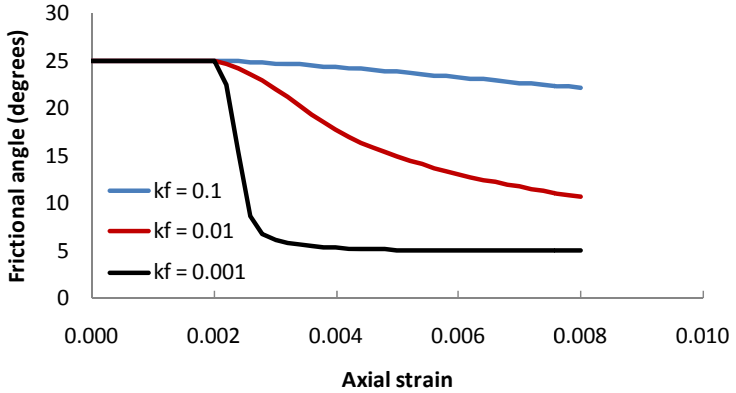

Fig. 33 – Variation of the friction angle with the axial strain for the three values of k_f parameter.

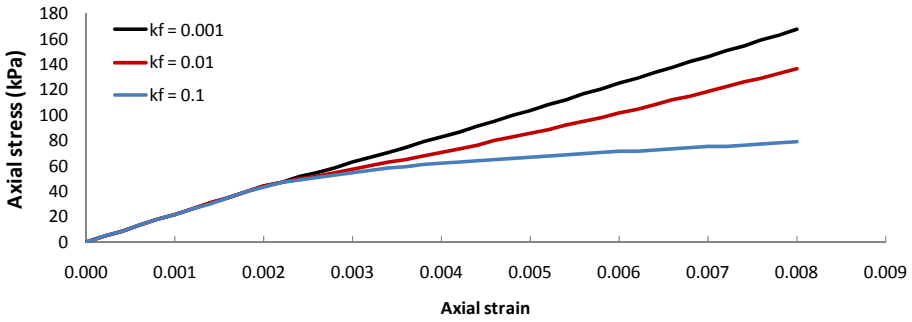

Fig. 34 – Influence of the k_f parameter on the stress-strain response.

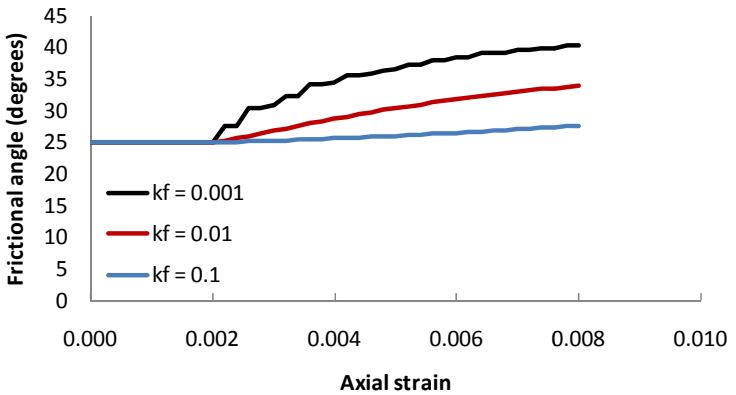

Fig. 35 – Variation of the friction angle with the axial strain for the three values of k_f parameter.

Conclusions similar to those already pointed out can be obtained from the analysis of the sets of Figs. 32 and 33 and Figs. 34 and 35.

To analyse the influence of assuming a softening law for the cohesion and for the friction angle in the case of a stiff RC foundation on a soil simulated by the M-C criteria, the problem represented in Fig. 18 is now re-analysed adopting for cohesion evolution law p=1.0 and two distinct values for the k_c parameter, and the values of 35°, 25° and 1.0 for the ϕ_o, ϕ_f and q parameters, respectively, and two distinct values for k_f (equal to the values assumed for the k_c). Fig. 36 represents the relationship between the vertical displacement of point at the footing-soil interface in the symmetry axis – positive signal was assumed for descendant displacements) and the pressure applied to the footing, s. As expected, after the linear-elastic phase the loss of load carrying capacity increases with the decrease of the k_c and k_f values, since the cohesion and the friction angles also decrease.

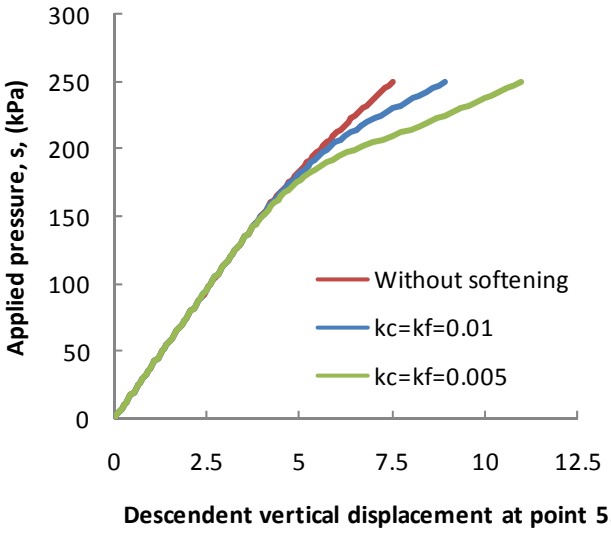

Fig. 36 – Influence of k_c and k_f values of the cohesion and friction softening laws in the footing load carrying capacity of problem of Fig. 18.

4.6 Constitutive model for the soil-concrete interface

To simulate the soil - box-culvert interaction, a six-node 2D line interface element was used, which formulation is described elsewhere (Sena-Cruz *et al.* 2004). The constitutive model of the interface element is simulated with the following relationship:

$$\underline{\sigma}' = \begin{bmatrix} \tau \\ \sigma \end{bmatrix} = \begin{bmatrix} \sigma_1' \\ \sigma_2' \end{bmatrix} = \underline{D}_I \, \Delta\underline{u}' \tag{41}$$

where $\underline{\sigma}'$ is a vector, whose components are the tangential ($\tau = \sigma_1'$) and normal ($\sigma = \sigma_2'$) stress in the local interface coordinate system, $\Delta\underline{u}'$ is a vector of the relative displacements, whose components represent the sliding, s, and the opening, w, of the interface boarders, and $\underline{D}_I$ is the constitutive matrix:

$$\underline{D}_I = \begin{bmatrix} D_t & 0 \\ 0 & D_n \end{bmatrix} \tag{42}$$

with D_t and D_n being the tangential and normal stiffness. In the present study it was assumed that no tractions can be transferred between soil and box-culvert, and a linear elastic behaviour occurs when the interface is subject to compression. For modelling the soil-concrete sliding behaviour, the law schematically represented in Fig. 37 was implemented, where:

$$\tau(s)=\begin{cases}\dfrac{\tau_o}{s_o} & if \quad 0\le|s|\le s_o\\ \tau_m\left(\dfrac{s}{s_m}\right)^{\alpha_1} & if \quad s_o<|s|\le s_m\\ \tau_m\left(\dfrac{s}{s_m}\right)^{-\alpha_2} & if \quad |s|>s_m\end{cases} \tag{43}$$

$$D_t=\begin{cases}\dfrac{\tau_o}{s_o} & if \quad 0\le|s|\le s_o\\ \alpha_1\dfrac{\tau_m}{s_m}\left(\dfrac{s}{s_m}\right)^{\alpha_1-1} & if \quad s_o<|s|\le s_m\\ -\alpha_2\dfrac{\tau_m}{s_m}\left(\dfrac{s}{s_m}\right)^{-\alpha_2-1} & if \quad |s|>s_m\end{cases} \tag{44}$$

$$\tau_m=\bar{c}-\sigma_n\tan\delta \tag{45}$$

with s_o defining the slip of the first linear branch, s_m is the slip at peak shear stress, $\bar{c}$ and δ are the cohesion and the friction angle of the soil-concrete interface, and $\sigma_n=\sigma_2'$ is negative when in compression. In (44) α_1 and α_2 are parameters that define the shape on the pre-peak nonlinear branch and the post-peak branch, respectively.

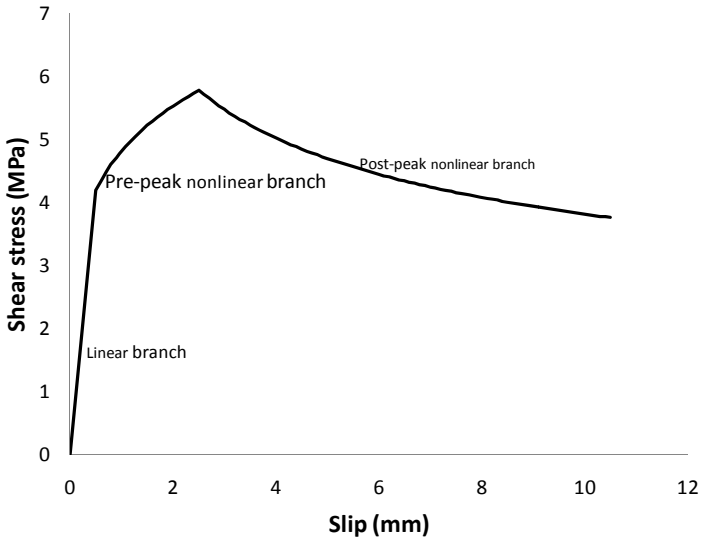

Fig. 37 – Diagram to simulate the soil-concrete sliding behaviour.

In Fig. 38 is represented an example for the appraisal of the performance of the constitutive model implemented for modelling the 2D interface finite element. This example is constituted of two relatively stiff materials modelled by four nodded plane stress elements (elements 1 and 2), with an elasticity modulus of 30000GPa, a null Poisson coefficient and a thickness of 10 mm.

The properties for the interface constitutive model are included into Table 13. To assess the variation of the updated bond strength (τ_m of Eq. (45)) and the slip-shear stress curves for increasing values of the *p*, a loading configuration composed of imposed increasing displacements in x_2 direction actuating in points 5 and 7 are applied, while a constant *p* value actuates in the top of the element number 2.

Table 13 – Values of the properties to simulate the sliding behaviour between soil and stiff material.

s_o (mm)	s_m (mm)	α_1 (-)	α_2 (-)	$\overline{c}$ (MPa)	δ ($^\circ$)	D_n (kN/m)
0.5	2.5	0.2	0.3	0.5	25.0	1.0e+03

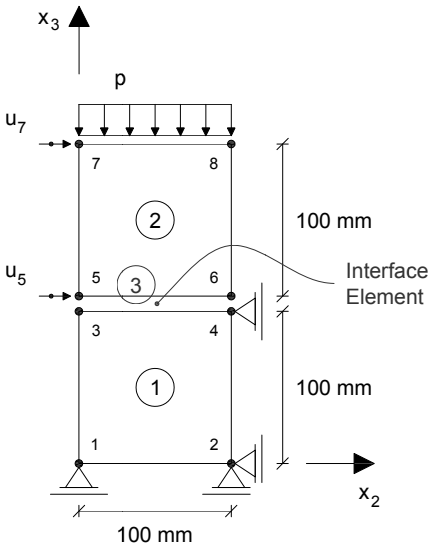

Fig. 38 – Stiff plane stress FEs (1 and 2) connected by a 2D interface element (3).

The relationship between the normal stress ($\sigma_n = \sigma_3$) and τ_m is depicted in Fig. 39, being $\sigma_3[MPa] = p[N/mm]/10[mm]$. As Figure 39 reveals, for null *p* value, i.e., for non-confined conditions, the updated bond strength is the cohesion value attributed to the interface, while the variation of the updated bond strength with the variation of the normal stress correspond to the tangent of the friction angle of the interface material.

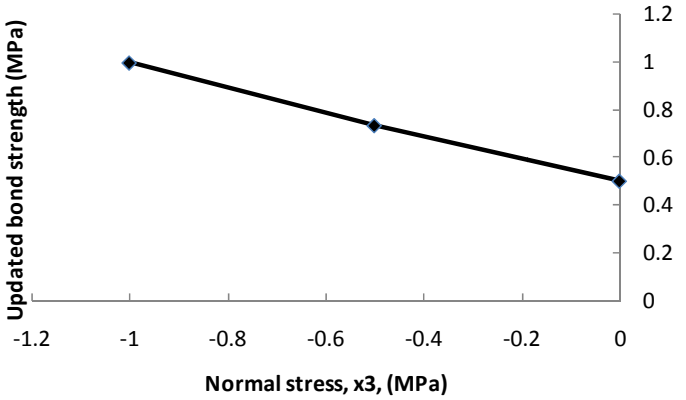

Fig. 39 – Normal stress ($\sigma_n = \sigma_3$) versus τ_m.

The relationship between the shear stress and slip is depicted in Fig. 40. As expected, with the increase of the confining pressure, *p*, the peak stress, τ_m, and consequently the $\tau_o = \tau_m \left(s_o / s_m\right)^{\alpha_1}$ and the post-peak residual shear stress also increase.

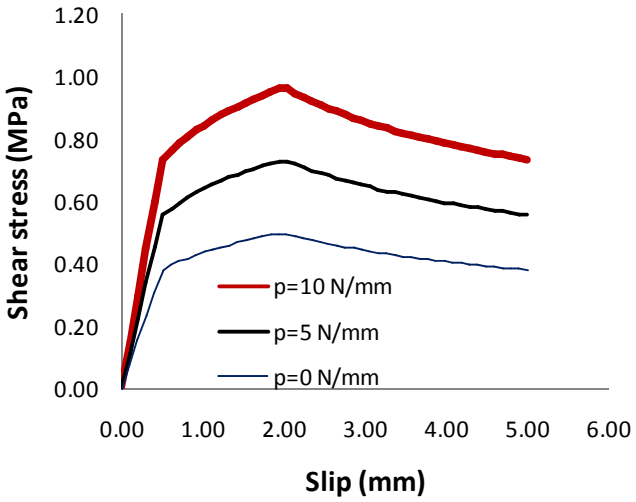

Fig. 40 – Shear stress versus slip.

4.7 Construction phases and finite element meshes

4.7.1 Phases

The simulation of the construction phases was implemented into FEMIX, being possible to have in distinct phases, finite elements of different type and constitutive models, as well as distinct support conditions and load cases. To appraise the implementation procedures of the phases into FEMIX V4.0, the cantilever beam represented in Fig. 41 is analyzed. This beam, of a material of elasticity modulus of 30 GPa, Poisson coefficient of 0.2 and specific weight of 25 kN/m^3 is built in three phases, as represented in Fig. 41. This structure is assumed as being in plane strain state and is discretized in four nodded elements, and a integration scheme of 2×2 was used to evaluate the stiffness matrix and the internal forces of the finite elements. In this analysis all the elements are considered as having linear-elastic behaviour. The elements 4 and 5 pertain to all the phases, the element 3 is active in phases 2 and 3 and the elements 1 and 2 pertain to phase 3. When each phase is analyzed in distinct separated simulations, the values of the vertical reaction, R (Fig. 41) are indicated in Table 14. The results of the distinct separated simulations and those obtained in the simulation with the constructions phases provided the same results.

The vertical deflections for the distinct separated simulations and those obtained in the simulations with the constructions phases are depicted in Fig. 42, showing that the implementation of the construction phases into FEMIX was correctly done.

Table 14 – Vertical reaction values of the phases simulations.

Distinct separated simulations			Simulations with phases
Phase 1	Phase 2	Phase 3	
50 kN			50 kN
	75 kN		75 kN
		125 kN	125 kN

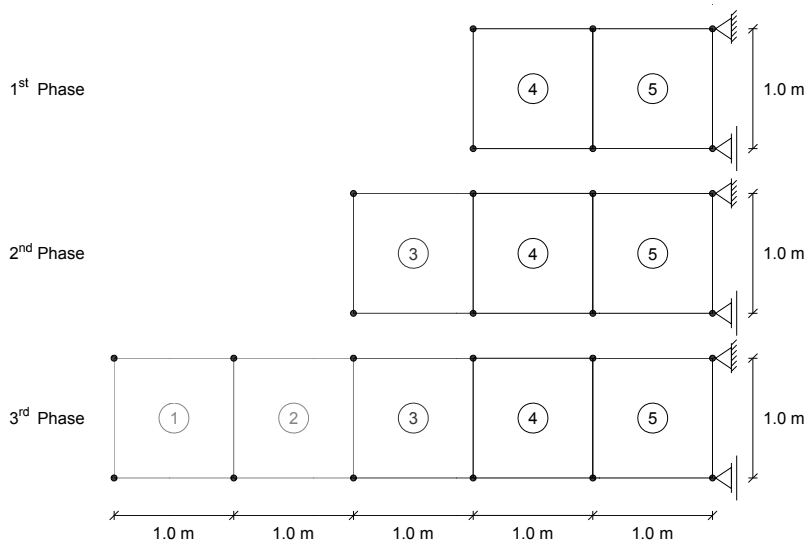

Fig. 41 – Beam built in three phases.

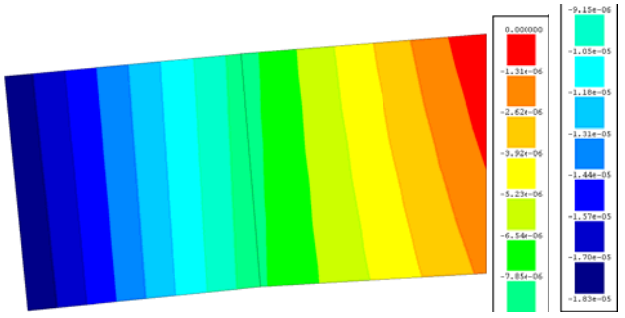

Structure corresponding to Phase 1

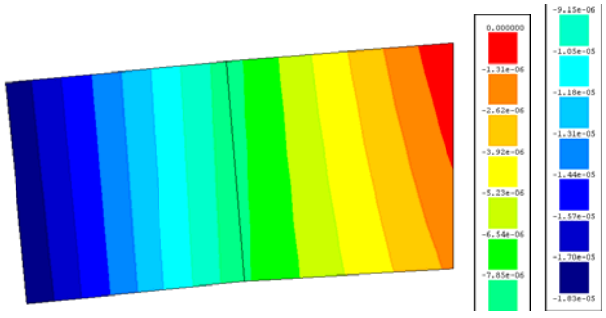

Phase 1

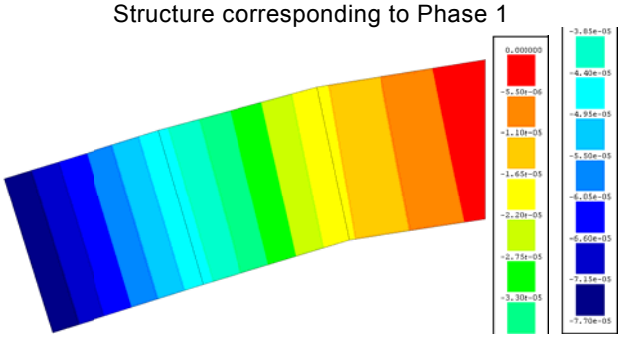

Structure corresponding to Phase 1 and 2

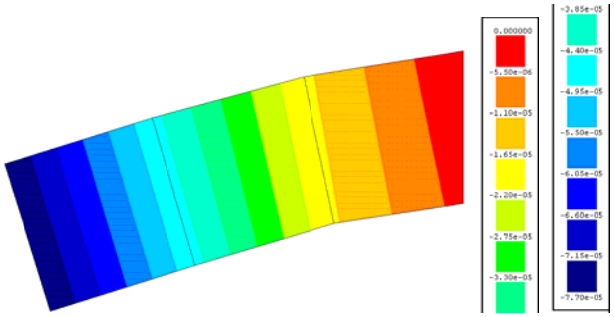

Phases 1 and 2

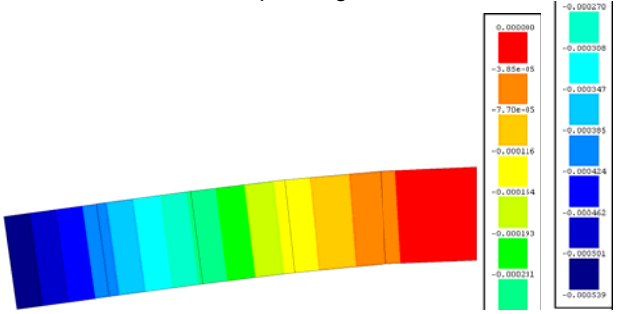

Structure corresponding to the 3 phases
(a)

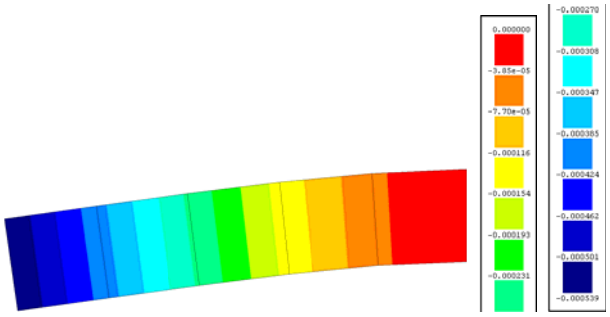

Phases 1, 2 and 3
(b)

Fig. 42 – Vertical deflection for: (a) the distinct separated simulations;.(b) simulations with the construction phases

4.7.2 Finite element meshes for the simulation of the construction phases in box-culvert

For the present study the phases and the corresponding finite element meshes are represented in Fig. 43 (these meshes corresponds to the m-50-5 box-culvert, but the strategy was the same in the iv-200-8 Box-culvert. The soil and the box-culvert were discretized by 8-noded finite elements, with a 2×2 Gauss-Legendre integration scheme, while soil-concrete interface was simulated by 6-noded interface elements with a 2 Gauss integration rule. In the analysis, a force convergence criterion with a tolerance of 0.001 was used with a Newton-Raphson technique based on the evaluation of the stiffness matrix in every iteration.

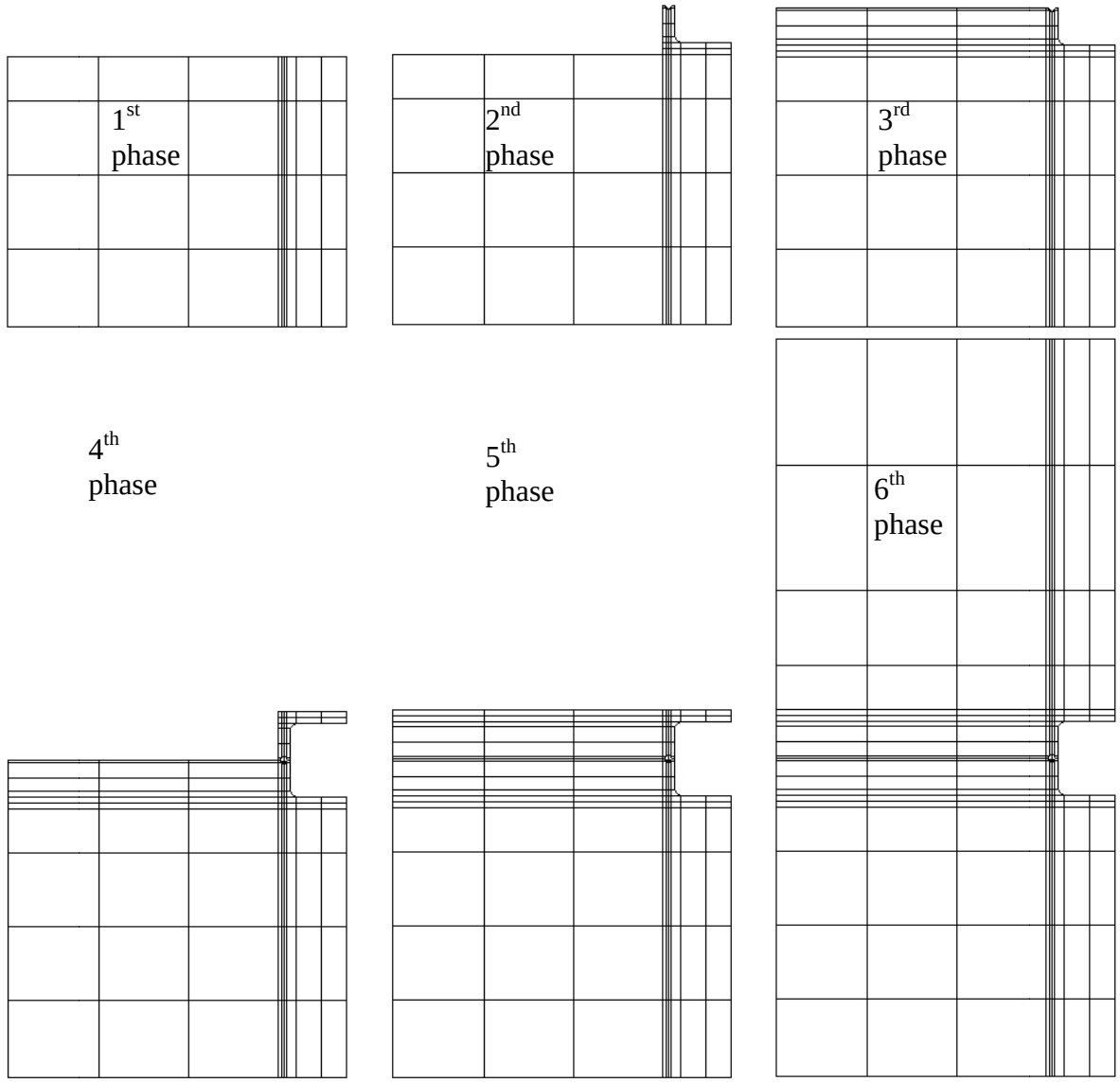

Fig. 43 – Finite element meshes of the sixth construction phases of the present study.

4.8 Load cases

In each phase the self-weigh of the intervening materials (not affected by any factor) is the load case. In the last phase, after having been applied the self-weight of the soil mobilized in this phase, an edge load applied on the surface of the embankment was increased monotonically in order to simulate a live load (represented by LL in Fig. 2) up to the attainment of a maximum crack width on the box-culvert of about 0.3 mm.

5 CASE STUDIES

5.1 M-50-5 box-culvert

In the analysis of the m-50-5 box culver, the properties for the SFRSCC are indicated in Table 11, while for the soil and soil-concrete interface are included in Tables 15 and 16, respectively. For the soil the Mohr-Coulomb criterion with constant values for the cohesion and friction angle were used.

Table 15 – Values of the properties for the Mohr-Coulomb soil constitutive model.

E_s (MPa)	ν_s (-)	γ_s (kN/m^3)	c (kPa)	ϕ ($^\circ$)
20.0	0.3	18.0	5.0	30.0

Table 16 – Values of the properties to simulate the soil-concrete sliding behaviour.

s_o (mm)	s_m (mm)	α_1 (-)	α_2 (-)	$\overline{c}$ (kPa)	δ ($^\circ$)	D_n (kN/m)
0.5	2.5	0.2	0.3	5.0	30.0	1.0e+05

Due to their relevance, only the results corresponding to the occurrence of a maximum crack width of 0.27mm are presented (the state at about the crack width limit for the serviceability design requirement for this type of structures). This crack width was estimated multiplying the maximum normal crack strain by the corresponding crack band width (square root of the area of the corresponding finite element). This crack width occurred for a live load (LL, see Fig. 2) of 20 kPa.
Fig. 44 represents the displacement fields, while Fig. 45 shows the undeformed and the deformed meshes (for an amplifier factor of the displacements of 11).

The crack pattern is illustrated in Fig. 46 showing that only flexural cracks formed on the top and bottom slabs of the two components composing the box-culvert. As Fig. 47 reveals, in the concrete in contact with the soil, at the symmetry axis of the problem, the σ_y compression stresses attained a maximum value of about 14 MPa, which is lower than the design value of the compressive strength of the SFRSCC considered for this box-culvert. In terms of σ_z stress field (Fig. 48), the maximum tensile stresses attained a value of about 1 MPa in the exterior-top part of the arms of the two components of the box-culvert, near the connection to the slab. The maximum compressive stresses occurred in the hinge connection, but the maximum value is limited to 4.6 MPa. It is also remarkable that no cracks formed in the hinge region, revealing that the connection was well designed.

The shear stress field in the box-culvert is represented in Fig. 49. The maximum τ_{yz} at the integration points in the shear critical zones is 650 kPa. According to the formulation proposed by RILEM TC 162-TDF committee (2003), the shear resistance of a concrete element reinforced with steel stirrups, steel fibres and ordinary longitudinal reinforcement is determined with the formulation described in Section 3.2.3. According to this formulation, if only fibres are used for the reinforcement of the box-culvert the $f_{eqk,3}$ needs to be higher than 7.7MPa $(V_{fd}/(b_w d) = 0.7\,\tau_{fd} = 0.7 \times 0.12\, f_{eqk,3} \geq$ 650kPa, in case of assuming the maximum shear stress as the average one in the shear critical zone). This value is higher than the values

registered experimentally for the developed cost competitive SFRSCC for this type of applications. Therefore, it is recommended to apply the minimum percentage of longitudinal conventional reinforcement (according to EC2 of 2002, $A_{s,min}$=0.0003 m^2/m, ρ_{sl}=0.23%, which corresponds to 6ϕ8/m, and 5.1 kg/m^3 of steel) as represented in Fig. 50, since for this percentage $\tau_{cd} = V_{cd} / (b_w \, d)$=503 kPa, which requires a $f_{eqk,3}$ of about 1.75MPa, which is a value that the developed SFRSCC exceeds.

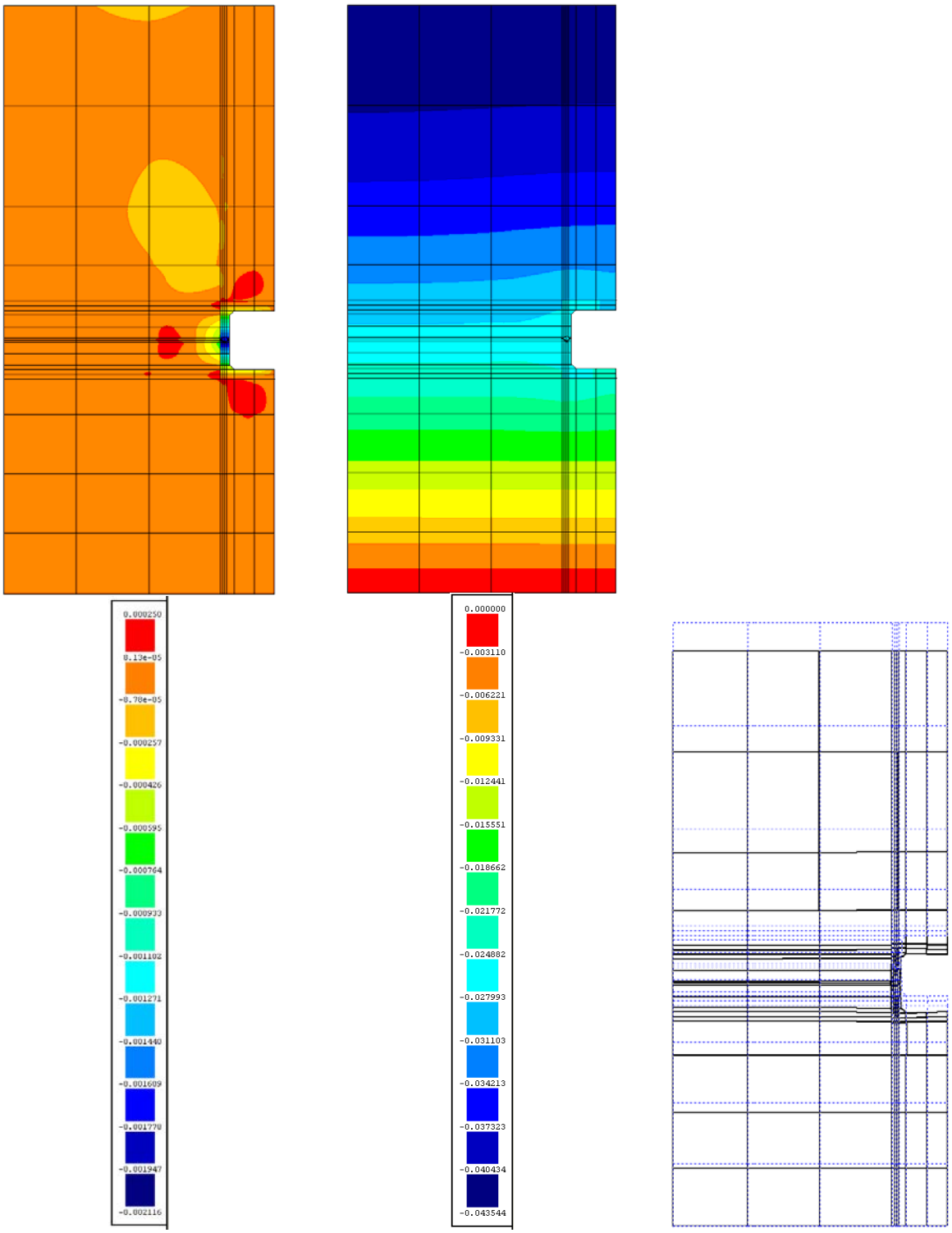

(a) (b)

Fig. 44 – Displacement field in *y* (a) and *z* (b) direction (m)

Fig. 45 – Deformed mesh.

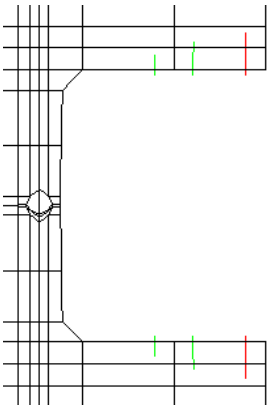

Fig 46 – Crack pattern.

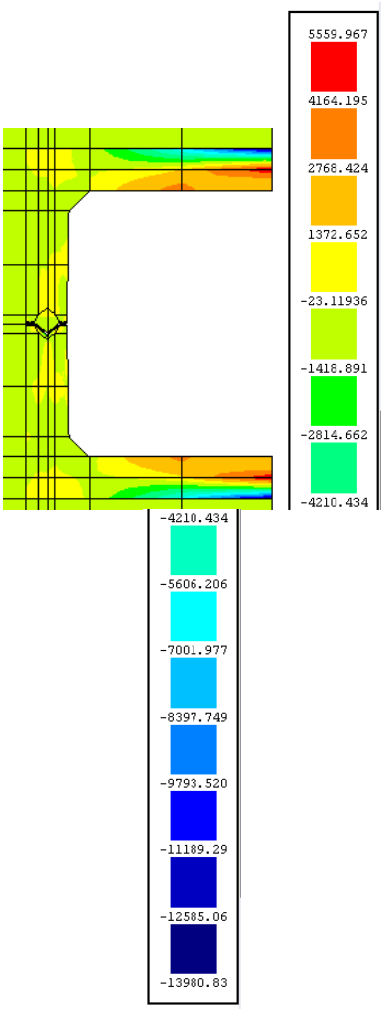

Fig. 47 – σ_y field in the box-culvert (kPa).

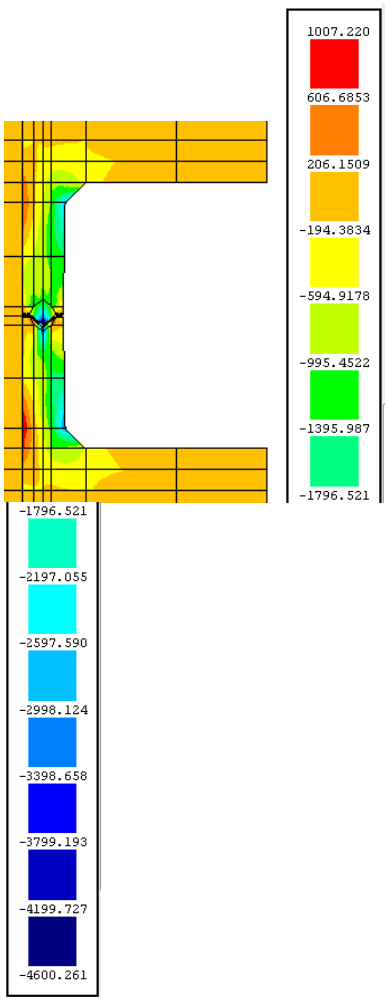

Fig. 48 – σ_z field in the box-culvert (kPa).

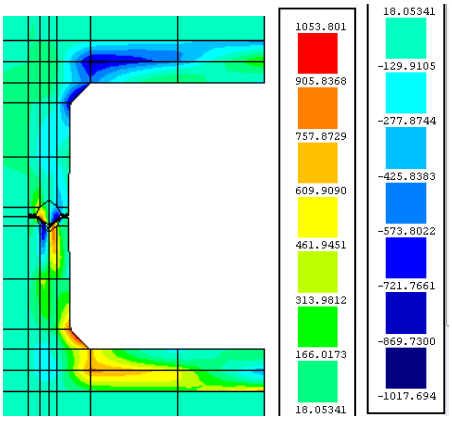

Fig. 49 – τ_{yz} field in the box-culvert (kPa).

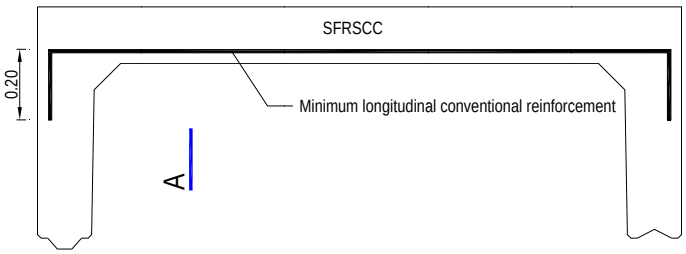

Fig. 50 – Proposed reinforcement.

5.2 IV-200-8 box-culvert

In the analysis of the IV-200-8 box culver, the values of the properties for the SFRSCC are indicated in Table 11, while for the soil and soil-concrete interface are included in Tables 17 and 16, respectively. For the soil, the Drucker-Prager criterion passing in the outer corners of the M-C yield surface, with softening law for the cohesion and friction angle evolution was used. Due to the relatively larger depth of the embankment soil layer (H_{st}, Fig. 2) in case of IV-200-8 box-culvert, better properties for the soil were considerer in the analysis of this box-culvert.

Table 17 – Values of the properties for the Drucker-Prager soil constitutive model.

E_s (MPa)	ν_s (-)	γ_s (kN/m^3)	c_o (kPa)	k_c (-)	ϕ_o ($^\circ$)	ϕ_f ($^\circ$)	K_f (-)
80.0	0.3	18.0	10.0	0.1	40.0	30.0	0.01

In a first analysis, using only fibres as the reinforcement for the box-culver, it was concluded that the developed SFRSCC is not capable of limiting the maximum crack width to a value required for this type of structures (0.3 mm), even for a relatively low live-load. A significantly higher content of fibres would be necessary, which, under the economic point-of-view can compromise the option of steel fibres in detriment of conventional steel bars. In this case, placing a certain percentage of conventional reinforcement in critical sections and maintaining 45 kg/m^3 of steel fibres seem to be a good compromise in terms of execution practice and economic point-of-views. Therefore, the conventional steel bars represented in Figure 51, was also added to the SFRSCC.

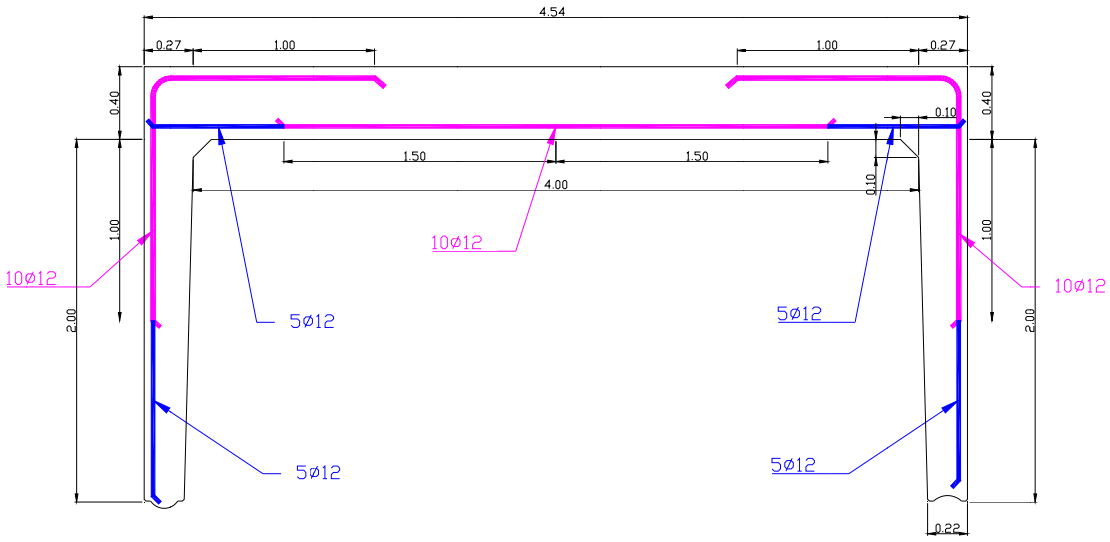

Fig. 51 – Arrangement of the conventional reinforcement applied in the SFRSCC IV-200-8 box-culvert.

Due to their relevance, only the results corresponding to the occurrence of a maximum crack width of 0.3mm are presented (the state at about the crack width limit for the serviceability design requirement for this type of structures). This crack width was estimated multiplying the maximum normal crack strain by the corresponding crack band width (square

root of the area of the corresponding finite element). This crack width occurred for a live load (LL, see Fig. 2) of 30 kPa.
Fig. 52 represents the displacement fields, while Fig. 53 shows the undeformed and the deformed meshes (for an amplifier factor of the displacements of 11).

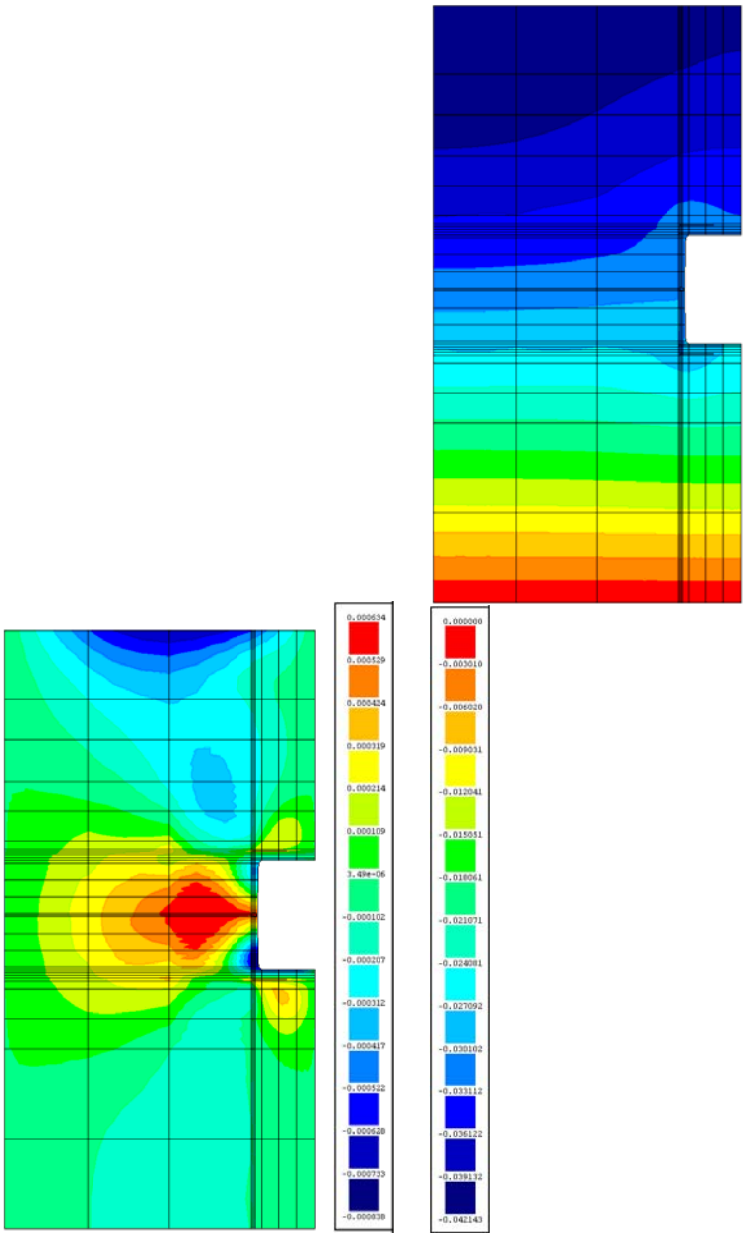

(a) (b)

Fig. 52 – Displacement field in *y* (a) and *z* (b) direction (m)

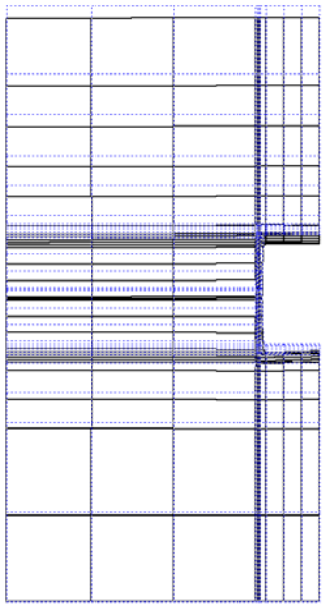

Fig. 53 – Deformed mesh.

The crack pattern is illustrated in Fig. 54 showing that flexural cracks are formed on the top and bottom slabs of the two components forming the box-culvert, as well as on the exterior parts at the top zones of the vertical walls. These last cracks were not formed in the m-505-5 box-culvert because the flexural resistance (for negative bending moments) of the wall and slab cross sections at the wall/slab joint connexion was similar, while in IV-200-8 the flexural resistance of the walls is significantly lower than the flexural resistance of the slab.

Therefore, an optimization of the geometry of the IV-200-8 box culvert seems to be opportune in order to optimize the global costs of this element. Some cracks also formed at the join connexion between the two elements that form the box-culvert, which recommends the use of an elastomer material able of decreasing the friction between the contacting materials in this zone (in the present study the same values for the constitutive law of the interface element were used for both soil-concrete and concrete-concrete, which was a simplified approach adopted, since no reliable data are still available to simulate accurately the concrete-concrete interface).

As Fig. 55 reveals, in the bottom element of the box culvert, in the zone of concrete in contact with the soil, at the symmetry axis of the problem, the σ_y compression stresses attained a maximum value of about 23 MPa, which is lower than the design value of the compressive strength of the SFRSCC considered for this box-culvert (f_{cm}=45 MPa). However, in the interior of the wall at the wall-slab joint of the bottom element of this box-culvert the σ_z compression stress is almost the design value of the SFRSCC compressive strength, which also recommends increasing the thickness of the walls of the box elements in the zone near the wall-slab connexion if the values of properties of the soil and the live load are those used in the present study.

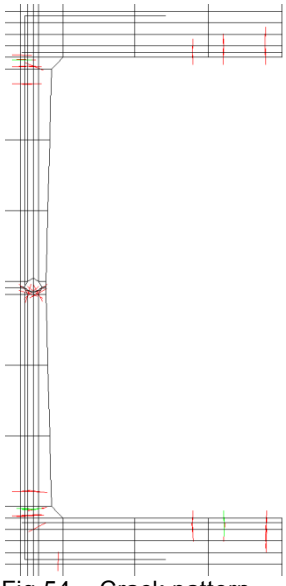

Fig 54 – Crack pattern.

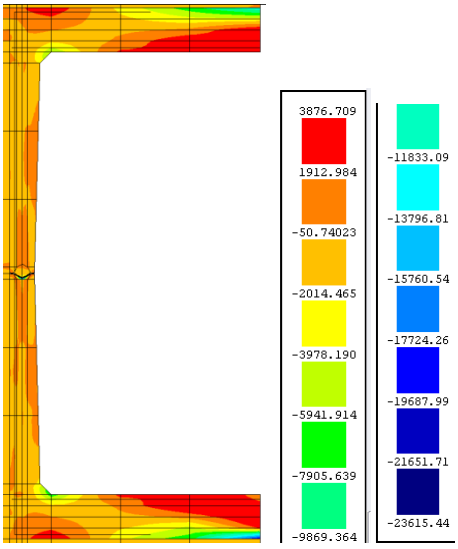

Fig. 55 – σ_y field in the box-culvert (kPa).

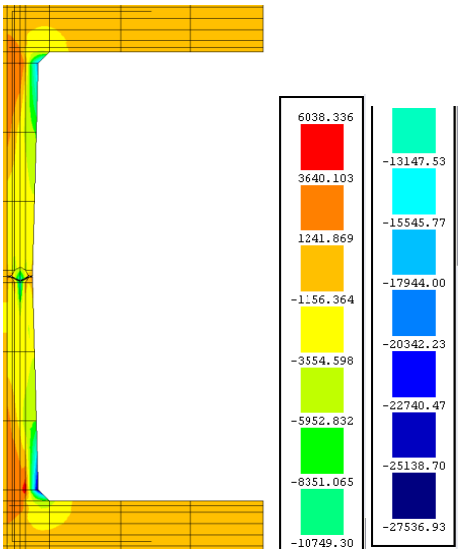

Fig. 56 – σ_z field in the box-culvert (kPa).

The shear stress field in the box-culvert is represented in Fig. 57. The maximum average shear stress occurs in the bottom slab at the section just aside the slab-wall connexion, with a value of 319 kPa, which is lower than the design value of the shear resistance, $V_{Rd,c}$, calculated according to EC2 (369 kPa). Therefore, the shear resistance seems do not be the critical shear failure mode of this type of structure.

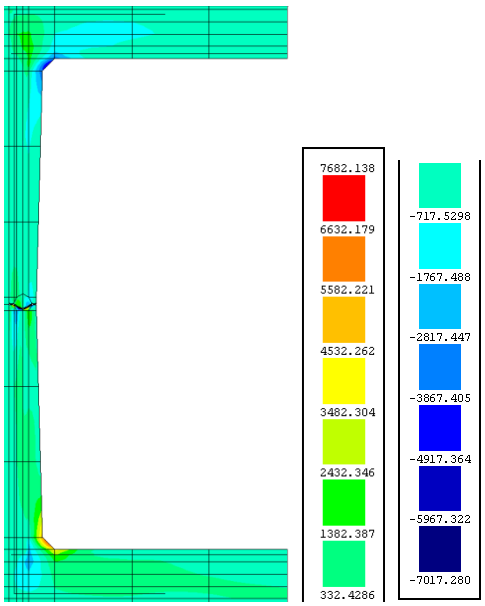

Fig. 57 – τ_{yz} field in the box-culvert (kPa).

6 CONCLUSIONS

In this paper a numerical model was briefly described to explore the possibilities of using fibre reinforced concrete for the partial or total replacement of conventional reinforcement in box-culvert underground structures. This is the first part of this research project, therefore some simplifications were adopted mainly for modelling the soil behaviour. In fact, the soil was model by an associated flow rule, elasto-plasticity Mohr-Coulomb yield criterion without any type of hardening. The box-culvert was simulated by a smeared 2D crack model and an interface model based on the Mohr-Coulomb principles and able of simulating a null tensile stress transfer between soil and concrete was developed. The simulation of phase construction process and the new constitutive laws were implemented into FEMIX computer program. A small and very stiff box-culvert was used in the present study, having been concluded that the 118.5 kg/m^3 of reinforcement currently used in this type of box-culvert can be reduced to 5.1 kg/m^3 if the steel fibre reinforced self compacting concrete, already developed within the ambit of another research project, is used. To improve the numerical model, the next research steps are composed by the introduction of a hardening/softening law for the cohesion and friction angle of the soil, the implementation of a non-associated flow rule elasto-plasticity approach in order to better simulate the inelastic soil volume changes, a constitutive law for the mode I component of the interface, able of simulating the use of appropriate materials at the soil-box-culvert interface in order to promote an oriented stress redistribution and, therefore, minimize the principal tensile stresses in the box-culvert.

7 ACKNOWLEDGEMENTS

The Author wishes to acknowledge the support provided by FCT, by means of the SFRH/BSAB/818/2008 and SFRH/BSAB/913/2009 sabbatical grants.

8 REFERENCES

Barragán, B.E., "Failure and tougness of steel fiber reinforced concrete under tension and shear", PhD Thesis, UPC, Barcelona, March 2002.

Barros et al., "PABERPRO - Conception and implementation of a system for the production of lightweight panels of steel fibre reinforced self-compacting concrete", Final report of PABERPRO project, University of Minho, September 2008

Barros, J.A.O., "Steel fiber reinforced self-compacting concrete – from the material characterization to the structural analysis", HAC2008, 1st Spanish Congress on Self-Compacting Concrete, Valencia, Spain, 31-58, 18-19 February 2008. (Invited Keynote Lecturer)

Barros, J. A. O., Pereira, E. B. and Santos, S. P. F., "Lightweight panels of steel fiber reinforced self-compacting concrete", *Journal of Materials in Civil Engineering*, 19(4), 295-304, 2007.

Barros, J.A.O.; Gettu, R.; Barragan, B.E., "Material Nonlinear analysis of Steel fibre reinforced concrete beams failing in shear", 6th International RILEM Symposium on fibre reinforced concrete - BEFIB 2004, Edts. M. di Prisco, R. Felicetti, G.A. Plizarri, Vol. 1, p. 711-720, 20-22 September 2004.

Barros, J.A.O., "Behaviour of fibre reinforced concrete - experimental and numerical analysis", PhD Thesis, Civil Eng. Dept., FEUP, Portugal, 1995. (in Portuguese)

De Borst, R. and Sluys, L.J., "Computational methods in non-linear solid mechanics", Koiter institute Delft, Delft University of Technology, CT5142, 2007.

Brite-Euram. Rational Production and Improved Working Environment through using Self Compacting Concrete - Brite-Euram project BRPR-CT96-0366. Technical report, Brite Euram / Swedish Cement and Concrete Research Institute, 2002.

Casanova, P.; Rossi, P.; Schaller. I., "Can steel fibres replace transverse reinforcement in reinforced concrete beams?", *ACI Material Journal*, 94, 341-354, 2000.

Casanova, P., "Bétons de fibres métalliques: du materiaux à la structure", PhD Thesis, École Nationale des Ponts et Chaussées, 1995. (in French)

CEB-FIP Model Code, Comite Euro-International du Beton, Bulletin d'Information nº 213/214, 1993.

Chen, W.F.; Han, D.J., "Plasticity for Structural Engineers", Springer-Verlag, 1988.

Chiaia, B.; Fantilli, A. P.; Vallini, P., "Evaluation of crack width in FRC structures and application to tunnel linnigs, Materials and Structures Journal, 43(3), 339-351, April 2009.

EN197-1:2000, "Cement. Composition, specifications and conformity criteria for low heat common cements." ISBN: 058036456 9, 52pp, 2000.

EFNARC, "Specification and Guidelines for Self-Compacting Concrete", ISBN 0 9539733 4 4, 32 pp, 2002.

Eurocode 2: *Design of concrete structures - Part 1-1: General rules and rules for buildings*. Comité Européen de Normalisation (CEN), EN 1992-1-1:2004: E, Brussels, 2004.

Gettu, R.; Barragán, B.; García, T.; Ramos, G; Fernández, C.; Oliver, R., "Steel Fiber Reinforced Concrete for the Barcelona Metro Line 9 Tunnel Lining", *6th RILEM Symposium on Fibre-Reinforced Concretes (FRC) – BEFIB*, 20-22 September, Varenna, Italy, 2004. (Invited lecturer)

Hofstetter, F.; Mang, H.A., "Computational mechanics of reinforced concrete structures", Vieweg, 1995.

Meda, A.; Minelli, F.; Plizzari, G. A.; Riva, P. "Shear behaviour of steel fibre reinforced concrete beams", *Materials and Structures Journal 38(3)*, 343-353, April 2005.

Okamura, H., "Ferguson Lecture for 1996: Self-compacting high-performance concrete", Concrete International, ACI 19(7), 50-4, 1997.

Pereira, E.B.; Barros, J.A.O., Camões, A.F.F.L., "Steel fiber reinforced self-compacting concrete – experimental research and numerical simulation", Journal of Structural Engineering, 134(8), 1310-1321, August 2008.

Pereira, E. N. B. *Steel Fibre Reinforced Self-compacting Concrete: from material to mechanical behaviour*, dissertation for Pedagogical and Scientific Aptitude Proofs, Department Civil Engineering, University of Minho, 188 pp, 2006. (http://www.civil.uminho.pt/composites)

RILEM TC 162-TDF, "Test and design methods for steel fibre reinforced concrete - σ - ε design method - Final Recommendation", Materials and Structures, 36, 560-567, October 2003.

Rots, J.G., "Computational modeling of concrete fracture", Dissertation, Delft University of Technology, 1988.

Sena-Cruz, J.M.; Barros, J.A.O.; Azevedo, A.F.M.; Ventura Gouveia, A.V. "Numerical simulation of the nonlinear behavior of RC beams strengthened with NSM CFRP strips", CMNE 2007 - Congress on Numerical Methods in Engineering and XXVIII CILAMCE - Iberian Latin American Congress on Computational Methods in Engineering, Abstract pp. 289, Paper nº 485 published in CD – FEUP, 20 pp., Porto, 13-15 June 2007.

Sena-Cruz, J.M.; Barros, J.A.O.; Ribeiro, A.F.; Azevedo, A.F.M.; Camões, A.F.F.L., "Stress-crack opening relationship of enhanced performance concrete", 9th Portuguese Conference on Fracture, ESTSetúbal, Portugal, p. 395-403, 18-20 February 2004.

Sena-Cruz, J.M. "Strengthening of concrete structures with near-surface mounted CFRP laminate strips." *PhD Thesis*, Department of Civil Engineering, University of Minho, 2004.

Swamy, R.N. and Al-Ta'An, S.A., "Deformation and Ultimate Strength in Flexure of Reinforced Concrete Beams made with Steel Fibre Concrete", ACI Journal, Proceedings 78(5), Sept-Oct., 395-405, 1981.

Vandewalle, L.; "Cracking behaviour of concrete beams reinforced with a combination of ordinary reinforcement and steel fibers", Materials and Structures Journal, 33(3), 339-351, April 2000

ANNEX

A.1 The return-mapping algorithm

The formulation is developed in the assumption a hardening/softening parameter, *k*, can be used to simulate the evolution of the cohesion and frictional angle of the material with the plastic variation, i.e., *c(k)* and *ϕ(k)*. Therefore, a non-hardening/softening material is a particular case of the present approach, i.e, when cohesion and friction angle are assumed having constant values regardless the damage installed into the material.

The return-mapping algorithm (n+1) is considered a new "load step" under the framework of FEM-based material nonlinear analysis using the implicit backward Euler algorithm):

$$\Delta\underline{\sigma}_{n+1} = \underline{D}\left(\Delta\underline{\varepsilon}_{n+1} - \Delta\underline{\varepsilon}^{p}_{n+1}\right) \tag{A.1}$$

being $\Delta\underline{\sigma}_{n+1}$, the stress increment vector, $\Delta\underline{\varepsilon}_{n+1}$ the total strain increment vector and $\Delta\underline{\varepsilon}^{p}_{n+1}$ plastic strain increment vector (all of them of four components). In (A.1) $\underline{D}$ represents the constitutive matrix for a plane strain problem,

$$\underline{D} = \begin{bmatrix} \frac{E(1-\upsilon)}{(1+\upsilon)(1-2\upsilon)} & \frac{\upsilon E}{(1+\upsilon)(1-2\upsilon)} & \frac{\upsilon E}{(1+\upsilon)(1-2\upsilon)} & 0 \\ \frac{\upsilon E}{(1+\upsilon)(1-2\upsilon)} & \frac{E(1-\upsilon)}{(1+\upsilon)(1-2\upsilon)} & \frac{\upsilon E}{(1+\upsilon)(1-2\upsilon)} & 0 \\ \frac{\upsilon E}{(1+\upsilon)(1-2\upsilon)} & \frac{\upsilon E}{(1+\upsilon)(1-2\upsilon)} & \frac{E(1-\upsilon)}{(1+\upsilon)(1-2\upsilon)} & 0 \\ 0 & 0 & 0 & \frac{E}{2(1+\upsilon)} \end{bmatrix} \tag{A.2}$$

where E and υ are the modulus of elasticity and Poisson coefficient of the soil.

$$\Delta\underline{\sigma}^{trial}_{n+1} = \underline{D}\left(\Delta\underline{\varepsilon}_{n+1} - \Delta\underline{\varepsilon}^{p,trial}_{n+1}\right) \tag{A.3}$$

being $\Delta\underline{\sigma}^{trial}_{n+1}$ the trial stress increment assuming the total strain increment as elastic, and

$$\underline{\varepsilon}^{p,trial}_{n+1} = \underline{\varepsilon}^{p}_{n} \tag{A.4}$$

The hardening/softening parameter (herein it will be designated by internal variable), *k*, is also assumed to preserve the value of the former load step at the onset of the new "load step",

$$k^{trial}_{n+1} = k_n \tag{A.5}$$

Following these assumptions the initial value of the yielding function is computed for the trial values of the "load step" n+1:

$$f^{trial}_{n+1} = f^{trial}_{n+1}\left(\underline{\sigma}^{trial}_{n+1},\ k^{trial}_{n+1}\right) \tag{A.6}$$

Then, the two ranges of possible solutions determine the behaviour of the material:

$$\begin{cases} \text{if } f^{trial}_{n+1} < 0 \text{ then } k^{trial}_{n+1} = k^{trial}_{n+1} \ (\text{elastic behaviour}) \\ \text{if } f^{trial}_{n+1} \geq 0 \text{ then } k^{trial}_{n+1} \neq k^{trial}_{n+1} \ (\text{elastic plastic behaviour}) \end{cases} \tag{A.7}$$

The new values of the total plastic strains and the internal variable are computed as follows:

$$\begin{cases} \underline{\varepsilon}^{p}_{n+1} = \underline{\varepsilon}^{p}_{n+1} + \Delta\underline{\varepsilon}^{p}_{n+1} \text{ with } \Delta\underline{\varepsilon}^{p}_{n+1} = \Delta\lambda_{n+1} \dfrac{\partial f_{n+1}}{\partial \underline{\sigma}_{n+1}} \\ k_{n+1} = k_n + \Delta k_{n+1} \text{ with } \Delta k_{n+1} = -\Delta\lambda_{n+1} \dfrac{\partial f_{n+1}}{\partial k_{n+1}} \end{cases} \tag{A.8}$$

Once the values of $\Delta\underline{\varepsilon}^{p}_{n+1}$ are calculated, the final state of stress $\Delta\underline{\sigma}_{n+1}$ are computed as follow:

$$\underline{\sigma}_{n+1} = \underline{\sigma}^{trial}_{n+1} - \underline{D}\,\Delta\underline{\varepsilon}^{p}_{n+1} = \underline{\sigma}^{trial}_{n+1} - \Delta\lambda_{n+1}\,\underline{D}\,\frac{\partial f_{n+1}}{\partial \underline{\sigma}_{n+1}} \tag{A.9}$$

The use of the backward Euler integration scheme in a numerical framework implies the need to determined the $\Delta\underline{\varepsilon}^{p}_{n+1}$ and Δk_{n+1} by an iterative procedure, where the objective is to minimize the residues $r^{l}_{f,n+1}$, $\underline{r}^{l}_{\varepsilon,n+1}$ and $r^{l}_{k,n+1}$:

$$r^{l}_{f,n+1} = f^{l}_{n+1}\left(\underline{\sigma}^{l}_{n+1}, k^{l}_{n+1}\right) \tag{A.10a}$$

$$\underline{r}^{l}_{\varepsilon,n+1} = -\underline{\varepsilon}^{p,l}_{n+1} + \underline{\varepsilon}^{p}_{n} + \Delta\lambda^{l}_{n+1}\,\frac{\partial f^{l}_{n+1}}{\partial \underline{\sigma}^{l}_{n+1}} \tag{A.10b}$$

$$r^{l}_{k,n+1} = -k^{l}_{n+1} + k_n - \Delta\lambda^{l}_{n+1}\,\frac{\partial f^{l}_{n+1}}{\partial k^{l}_{n+1}} \tag{A.10c}$$

In each of the three equation presented in Eq.(A.10), the *l* variable represents the iteration step within the iterative process destined to find the solutions of the $\Delta\underline{\sigma}_{n+1}$, the $\Delta\underline{\varepsilon}^{p}_{n+1}$ and the Δk_{n+1} variables. For the first step of the iterative procedure, (*l*=1), the residues $\underline{r}^{l=1}_{\varepsilon,n+1}$ and $r^{l=1}_{k,n+1}$ are null, and the residue $r^{l=1}_{f,n+1}$ is obtained from:

$$r^{l=1}_{k,n+1} = f^{l=1}_{n+1}\left(\underline{\sigma}^{trial}_{n+1},\ k_n\right) \tag{A.11}$$

The use of the Newton-Raphson scheme for the solution of the three equations system requires the linearization of the equations. By differentiating (A.10) yields,

$$r^{l}_{f,n+1} + \frac{\partial f^{l}_{n+1}}{\partial \underline{\sigma}^{l}_{n+1}}\,d\underline{\sigma}^{l}_{n+1} + \frac{\partial f^{l}_{n+1}}{\partial k^{l}_{n+1}}\,dk^{l}_{n+1} = 0 \tag{A.12a}$$

$$\underline{r}^{l}_{\varepsilon,n+1} - d\underline{\varepsilon}^{p,l}_{n+1} + d\lambda^{l}_{n+1}\,\frac{\partial f^{l}_{n+1}}{\partial \underline{\sigma}^{l}_{n+1}} + \Delta\lambda^{l}_{n+1}\left[\frac{\partial^2 f^{l}_{n+1}}{\partial\left(\underline{\sigma}^{l}_{n+1}\right)^2}\,d\underline{\sigma}^{l}_{n+1} + \frac{\partial^2 f^{l}_{n+1}}{\partial \underline{\sigma}^{l}_{n+1}\partial k^{l}_{n+1}}\,dk^{l}_{n+1}\right] = \underline{0} \tag{A.12b}$$

$$r^{l}_{k,n+1} - dk^{l}_{n+1} - d\lambda^{l}_{n+1}\,\frac{\partial f^{l}_{n+1}}{\partial k^{l}_{n+1}} - \Delta\lambda^{l}_{n+1}\left[\frac{\partial^2 f^{l}_{n+1}}{\partial\left(k^{l}_{n+1}\right)^2}\,dk^{l}_{n+1} + \frac{\partial^2 f^{l}_{n+1}}{\partial k^{l}_{n+1}\partial \underline{\sigma}^{l}_{n+1}}\,d\underline{\sigma}^{l}_{n+1}\right] = 0 \tag{A.12c}$$

or in a matrix format:

$$\underline{J}_{n+1}^{l}\begin{bmatrix} d\underline{\sigma}_{n+1}^{l} \\ dk_{n+1}^{l} \\ d\lambda_{n+1}^{l} \end{bmatrix} = -\begin{bmatrix} r_{f,n+1}^{l} \\ \underline{r}_{\varepsilon,n+1}^{l} \\ r_{k,n+1}^{l} \end{bmatrix} \tag{A.13}$$

being $\underline{J}_{n+1}^{l}$ the Jacobian:

$$\underline{J}_{n+1}^{l} = \begin{bmatrix} \dfrac{\partial F_1}{\partial \underline{\sigma}_{n+1}} & \dfrac{\partial F_1}{\partial k_{n+1}} & \dfrac{\partial F_1}{\partial \lambda_{n+1}} \\ \dfrac{\partial F_2}{\partial \underline{\sigma}_{n+1}} & \dfrac{\partial F_2}{\partial k_{n+1}} & \dfrac{\partial F_2}{\partial \lambda_{n+1}} \\ \dfrac{\partial F_3}{\partial \underline{\sigma}_{n+1}} & \dfrac{\partial F_3}{\partial k_{n+1}} & \dfrac{\partial F_3}{\partial \lambda_{n+1}} \end{bmatrix}^{l} \tag{A.14}$$

where

$$F_1^l = f_{n+1}^l\left(\underline{\sigma}_{n+1}^l,\ k_{n+1}^l\right) \tag{A.15a}$$

$$F_2^l = \underline{D}^{-1}\Delta\underline{\sigma}_{n+1}^l + \Delta\lambda_{n+1}^l\ \frac{\partial f_{n+1}^l}{\partial \underline{\sigma}_{n+1}^l} \tag{A.15b}$$

$$F_3^l = -\Delta k_{n+1}^l - \Delta\lambda_{n+1}^l\ \frac{\partial f_{n+1}^l}{\partial k_{n+1}^l} \tag{A.15c}$$

Since

$$\underline{\varepsilon}_n^p = \underline{\varepsilon}_{n+1}^p + \Delta\underline{\varepsilon}_{n+1}^p \tag{A.16}$$

and

$$\Delta\underline{\sigma}_{n+1} = \underline{D}\left(\Delta\underline{\varepsilon}_{n+1} - \Delta\underline{\varepsilon}_{n+1}^p\right) \tag{A.17}$$

and since the updates on the integration point level are carried out for known $\Delta\underline{\varepsilon}_{n+1}$, the replacement of the term "$-\underline{\varepsilon}_{n+1}^{p,l} + \underline{\varepsilon}_n^p$" of Eq. (A.10b) by "$\underline{D}^{-1}\Delta\underline{\sigma}_{n+1}^l$" in Eq. (A.15b) is the result of the linearization of (A.17). In Eq. (A.10c) the term "$-k_{n+1}^l + k_n$" was replaced by "$-\Delta k_{n+1}^l$", which justifies the present of this term in Eq. (A.15c).

The terms of the $\underline{J}_{n+1}^{l}$ have the following configuration:

$$\frac{\partial F_1}{\partial \underline{\sigma}_{n+1}} = \frac{\partial f_{n+1}^l}{\partial \underline{\sigma}_{n+1}^l}\, d\underline{\sigma}_{n+1}^l \tag{A.18a}$$

$$\frac{\partial F_1}{\partial k_{n+1}} = \frac{\partial f_{n+1}^l}{\partial k_{n+1}^l}\, dk_{n+1}^l \tag{A.18b}$$

$$\frac{\partial F_1}{\partial \lambda_{n+1}} = 0 \tag{A.18c}$$

$$\frac{\partial F_2}{\partial \underline{\sigma}_{n+1}} = \left(\underline{D}^{-1} + \Delta\lambda_{n+1}^{l} \frac{\partial^2 f_{n+1}^{l}}{\partial \left(\underline{\sigma}_{n+1}^{l} \right)^2} \right) d\underline{\sigma}_{n+1}^{l} \tag{A.18d}$$

$$\frac{\partial F_2}{\partial k_{n+1}} = \Delta\lambda_{n+1}^{l} \frac{\partial^2 f_{n+1}^{l}}{\partial \underline{\sigma}_{n+1}^{l} \partial k_{n+1}^{l}} dk_{n+1}^{l} \tag{A.18e}$$

$$\frac{\partial F_2}{\partial \lambda_{n+1}} = \frac{\partial f_{n+1}^{l}}{\partial \underline{\sigma}_{n+1}^{l}} d\lambda_{n+1}^{l} \tag{A.18f}$$

$$\frac{\partial F_3}{\partial \underline{\sigma}_{n+1}} = -\Delta\lambda_{n+1}^{l} \frac{\partial^2 f_{n+1}^{l}}{\partial k_{n+1}^{l} \partial \underline{\sigma}_{n+1}^{l}} d\underline{\sigma}_{n+1}^{l} \tag{A.18g}$$

$$\frac{\partial F_3}{\partial k_{n+1}} = \left(-1 - \Delta\lambda_{n+1}^{l} \frac{\partial^2 f_{n+1}^{l}}{\partial \left(k_{n+1}^{l} \right)^2} \right) dk_{n+1}^{l} \tag{A.18h}$$

$$\frac{\partial F_3}{\partial \lambda_{n+1}} = -\frac{\partial f_{n+1}^{l}}{\partial k_{n+1}^{l}} d\lambda_{n+1}^{l} \tag{A.18i}$$

The final converged values of the unknowns for the step “n+1” are obtained trough the successive summation of the increments determined at each iteration from the linear system of Eqs. (A.13):

$$\underline{\sigma}_{n+1}^{l} = \underline{\sigma}_{n} + \sum_{i=1}^{l} d\underline{\sigma}_{n+1}^{i} \tag{A.19a}$$

$$k_{n+1}^{l} = k_{n} + \sum_{i=1}^{l} dk_{n+1}^{i} \tag{A.19b}$$

$$\Delta\lambda_{n+1}^{l} = \sum_{i=1}^{l} d\lambda_{n+1}^{i} \tag{A.19c}$$

A.2 The consistent tangent elasto-plastic constitutive matrix

For the integration of the FEM equilibrium equations within the Newton-Raphson incremental-iterative algorithm framework, the use of the consistent tangent constitutive matrix is desirable since it contributes to a faster convergence of this algorithm. The obtaining of the consistent tangent constitutive matrix is described in the following steps.

Yield function:

$$f_{n+1} = f_{n+1}\left(\underline{\sigma}_{n+1},\ k_{n+1} \right) \tag{A.20}$$

Constitutive equation:

$$\Delta\underline{\sigma}_{n+1} = \underline{D}\left(\Delta\underline{\varepsilon}_{n+1} - \Delta\underline{\varepsilon}_{n+1}^{p} \right) \tag{A.21}$$

Associated flow rule:

$$\Delta \underline{\varepsilon}^{p}_{n+1} = \Delta\lambda_{n+1} \frac{\partial f_{n+1}}{\partial \underline{\sigma}_{n+1}} \tag{A.22}$$

Evolution law:

$$\Delta k_{n+1} = -\Delta\lambda_{n+1} \frac{\partial f_{n+1}}{\partial k_{n+1}} \tag{A.23}$$

The derivation of the consistent tangent matrix for the general return-mapping algorithm requires the determination of the total differentials df_{n+1}, $d\underline{\sigma}_{n+1}$, $d\underline{\varepsilon}^{p}_{n+1}$ dk_{n+1}. For the yield function (normality rule):

$$df_{n+1} = \frac{\partial f_{n+1}}{\partial \underline{\sigma}_{n+1}} d\underline{\sigma}_{n+1} + \frac{\partial f_{n+1}}{\partial k_{n+1}} dk_{n+1} \tag{A.24}$$

for the constitutive equation:

$$d\underline{\sigma}_{n+1} = \underline{D}\left(d\underline{\varepsilon}_{n+1} - d\underline{\varepsilon}^{p}_{n+1} \right) \tag{A.25}$$

for the flow rule:

$$d\underline{\varepsilon}^{p}_{n+1} = d\lambda_{n+1} \frac{\partial f_{n+1}}{\partial \underline{\sigma}_{n+1}} + \Delta\lambda_{n+1} \left[\frac{\partial^2 f_{n+1}}{\partial \underline{\sigma}^2_{n+1}} d\underline{\sigma}_{n+1} + \frac{\partial^2 f_{n+1}}{\partial \underline{\sigma}_{n+1} \partial k_{n+1}} dk_{n+1} \right] \tag{A.26}$$

and for the evolution law:

$$dk_{n+1} = -d\lambda_{n+1} \frac{\partial f_{n+1}}{\partial k_{n+1}} - \Delta\lambda_{n+1} \left[\frac{\partial^2 f_{n+1}}{\partial k^2_{n+1}} dk_{n+1} + \frac{\partial^2 f_{n+1}}{\partial k_{n+1} \partial \underline{\sigma}_{n+1}} d\underline{\sigma}_{n+1} \right] \tag{A.27}$$

Substituting (A.26) in (A.25) and after some algebraic operations:

$$d\underline{\sigma}_{n+1} = \underline{H} \left(d\underline{\varepsilon}_{n+1} - d\lambda_{n+1} \frac{\partial f_{n+1}}{\partial \underline{\sigma}_{n+1}} - \Delta\lambda_{n+1} \frac{\partial^2 f_{n+1}}{\partial \underline{\sigma}_{n+1} \partial k_{n+1}} dk_{n+1} \right) \tag{A.28}$$

being:

$$\underline{H} = \left(\underline{D}^{-1} + \Delta\lambda_{n+1} \frac{\partial^2 f_{n+1}}{\partial \underline{\sigma}^2_{n+1}} \right)^{-1} \tag{A.29}$$

Substituting (A.28) into (A.24) and assuming $df_{n+1} = 0$ while plastic deformation is taking place:

$$\frac{\partial f_{n+1}}{\partial \underline{\sigma}_{n+1}} \underline{H} d\underline{\varepsilon}_{n+1} = d\lambda_{n+1} \frac{\partial f_{n+1}}{\partial \underline{\sigma}_{n+1}} \underline{H} \frac{\partial f_{n+1}}{\partial \underline{\sigma}_{n+1}} + \left(\Delta\lambda_{n+1} \frac{\partial f_{n+1}}{\partial \underline{\sigma}_{n+1}} \underline{H} \frac{\partial^2 f_{n+1}}{\partial \underline{\sigma}_{n+1} \partial k_{n+1}} - \frac{\partial f_{n+1}}{\partial k_{n+1}} \right) dk_{n+1} \tag{A.30}$$

Substituting (A.28) into (A.27):

$$\left(\Delta\lambda_{n+1}\frac{\partial^2 f_{n+1}}{\partial k_{n+1}\partial\underline{\sigma}_{n+1}}\underline{H}\frac{\partial f_{n+1}}{\partial\underline{\sigma}_{n+1}}-\frac{\partial f_{n+1}}{\partial k_{n+1}}\right)d\lambda_{n+1}+$$
$$\left(\Delta\lambda_{n+1}^2\frac{\partial^2 f_{n+1}}{\partial k_{n+1}\partial\underline{\sigma}_{n+1}}\underline{H}\frac{\partial^2 f_{n+1}}{\partial\underline{\sigma}_{n+1}\partial k_{n+1}}-\Delta\lambda_{n+1}\frac{\partial^2 f_{n+1}}{\partial k_{n+1}^2}-1\right)dk_{n+1}= \tag{A.31}$$
$$\Delta\lambda_{n+1}\frac{\partial^2 f_{n+1}}{\partial k_{n+1}\partial\underline{\sigma}_{n+1}}\underline{H}d\underline{\varepsilon}_{n+1}$$

In order to be possible the substitution of Eq. (A.30) and Eq. (A.31) into Eq. (A.28), the first and the second must be described explicitly with respect to $d\lambda_{n+1}$ and $\Delta\lambda_{n+1}dk_{n+1}$. In this fashion Eq. (A.30) can be rewritten as:

$$\frac{\partial f_{n+1}}{\partial\underline{\sigma}_{n+1}}\underline{H}\frac{\partial f_{n+1}}{\partial\underline{\sigma}_{n+1}}d\lambda_{n+1}+\left(\frac{\partial f_{n+1}}{\partial\underline{\sigma}_{n+1}}\underline{H}\frac{\partial^2 f_{n+1}}{\partial\underline{\sigma}_{n+1}\partial k_{n+1}}-\frac{1}{\Delta\lambda_{n+1}}\frac{\partial f_{n+1}}{\partial k_{n+1}}\right)\Delta\lambda_{n+1}dk_{n+1}= \tag{A.32}$$
$$\frac{\partial f_{n+1}}{\partial\underline{\sigma}_{n+1}}\underline{H}d\underline{\varepsilon}_{n+1}$$

and for Eq. (A.31)

$$\left(\frac{\partial^2 f_{n+1}}{\partial k_{n+1}\partial\underline{\sigma}_{n+1}}\underline{H}\frac{\partial f_{n+1}}{\partial\underline{\sigma}_{n+1}}-\frac{1}{\Delta\lambda_{n+1}}\frac{\partial f_{n+1}}{\partial k_{n+1}}\right)d\lambda_{n+1}+$$
$$\left(\frac{\partial^2 f_{n+1}}{\partial k_{n+1}\partial\underline{\sigma}_{n+1}}\underline{H}\frac{\partial^2 f_{n+1}}{\partial\underline{\sigma}_{n+1}\partial k_{n+1}}-\frac{1}{\Delta\lambda_{n+1}}\frac{\partial^2 f_{n+1}}{\partial k_{n+1}^2}-\frac{1}{\Delta\lambda_{n+1}^2}\right)\Delta\lambda_{n+1}dk_{n+1}= \tag{A.33}$$
$$\frac{\partial^2 f_{n+1}}{\partial k_{n+1}\partial\underline{\sigma}_{n+1}}\underline{H}d\underline{\varepsilon}_{n+1}$$

The values of $d\lambda_{n+1}$ and $\Delta\lambda_{n+1}dk_{n+1}$ can be obtained by solving the system formed by Eq. (A.32) and Eq. (A.33):

$$\begin{bmatrix} d\lambda_{n+1} \\ \Delta\lambda_{n+1}dk_{n+1}\end{bmatrix}=\begin{bmatrix} A_{11} & A_{12} \\ A_{21} & A_{22}\end{bmatrix}^{-1}\begin{bmatrix} B_1 \\ B_2\end{bmatrix} \tag{A.34}$$

being:

$$A_{11}=\frac{\partial f_{n+1}}{\partial\underline{\sigma}_{n+1}}\underline{H}\frac{\partial f_{n+1}}{\partial\underline{\sigma}_{n+1}} \tag{A.35a}$$

$$A_{12}=\frac{\partial f_{n+1}}{\partial\underline{\sigma}_{n+1}}\underline{H}\frac{\partial^2 f_{n+1}}{\partial\underline{\sigma}_{n+1}\partial k_{n+1}}-\frac{1}{\Delta\lambda_{n+1}}\frac{\partial f_{n+1}}{\partial k_{n+1}} \tag{A.35b}$$

$$A_{21}=A_{12}=\frac{\partial^2 f_{n+1}}{\partial\underline{\sigma}_{n+1}\partial k_{n+1}}\underline{H}\frac{\partial f_{n+1}}{\partial\underline{\sigma}_{n+1}}-\frac{1}{\Delta\lambda_{n+1}}\frac{\partial f_{n+1}}{\partial k_{n+1}} \tag{A.35c}$$

$$A_{22}=\frac{\partial^2 f_{n+1}}{\partial k_{n+1}\partial\underline{\sigma}_{n+1}}\underline{H}\frac{\partial^2 f_{n+1}}{\partial\underline{\sigma}_{n+1}\partial k_{n+1}}-\frac{1}{\Delta\lambda_{n+1}}\frac{\partial^2 f_{n+1}}{\partial k_{n+1}^2}-\frac{1}{\Delta\lambda_{n+1}^2} \tag{A.35d}$$

$$B_1 = \frac{\partial f_{n+1}}{\partial \underline{\sigma}_{n+1}} \underline{H} d\underline{\varepsilon}_{n+1} \tag{A.35e}$$

$$B_2 = \frac{\partial^2 f_{n+1}}{\partial k_{n+1} \partial \underline{\sigma}_{n+1}} \underline{H} d\underline{\varepsilon}_{n+1} \tag{A.35f}$$

If it is assumed that:

$$\begin{bmatrix} A_{11} & A_{12} \\ A_{21} & A_{22} \end{bmatrix}^{-1} = \begin{bmatrix} a_{11} & a_{12} \\ a_{21} & a_{22} \end{bmatrix} \tag{A.36}$$

then:

$$a_{11} = \frac{A_{22}}{A_{11}A_{22} - A_{12}A_{22}} \tag{A.37a}$$

$$a_{12} = a_{21} = -\frac{A_{12}}{A_{11}A_{22} - A_{12}A_{22}} \tag{A.37b}$$

$$a_{22} = \frac{A_{11}}{A_{11}A_{22} - A_{12}A_{22}} \tag{A.37c}$$

The B1 and the B2 terms can be also rewritten in the following format:

$$\begin{bmatrix} B_1 \\ B_2 \end{bmatrix} = \begin{bmatrix} \underline{b}_1 \\ \underline{b}_2 \end{bmatrix} d\varepsilon_{n+1} \tag{A.38}$$

being:

$$\underline{b}_1 = \frac{\partial f_{n+1}}{\partial \underline{\sigma}_{n+1}} \underline{H} \tag{A.39a}$$

$$\underline{b}_2 = \frac{\partial^2 f_{n+1}}{\partial k_{n+1} \partial \underline{\sigma}_{n+1}} \underline{H} \tag{A.39b}$$

Therefore, from the first row of the Eq. (A.34):

$$d\lambda_{n+1} = \left(a_{11}\underline{b}_1 + a_{12}\underline{b}_2 \right) d\varepsilon_{n+1} \tag{A.40a}$$

and from the second row of the Eq. (A.34):

$$\Delta\lambda_{n+1} dk_{n+1} = \left(a_{21}\underline{b}_1 + a_{22}\underline{b}_2 \right) d\varepsilon_{n+1} \tag{A.40b}$$

Replacing Eq. (A.40) in Eq. (A.28) yields:

$$d\underline{\sigma}_{n+1} = \begin{pmatrix} \underline{H} - a_{11}\underline{H} \dfrac{\partial f_{n+1}}{\partial \underline{\sigma}_{n+1}} \dfrac{\partial f_{n+1}}{\partial \underline{\sigma}_{n+1}} \underline{H} - a_{12}\underline{H} \dfrac{\partial f_{n+1}}{\partial \underline{\sigma}_{n+1}} \dfrac{\partial^2 f_{n+1}}{\partial k_{n+1} \partial \underline{\sigma}_{n+1}} \underline{H} - \\ a_{21}\underline{H} \dfrac{\partial^2 f_{n+1}}{\partial \underline{\sigma}_{n+1} \partial k_{n+1}} \dfrac{\partial f_{n+1}}{\partial \underline{\sigma}_{n+1}} \underline{H} - a_{22}\underline{H} \dfrac{\partial^2 f_{n+1}}{\partial \underline{\sigma}_{n+1} \partial k_{n+1}} \dfrac{\partial^2 f_{n+1}}{\partial k_{n+1} \partial \underline{\sigma}_{n+1}} \underline{H} \end{pmatrix} d\underline{\varepsilon}_{n+1} \tag{A.41}$$

or, in a condensed format:

$$d\underline{\sigma}_{n+1} = \left(\underline{H} - \sum_{i=1}^{2}\sum_{i=1}^{2} a_{ij}\underline{c}_i\underline{c}_j \right) d\underline{\varepsilon}_{n+1} \tag{A.42}$$

being:

$$\underline{c}_1 = \underline{H}\frac{\partial f_{n+1}}{\partial \underline{\sigma}_{n+1}} \tag{A.43a}$$

$$\underline{c}_2 = \underline{H}\frac{\partial^2 f_{n+1}}{\partial k_{n+1}\partial \underline{\sigma}_{n+1}} \tag{A.43b}$$

So finally the consistent tangent constitutive matrix has the following format:

$$\underline{D}_{ep} = \underline{H} - \sum_{i=1}^{2}\sum_{i=1}^{2} a_{ij}\underline{c}_i\underline{c}_j \tag{A.44}$$

If no hardening/softening is considered for the cohesion and frictional angle of the material, i.e., both c and ϕ are considered constant, the second row and second column of the Jacobian at Eq. (A.14) are eliminated and the unknowns are $d\underline{\sigma}_{n+1}$ and $d\lambda_{n+1}$. In terms of the constituent tangent constitutive matrix it becomes reduced to the following format:

$$d\underline{\sigma}_{n+1} = \left(\underline{H} - \frac{\underline{H}\dfrac{\partial f_{n+1}}{\partial \underline{\sigma}_{n+1}}\dfrac{\partial f_{n+1}}{\partial \underline{\sigma}_{n+1}}\underline{H}}{\dfrac{\partial f_{n+1}}{\partial \underline{\sigma}_{n+1}}\underline{H}\dfrac{\partial f_{n+1}}{\partial \underline{\sigma}_{n+1}}} \right) d\underline{\varepsilon}_{n+1} \tag{A.45}$$

since

$$a_{11} = \frac{1}{\dfrac{\partial f_{n+1}}{\partial \underline{\sigma}_{n+1}}\underline{H}\dfrac{\partial f_{n+1}}{\partial \underline{\sigma}_{n+1}}} \tag{A.46}$$

and $a_{12}=a_{21}=a_{22}=0$.

A.3 The derivatives of the stress invariants for the plane strain problems

For a plane strain problem, the stress vector has the following four components (the structure is considered inscribed in the *yz* plane, so σ_x is the component orthogonal to the plane of the structure):

$$\underline{\sigma} = \begin{bmatrix} \sigma_x & \sigma_y & \sigma_z & \tau_{yz} \end{bmatrix}^T \tag{A.47}$$

The first, the second deviatoric and the third deviatoric stress invariants used in the yield functions treated in the present work are the following:

$$I_1 = \sigma_x + \sigma_y + \sigma_z \tag{A.48}$$

$$J_2 = \frac{1}{3}\left(\sigma_x^2 + \sigma_y^2 + \sigma_z^2 - \sigma_x\sigma_y - \sigma_x\sigma_z - \sigma_y\sigma_z + 3\tau_{yz}^2 \right) \tag{A.49}$$

$$J_3 = \frac{2}{27}\left(\sigma_x^3 + \sigma_y^3 + \sigma_z^3\right) - \frac{1}{9}\left(\sigma_x^2\sigma_y + \sigma_x^2\sigma_z + \sigma_y^2\sigma_x + \sigma_y^2\sigma_z + \sigma_z^2\sigma_x + \sigma_z^2\sigma_y\right) + \frac{4}{9}\sigma_x\sigma_y\sigma_z + \frac{1}{3}\tau_{yz}^2\left(\sigma_y + \sigma_z - 2\sigma_x\right) \quad \text{(A.50)}$$

The first order derivatives of the first, the second deviatoric and the third deviatoric stress invariants have the following format:

$$\frac{\partial I_1}{\partial \sigma_x} = \frac{\partial I_1}{\partial \sigma_y} = \frac{\partial I_1}{\partial \sigma_z} = 1;\ \frac{\partial I_1}{\partial \tau_{yz}} = 0 \quad \text{(A.51)}$$

$$\begin{aligned} \frac{\partial J_2}{\partial \sigma_x} &= \frac{1}{3}\left(2\sigma_x - \sigma_y - \sigma_z\right) \\ \frac{\partial J_2}{\partial \sigma_y} &= \frac{1}{3}\left(2\sigma_y - \sigma_x - \sigma_z\right) \\ \frac{\partial J_2}{\partial \sigma_z} &= \frac{1}{3}\left(2\sigma_z - \sigma_x - \sigma_y\right) \\ \frac{\partial J_2}{\partial \tau} &= 2\tau_{yz} \end{aligned} \quad \text{(A.52)}$$

$$\begin{aligned} \frac{\partial J_3}{\partial \sigma_x} &= \frac{1}{9}\left(2\sigma_x^2 - \sigma_y^2 - \sigma_z^2 - 2\sigma_x\sigma_y - 2\sigma_x\sigma_z + 4\sigma_y\sigma_z\right) - \frac{2}{3}\tau_{yz}^2 \\ \frac{\partial J_3}{\partial \sigma_y} &= \frac{1}{9}\left(2\sigma_y^2 - \sigma_x^2 - \sigma_z^2 - 2\sigma_x\sigma_y - 2\sigma_y\sigma_z + 4\sigma_x\sigma_z\right) + \frac{1}{3}\tau_{yz}^2 \\ \frac{\partial J_3}{\partial \sigma_z} &= \frac{1}{9}\left(2\sigma_z^2 - \sigma_x^2 - \sigma_y^2 - 2\sigma_x\sigma_z - 2\sigma_y\sigma_z + 4\sigma_x\sigma_y\right) + \frac{1}{3}\tau_{yz}^2 \\ \frac{\partial J_3}{\partial \tau_{yz}} &= \frac{2}{3}\tau_{yz}\left(\sigma_y + \sigma_z - 2\sigma_x\right) \end{aligned} \quad \text{(A.53)}$$

The second order derivatives of the first, the second deviatoric and the third deviatoric stress invariants have the following format:

$$\frac{\partial^2 I_1}{\partial \sigma_x^2} = \frac{\partial^2 I_1}{\partial \sigma_y^2} = \frac{\partial^2 I_1}{\partial \sigma_z^2} = \frac{\partial^2 I_1}{\partial \tau_{yz}^2} = 0 \quad \text{(A.54)}$$

$$\frac{\partial}{\partial\sigma_x}\left(\frac{\partial J_2}{\partial\sigma_x}\right)=\frac{2}{3};\quad \frac{\partial}{\partial\sigma_x}\left(\frac{\partial J_2}{\partial\sigma_y}\right)=-\frac{1}{3};\quad \frac{\partial}{\partial\sigma_x}\left(\frac{\partial J_2}{\partial\sigma_z}\right)=-\frac{1}{3};\quad \frac{\partial}{\partial\sigma_x}\left(\frac{\partial J_2}{\partial\tau_{yz}}\right)=0$$

$$\frac{\partial}{\partial\sigma_y}\left(\frac{\partial J_2}{\partial\sigma_x}\right)=-\frac{1}{3};\quad \frac{\partial}{\partial\sigma_y}\left(\frac{\partial J_2}{\partial\sigma_y}\right)=\frac{2}{3};\quad \frac{\partial}{\partial\sigma_y}\left(\frac{\partial J_2}{\partial\sigma_z}\right)=-\frac{1}{3};\quad \frac{\partial}{\partial\sigma_y}\left(\frac{\partial J_2}{\partial\tau_{yz}}\right)=0$$

$$\frac{\partial}{\partial\sigma_z}\left(\frac{\partial J_2}{\partial\sigma_x}\right)=-\frac{1}{3};\quad \frac{\partial}{\partial\sigma_z}\left(\frac{\partial J_2}{\partial\sigma_y}\right)=-\frac{1}{3};\quad \frac{\partial}{\partial\sigma_z}\left(\frac{\partial J_2}{\partial\sigma_z}\right)=\frac{2}{3};\quad \frac{\partial}{\partial\sigma_z}\left(\frac{\partial J_2}{\partial\tau_{yz}}\right)=0 \qquad \text{(A.55)}$$

$$\frac{\partial}{\partial\tau_{yz}}\left(\frac{\partial J_2}{\partial\sigma_x}\right)=0;\qquad \frac{\partial}{\partial\tau_{yz}}\left(\frac{\partial J_2}{\partial\sigma_y}\right)=0;\qquad \frac{\partial}{\partial\tau_{yz}}\left(\frac{\partial J_2}{\partial\sigma_z}\right)=0;\quad \frac{\partial}{\partial\tau_{yz}}\left(\frac{\partial J_2}{\partial\tau_{yz}}\right)=2$$

$$\frac{\partial}{\partial\sigma_x}\left(\frac{\partial J_3}{\partial\sigma_x}\right)=\frac{2}{9}\left[2\sigma_x-\left(\sigma_y+\sigma_z\right)\right];\ \frac{\partial}{\partial\sigma_x}\left(\frac{\partial J_3}{\partial\sigma_y}\right)=\frac{2}{9}\left[2\sigma_z-\left(\sigma_x+\sigma_y\right)\right];\ \frac{\partial}{\partial\sigma_x}\left(\frac{\partial J_3}{\partial\sigma_z}\right)=\frac{2}{9}\left[2\sigma_y-\left(\sigma_x+\sigma_z\right)\right];\ \frac{\partial}{\partial\sigma_x}\left(\frac{\partial J_3}{\partial\tau_{yz}}\right)=-\frac{4}{3}\tau_{yz}$$

$$\frac{\partial}{\partial\sigma_y}\left(\frac{\partial J_3}{\partial\sigma_x}\right)=\frac{2}{9}\left[2\sigma_z-\left(\sigma_x+\sigma_y\right)\right];\ \frac{\partial}{\partial\sigma_y}\left(\frac{\partial J_3}{\partial\sigma_y}\right)=\frac{2}{9}\left[2\sigma_y-\left(\sigma_x+\sigma_z\right)\right];\ \frac{\partial}{\partial\sigma_y}\left(\frac{\partial J_3}{\partial\sigma_z}\right)=\frac{2}{9}\left[2\sigma_x-\left(\sigma_y+\sigma_z\right)\right];\ \frac{\partial}{\partial\sigma_y}\left(\frac{\partial J_3}{\partial\tau_{yz}}\right)=\frac{2}{3}\tau_{yz} \qquad \text{(A.56)}$$

$$\frac{\partial}{\partial\sigma_z}\left(\frac{\partial J_3}{\partial\sigma_x}\right)=\frac{2}{9}\left[2\sigma_y-\left(\sigma_x+\sigma_z\right)\right];\ \frac{\partial}{\partial\sigma_z}\left(\frac{\partial J_3}{\partial\sigma_y}\right)=\frac{2}{9}\left[2\sigma_x-\left(\sigma_y+\sigma_z\right)\right];\ \frac{\partial}{\partial\sigma_z}\left(\frac{\partial J_3}{\partial\sigma_z}\right)=\frac{2}{9}\left[2\sigma_z-\left(\sigma_x+\sigma_y\right)\right];\ \frac{\partial}{\partial\sigma_z}\left(\frac{\partial J_3}{\partial\tau_{yz}}\right)=\frac{2}{3}\tau_{yz}$$

$$\frac{\partial}{\partial\tau_{yz}}\left(\frac{\partial J_3}{\partial\sigma_x}\right)=-\frac{4}{3}\tau_{yz};\qquad \frac{\partial}{\partial\tau_{yz}}\left(\frac{\partial J_3}{\partial\sigma_y}\right)=\frac{2}{3}\tau_{yz};\qquad \frac{\partial}{\partial\tau_{yz}}\left(\frac{\partial J_3}{\partial\sigma_z}\right)=\frac{2}{3}\tau_{yz};\qquad \frac{\partial}{\partial\tau_{yz}}\left(\frac{\partial J_3}{\partial\tau_{yz}}\right)=\frac{2}{3}\left(\sigma_y+\sigma_z-2\sigma_x\right)$$

A.4 The first and the second order derivatives of the yield function of the Mohr-Coulomb criterion

The formulation is developed in the assumption a hardening/softening parameter, *k*, can be used to simulate the evolution of the cohesion and frictional angle of the material with the plastic variation, i.e., *c(k)* and $\phi(k)$.

$$f\left(\underline{\sigma},k\right)=\frac{1}{3}I_1\sin\phi\left(k\right)+J_2^{1/2}\left(\cos\theta-\frac{1}{\sqrt{3}}\sin\theta\sin\phi\left(k\right)\right)-c\left(k\right)\cos\phi\left(k\right) \qquad \text{(A.57)}$$

In this section the derivatives necessary for the implementation of the model are presented.

$$\frac{\partial f}{\partial k}=\frac{1}{3}I_1\cos\phi\left(k\right)\frac{\partial\phi\left(k\right)}{\partial k}-\frac{1}{\sqrt{3}}J_2^{1/2}\sin\theta\cos\phi\left(k\right)\frac{\partial\phi\left(k\right)}{\partial k}-\frac{\partial c\left(k\right)}{\partial k}\cos\phi\left(k\right)+c\left(k\right)\sin\phi\left(k\right)\frac{\partial\phi\left(k\right)}{\partial k} \qquad \text{(A.58)}$$

$$\frac{\partial f}{\partial\sigma_i}=\frac{1}{3}\frac{\partial I_1}{\partial\sigma_i}\sin\phi\left(k\right)+\frac{1}{2}J_2^{-1/2}\frac{\partial J_2}{\partial\sigma_i}\left[\cos\theta-\frac{1}{\sqrt{3}}\sin\theta\sin\phi\left(k\right)\right]-J_2^{1/2}\left[\sin\theta+\frac{1}{\sqrt{3}}\cos\theta\sin\phi\left(k\right)\right]\frac{\partial\theta}{\partial\sigma_i} \qquad \text{(A.59)}$$

$$\frac{\partial^2 f}{\partial\sigma_i\partial k}=\frac{1}{3}\frac{\partial I_1}{\partial\sigma_i}\cos\phi\left(k\right)\frac{\partial\phi\left(k\right)}{\partial k}-\frac{1}{2\sqrt{3}}J_2^{-1/2}\frac{\partial J_2}{\partial\sigma_i}\sin\theta\cos\phi\left(k\right)\frac{\partial\phi\left(k\right)}{\partial k}-\frac{1}{\sqrt{3}}J_2^{1/2}\cos\theta\frac{\partial\theta}{\partial\sigma_i}\cos\phi\left(k\right)\frac{\partial\phi\left(k\right)}{\partial k} \qquad \text{(A.60)}$$

$$\frac{\partial^2 f}{\partial k \partial \sigma_i} = \frac{1}{3}\frac{\partial I_1}{\partial \sigma_i}\cos\phi(k)\frac{\partial \phi(k)}{\partial k} - \frac{1}{2\sqrt{3}} J_2^{-1/2}\frac{\partial J_2}{\partial \sigma_i}\sin\theta\cos\phi(k)\frac{\partial \phi(k)}{\partial k} - \frac{1}{\sqrt{3}} J_2^{1/2}\cos\theta\frac{\partial \theta}{\partial \sigma_i}\cos\phi(k)\frac{\partial \phi(k)}{\partial k} = \frac{\partial^2 f}{\partial \sigma_i \partial k} \quad \text{(A.61)}$$

$$\frac{\partial^2 f}{\partial k^2} = -\frac{1}{3} I_1 \sin\phi(k)\frac{\partial \phi(k)}{\partial k}\frac{\partial \phi(k)}{\partial k} + \frac{1}{3} I_1 \cos\phi(k)\frac{\partial^2 \phi(k)}{\partial k^2} + \frac{1}{\sqrt{3}} J_2^{1/2}\sin\theta\sin\phi(k)\frac{\partial \phi(k)}{\partial k}\frac{\partial \phi(k)}{\partial k} - \frac{1}{\sqrt{3}} J_2^{1/2}\sin\theta\cos\phi(k)\frac{\partial^2 \phi(k)}{\partial k^2} - \frac{\partial^2 c(k)}{\partial k^2}\cos\phi(k) + \frac{\partial c(k)}{\partial k}\sin\phi(k)\frac{\partial \phi(k)}{\partial k} + \frac{\partial c(k)}{\partial k}\sin\phi(k)\frac{\partial \phi(k)}{\partial k} + c(k)\cos\phi(k)\frac{\partial \phi(k)}{\partial k}\frac{\partial \phi(k)}{\partial k} + c(k)\sin\phi(k)\frac{\partial^2 \phi(k)}{\partial k^2} \quad \text{(A.62)}$$

$$\begin{aligned}\frac{\partial^2 f}{\partial \sigma_j \partial \sigma_i} = {} & -\frac{1}{4} J_2^{-3/2}\frac{\partial J_2}{\partial \sigma_j}\frac{\partial J_2}{\partial \sigma_i}\left[\cos\theta - \frac{1}{\sqrt{3}}\sin\theta\sin\phi(k)\right] + \\ & \frac{1}{2} J_2^{-1/2}\frac{\partial}{\partial \sigma_j}\left(\frac{\partial J_2}{\partial \sigma_i}\right)\left[\cos\theta - \frac{1}{\sqrt{3}}\sin\theta\sin\phi(k)\right] - \\ & \frac{1}{2} J_2^{-1/2}\frac{\partial J_2}{\partial \sigma_i}\left[\sin\theta\frac{\partial \theta}{\partial \sigma_j} + \frac{1}{\sqrt{3}}\cos\theta\frac{\partial \theta}{\partial \sigma_j}\sin\phi(k)\right] - \\ & \frac{1}{2} J_2^{-1/2}\frac{\partial J_2}{\partial \sigma_j}\left[\sin\theta + \frac{1}{\sqrt{3}}\cos\theta\sin\phi(k)\right]\frac{\partial \theta}{\partial \sigma_i} - \\ & J_2^{1/2}\left[\cos\theta\frac{\partial \theta}{\partial \sigma_j} - \frac{1}{\sqrt{3}}\sin\theta\frac{\partial \theta}{\partial \sigma_j}\sin\phi(k)\right]\frac{\partial \theta}{\partial \sigma_i} - \\ & J_2^{1/2}\left[\sin\theta + \frac{1}{\sqrt{3}}\cos\theta\sin\phi(k)\right]\frac{\partial^2 \theta}{\partial \sigma_j \partial \sigma_i}\end{aligned} \quad \text{(A.63)}$$

Derivating Eq. (19) yields:

$$\frac{\partial \theta}{\partial \sigma_i} = -\frac{\sqrt{3}}{2}\frac{\frac{\partial J_3}{\partial \sigma_i} J_2^{3/2} - \frac{3}{2} J_3 \frac{\partial J_2}{\partial \sigma_i} J_2^{1/2}}{J_2^3\sqrt{1-(\sin 3\theta)^2}} \quad \text{(A.64)}$$

$$\frac{\partial^2\theta}{\partial\sigma_j\partial\sigma_i}=\frac{\partial}{\partial\sigma_j}\left(-\frac{\sqrt{3}}{2}\frac{\frac{\partial J_3}{\partial\sigma_i}J_2^{3/2}-\frac{3}{2}J_3\frac{\partial J_2}{\partial\sigma_i}J_2^{1/2}}{J_2^3\sqrt{1-\left(\sin 3\theta\right)^2}}\right)$$

$$=-\frac{\sqrt{3}}{2}\frac{\partial}{\partial\sigma_j}\left(\frac{g\left(\underline{\sigma}\right)}{h\left(\underline{\sigma}\right)}\right) \tag{A.65a}$$

$$=-\frac{\sqrt{3}}{2}\left(\frac{\frac{\partial g\left(\underline{\sigma}\right)}{\partial\sigma_j}h\left(\underline{\sigma}\right)-g\left(\underline{\sigma}\right)\frac{\partial h\left(\underline{\sigma}\right)}{\partial\sigma_j}}{\left(h\left(\underline{\sigma}\right)\right)^2}\right)$$

$$g\left(\underline{\sigma}\right)=\frac{\partial J_3}{\partial\sigma_i}J_2^{3/2}-\frac{3}{2}J_3\frac{\partial J_2}{\partial\sigma_i}J_2^{1/2} \tag{A.65b}$$

$$h\left(\underline{\sigma}\right)=J_2^3\sqrt{1-\left(\sin 3\theta\right)^2} \tag{A.65c}$$

$$\begin{aligned}\frac{\partial g}{\partial\sigma_j}=&\frac{\partial}{\partial\sigma_j}\left(\frac{\partial J_3}{\partial\sigma_i}\right)J_2^{3/2}+\frac{3}{2}\frac{\partial J_3}{\partial\sigma_i}\frac{\partial J_3}{\partial\sigma_j}J_2^{1/2}-\frac{3}{2}\frac{\partial J_3}{\partial\sigma_j}\frac{\partial J_2}{\partial\sigma_i}J_2^{1/2}\\&-\frac{3}{2}J_3\frac{\partial}{\partial\sigma_j}\left(\frac{\partial J_2}{\partial\sigma_i}\right)J_2^{1/2}-\frac{3}{4}J_3\frac{\partial J_2}{\partial\sigma_i}\frac{\partial J_2}{\partial\sigma_j}J_2^{-1/2}\end{aligned} \tag{A.65d}$$

$$\frac{\partial h}{\partial\sigma_j}=3\frac{\partial J_2}{\partial\sigma_j}J_2^2\sqrt{1-\left(\sin 3\theta\right)^2}-3J_2^3\sin 3\theta\cos 3\theta\frac{\partial\theta}{\partial\sigma_j}\left[1-\left(\sin 3\theta\right)^2\right]^{-1/2} \tag{A.65e}$$

For the singularity point of θ=30° ($\cos 30^\circ=\sqrt{3}/2$; $\sin 30^\circ=1/2$; $\partial\theta/\partial\sigma_i=0$; $\partial^2\theta/\left(\partial\sigma_j\partial\sigma_i\right)=0$)

$$f\left(\underline{\sigma},k\right)=\frac{1}{3}I_1\sin\phi\left(k\right)+J_2^{1/2}\left(\frac{\sqrt{3}}{2}-\frac{1}{2\sqrt{3}}\sin\phi\left(k\right)\right)-c\left(k\right)\cos\phi\left(k\right) \tag{A.66}$$

$$\begin{aligned}\frac{\partial f}{\partial k}=&\frac{1}{3}I_1\cos\phi\left(k\right)\frac{\partial\phi\left(k\right)}{\partial k}-\frac{1}{2\sqrt{3}}J_2^{1/2}\cos\phi\left(k\right)\frac{\partial\phi\left(k\right)}{\partial k}-\frac{\partial c\left(k\right)}{\partial k}\cos\phi\left(k\right)+\\&c\left(k\right)\sin\phi\left(k\right)\frac{\partial\phi\left(k\right)}{\partial k}\end{aligned} \tag{A.67}$$

$$\frac{\partial f}{\partial\sigma_i}=\frac{1}{3}\frac{\partial I_1}{\partial\sigma_i}\sin\phi\left(k\right)+\frac{1}{2}J_2^{-1/2}\frac{\partial J_2}{\partial\sigma_i}\left[\frac{\sqrt{3}}{2}-\frac{1}{2\sqrt{3}}\sin\phi\left(k\right)\right] \tag{A.68}$$

$$\frac{\partial^2 f}{\partial\sigma_i\partial k}=\frac{1}{3}\frac{\partial I_1}{\partial\sigma_i}\cos\phi\left(k\right)\frac{\partial\phi\left(k\right)}{\partial k}-\frac{1}{4\sqrt{3}}J_2^{-1/2}\frac{\partial J_2}{\partial\sigma_i}\cos\phi\left(k\right)\frac{\partial\phi\left(k\right)}{\partial k} \tag{A.69}$$

$$\frac{\partial^2 f}{\partial k \partial \sigma_i} = \frac{1}{3}\frac{\partial I_1}{\partial \sigma_i}\cos\phi(k)\frac{\partial \phi(k)}{\partial k} - \frac{1}{4\sqrt{3}}\, J_2^{-1/2}\frac{\partial J_2}{\partial \sigma_i}\cos\phi(k)\frac{\partial \phi(k)}{\partial k} = \frac{\partial^2 f}{\partial \sigma_i \partial k} \tag{A.70}$$

$$\frac{\partial^2 f}{\partial k^2} = -\frac{1}{3}I_1\sin\phi(k)\frac{\partial \phi(k)}{\partial k}\frac{\partial \phi(k)}{\partial k} + \frac{1}{3}I_1\cos\phi(k)\frac{\partial^2 \phi(k)}{\partial k^2} + \frac{1}{2\sqrt{3}}\, J_2^{1/2}\sin\phi(k)\frac{\partial \phi(k)}{\partial k}\frac{\partial \phi(k)}{\partial k} - \frac{1}{2\sqrt{3}}\, J_2^{1/2}\cos\phi(k)\frac{\partial^2 \phi(k)}{\partial k^2} - \frac{\partial^2 c(k)}{\partial k^2}\cos\phi(k) + \frac{\partial c(k)}{\partial k}\sin\phi(k)\frac{\partial \phi(k)}{\partial k} + \frac{\partial c(k)}{\partial k}\sin\phi(k)\frac{\partial \phi(k)}{\partial k} + c(k)\cos\phi(k)\frac{\partial \phi(k)}{\partial k}\frac{\partial \phi(k)}{\partial k} + c(k)\sin\phi(k)\frac{\partial^2 \phi(k)}{\partial k^2} \tag{A.71}$$

$$\frac{\partial^2 f}{\partial \sigma_j \partial \sigma_i} = -\frac{1}{4}J_2^{-3/2}\frac{\partial J_2}{\partial \sigma_j}\frac{\partial J_2}{\partial \sigma_i}\left[\frac{\sqrt{3}}{2} - \frac{1}{2\sqrt{3}}\sin\phi(k)\right] + \frac{1}{2}J_2^{-1/2}\frac{\partial}{\partial \sigma_j}\left(\frac{\partial J_2}{\partial \sigma_i}\right)\left[\frac{\sqrt{3}}{2} - \frac{1}{2\sqrt{3}}\sin\phi(k)\right] \tag{A.72}$$

For the singularity point of θ=-30° ($\cos(-30^\circ) = \sqrt{3}/2$; $\sin(-30^\circ) = -1/2$; $\partial\theta/\partial\sigma_i = 0$; $\partial^2\theta/(\partial\sigma_j\partial\sigma_i) = 0$)

$$f(\underline{\sigma}, k) = \frac{1}{3}I_1\sin\phi(k) + J_2^{1/2}\left(\frac{\sqrt{3}}{2} + \frac{1}{2\sqrt{3}}\sin\phi(k)\right) - c(k)\cos\phi(k) \tag{A.73}$$

$$\frac{\partial f}{\partial k} = \frac{1}{3}I_1\cos\phi(k)\frac{\partial \phi(k)}{\partial k} + \frac{1}{2\sqrt{3}}\, J_2^{1/2}\cos\phi(k)\frac{\partial \phi(k)}{\partial k} - \frac{\partial c(k)}{\partial k}\cos\phi(k) + c(k)\sin\phi(k)\frac{\partial \phi(k)}{\partial k} \tag{A.74}$$

$$\frac{\partial f}{\partial \sigma_i} = \frac{1}{3}\frac{\partial I_1}{\partial \sigma_i}\sin\phi(k) + \frac{1}{2}J_2^{-1/2}\frac{\partial J_2}{\partial \sigma_i}\left[\frac{\sqrt{3}}{2} + \frac{1}{2\sqrt{3}}\sin\phi(k)\right] \tag{A.75}$$

$$\frac{\partial^2 f}{\partial \sigma_i \partial k} = \frac{1}{3}\frac{\partial I_1}{\partial \sigma_i}\cos\phi(k)\frac{\partial \phi(k)}{\partial k} + \frac{1}{4\sqrt{3}}\, J_2^{-1/2}\frac{\partial J_2}{\partial \sigma_i}\cos\phi(k)\frac{\partial \phi(k)}{\partial k} \tag{A.76}$$

$$\frac{\partial^2 f}{\partial k \partial \sigma_i} = \frac{1}{3}\frac{\partial I_1}{\partial \sigma_i}\cos\phi(k)\frac{\partial \phi(k)}{\partial k} + \frac{1}{4\sqrt{3}}\, J_2^{-1/2}\frac{\partial J_2}{\partial \sigma_i}\cos\phi(k)\frac{\partial \phi(k)}{\partial k} = \frac{\partial^2 f}{\partial \sigma_i \partial k} \tag{A.77}$$

$$\frac{\partial^2 f}{\partial k^2} = -\frac{1}{3} I_1 \sin\phi(k) \frac{\partial \phi(k)}{\partial k} \frac{\partial \phi(k)}{\partial k} + \frac{1}{3} I_1 \cos\phi(k) \frac{\partial^2 \phi(k)}{\partial k^2} - \frac{1}{2\sqrt{3}} J_2^{1/2} \sin\phi(k) \frac{\partial \phi(k)}{\partial k} \frac{\partial \phi(k)}{\partial k} + \frac{1}{2\sqrt{3}} J_2^{1/2} \cos\phi(k) \frac{\partial^2 \phi(k)}{\partial k^2} - \frac{\partial^2 c(k)}{\partial k^2} \cos\phi(k) + \frac{\partial c(k)}{\partial k} \sin\phi(k) \frac{\partial \phi(k)}{\partial k} + \frac{\partial c(k)}{\partial k} \sin\phi(k) \frac{\partial \phi(k)}{\partial k} + c(k) \cos\phi(k) \frac{\partial \phi(k)}{\partial k} \frac{\partial \phi(k)}{\partial k} + c(k) \sin\phi(k) \frac{\partial^2 \phi(k)}{\partial k^2} \tag{A.78}$$

$$\frac{\partial^2 f}{\partial \sigma_j \partial \sigma_i} = -\frac{1}{4} J_2^{-3/2} \frac{\partial J_2}{\partial \sigma_j} \frac{\partial J_2}{\partial \sigma_i} \left[\frac{\sqrt{3}}{2} + \frac{1}{2\sqrt{3}} \sin\phi(k) \right] + \frac{1}{2} J_2^{-1/2} \frac{\partial}{\partial \sigma_j} \left(\frac{\partial J_2}{\partial \sigma_i} \right) \left[\frac{\sqrt{3}}{2} + \frac{1}{2\sqrt{3}} \sin\phi(k) \right] \tag{A.79}$$

A.5 The first and the second order derivatives of the yield function of the Drucker-Prager criterion

The formulation is developed in the assumption a hardening/softening parameter, *k*, can be used to simulate the evolution of the cohesion and frictional angle of the material with the plastic variation, i.e., *c(k)* and *ϕ(k)*.

$$f(\underline{\sigma}, k) = \alpha(k) I_1 + J_2^{1/2} - \beta(k) \tag{A.80}$$

being $\alpha(k)$ and $\beta(k)$ defined in Eqs. (31) and (32), respectively. In this section the derivatives necessary for the implementation of the model are presented.

$$\frac{\partial f}{\partial k} = \frac{\partial \alpha(k)}{\partial k} I_1 - \frac{\partial \beta(k)}{\partial k} \tag{A.81}$$

If it was assumed:

$$g(k) = \sin\phi(k) \tag{A.82}$$

$$h(k) = 3 + a \sin\phi(k) \tag{A.83}$$

$$s(k) = c(k) \cos\phi(k) \tag{A.84}$$

where *a*=1 for inner corners and *a*=-1 for outer corners. Since:

$$\frac{\partial g(k)}{\partial k} = \cos\phi(k) \frac{\partial \phi(k)}{\partial k} \tag{A.85}$$

$$\frac{\partial h(k)}{\partial k} = a \cos\phi(k) \frac{\partial \phi(k)}{\partial k} \tag{A.86}$$

$$\frac{\partial s(k)}{\partial k} = \frac{\partial c(k)}{\partial k} \cos\phi(k) - c(k) \sin\phi(k) \frac{\partial \phi(k)}{\partial k} \tag{A.87}$$

then

$$\frac{\partial \alpha(k)}{\partial k} = \frac{2}{\sqrt{3}} \frac{\partial}{\partial k}\left(\frac{g(k)}{h(k)}\right) = \frac{2}{\sqrt{3}} \frac{\cos\phi(k)\frac{\partial \phi(k)}{\partial k} h(k) - g(k) a \cos\phi(k) \frac{\partial \phi(k)}{\partial k}}{h^2(k)} \tag{A.88}$$

and

$$\frac{\partial \beta(k)}{\partial k} = \frac{6}{\sqrt{3}} \frac{\partial}{\partial k}\left(\frac{s(k)}{h(k)}\right) = \frac{6}{\sqrt{3}} \frac{\frac{\partial s(k)}{\partial k} h(k) - s(k) \frac{\partial h(k)}{\partial k}}{h^2(k)} = \frac{6}{\sqrt{3}} \frac{\left(\frac{\partial c(k)}{\partial k}\cos\phi(k) - c(k)\sin\phi(k)\frac{\partial \phi(k)}{\partial k}\right) h(k) - s(k) a \cos\phi(k) \frac{\partial \phi(k)}{\partial k}}{h^2(k)} \tag{A.89}$$

$$\frac{\partial f}{\partial \sigma_i} = \alpha(k) \frac{\partial I_1}{\partial \sigma_i} + \frac{1}{2} \frac{\partial J_2}{\partial \sigma_i} J_2^{-1/2} \tag{A.90}$$

$$\frac{\partial^2 f}{\partial k \partial \sigma_i} = \frac{\partial \alpha(k)}{\partial k} \frac{\partial I_1}{\partial \sigma_i} \tag{A.91}$$

$$\frac{\partial^2 f}{\partial \sigma_j \partial \sigma_i} = \frac{1}{2} \frac{\partial}{\partial \sigma_j}\left(\frac{\partial J_2}{\partial \sigma_i}\right) J_2^{-1/2} - \frac{1}{4} \frac{\partial J_2}{\partial \sigma_i} \frac{\partial J_2}{\partial \sigma_j} J_2^{-3/2} \tag{A.92}$$

$$\frac{\partial^2 f}{\partial k^2} = \frac{\partial^2 \alpha(k)}{\partial k^2} I_1 - \frac{\partial^2 \beta(k)}{\partial k^2} \tag{A.93}$$

Assuming:

$$t(k) = \frac{\partial g(k)}{\partial k} h(k) - g(k) \frac{\partial h(k)}{\partial k} \tag{A.94}$$

$$u(k) = h^2(k) \tag{A.95}$$

$$\mathrm{v}(k) = \frac{\partial s(k)}{\partial k} h(k) - s(k) \frac{\partial h(k)}{\partial k} \tag{A.96}$$

Then

$$\frac{\partial \alpha(k)}{\partial k} = \frac{2}{\sqrt{3}} \frac{t(k)}{u(k)} \tag{A.97}$$

$$\frac{\partial \beta(k)}{\partial k} = \frac{6}{\sqrt{3}} \frac{\mathrm{v}(k)}{u(k)} \tag{A.98}$$

and therefore,

$$\frac{\partial^2 \alpha(k)}{\partial k^2} = \frac{2}{\sqrt{3}} \frac{\frac{\partial t(k)}{\partial k} u(k) - t(k) \frac{\partial u(k)}{\partial k}}{u^2(k)} \tag{A.99}$$

where

$$\frac{\partial t(k)}{\partial k} = \frac{\partial^2 g(k)}{\partial k^2} h(k) - g(k) \frac{\partial^2 h(k)}{\partial k^2} \tag{A.100}$$

being

$$\frac{\partial^2 g(k)}{\partial k^2} = \frac{\partial^2 \phi(k)}{\partial k^2} \cos\phi(k) - \sin\phi(k) \frac{\partial \phi(k)}{\partial k} \frac{\partial \phi(k)}{\partial k} \tag{A.101}$$

$$\frac{\partial u(k)}{\partial k} = 2h(k) \frac{\partial h(k)}{\partial k} \tag{A.102}$$

$$\frac{\partial^2 h(k)}{\partial k^2} = a \left(\frac{\partial^2 \phi(k)}{\partial k^2} \cos\phi(k) - \sin\phi(k) \frac{\partial \phi(k)}{\partial k} \frac{\partial \phi(k)}{\partial k} \right) \tag{A.103}$$

$$\frac{\partial^2 \beta(k)}{\partial k^2} = \frac{6}{\sqrt{3}} \left(\frac{\frac{\partial \mathrm{v}(k)}{\partial k} u(k) - \mathrm{v}(k) \frac{\partial u(k)}{\partial k}}{u^2(k)} \right) \tag{A.104}$$

where

$$\frac{\partial \mathrm{v}(k)}{\partial k} = \frac{\partial^2 s(k)}{\partial k^2} h(k) - s(k) \frac{\partial^2 h(k)}{\partial k^2} \tag{A.105}$$

$$\begin{aligned} \frac{\partial^2 s(k)}{\partial k^2} = \frac{\partial^2 c(k)}{\partial k^2} \cos\phi(k) - 2 \frac{\partial c(k)}{\partial k} \frac{\partial \phi(k)}{\partial k} \sin\phi(k) - \\ c(k) \cos\phi(k) \frac{\partial \phi(k)}{\partial k} \frac{\partial \phi(k)}{\partial k} - c(k) \sin\phi(k) \frac{\partial^2 \phi(k)}{\partial k^2} \end{aligned} \tag{A.106}$$

A.6 The first and the second order derivatives of the softening/hardening evolution laws

First derivative of the cohesion evolution law:

$$\frac{dc(k)}{dk} = -\frac{p}{k_c} \frac{k}{k_c}^{(p-1)} c(k) \tag{A.107}$$

Second derivative of the cohesion evolution law:

$$\frac{d^2 c(k)}{dk^2} = -\frac{p}{k_c} \frac{k}{k_c}^{(p-1)} \left[(p-1) \frac{1}{k_c} \frac{k}{k_c}^{(-1)} - \frac{p}{k_c} \frac{k}{k_c}^{(p-1)} \right] c(k) \tag{A.108}$$

First derivative of the frictional angle evolution law:

$$\frac{d\phi(k)}{dk} = \frac{q}{k_f} (\phi_f - \phi_o) \left(\frac{k}{k_f} \right)^{(q-1)} e^{-\left(\frac{k}{k_f}\right)^q} \tag{A.109}$$

Second derivative of the frictional angle evolution law:

$$\frac{d^2\phi(k)}{dk^2} = \frac{q}{k_f}\left(\phi_f - \phi_o\right)e^{-\left(\frac{k}{k_f}\right)^q}\left[\frac{q-1}{k_f}\left(\frac{k}{k_f}\right)^{(q-2)} - \left(\frac{k}{k_f}\right)^{(q-1)}\frac{q}{k_f}\right] \tag{A.110}$$